Studies on Fabrication and Characterization of High Efficiency Optical Sensing Devices

Hiroshi Imamoto

2011

Contents

General Introduction

1. Objective of this study

The background of this study is first introduced; the issues in semiconductor optical devices for optical sensing, such as photo interrupter, photoelectric sensor, ultraviolet (UV) sensor, infrared human sensor and optical sensor, are discussed.

There are so many kinds of optical sensors, for example on/off optical switch by using light irradiation and detection, measurement of a distance to objects by measuring the flight time of light, UV sensing by optical absorption, and so on. Additionally, some environmental gas sensor, detecting CO_2, NO_x, SO_x, etc. by wavelength spectrum of optical absorption has been put into practical use. The optical sensing devices are classified into light emitting devices such as light emitting diodes (LEDs) and laser diodes (LDs) and photodetectors such as photodiodes, phototransistors, UV detectors and solar cells. The background history of this thesis is summarized in Table 1 and they cover both the light emitting devices and detectors at various wavelengths.

(1) Light Emitting Devices

The feature of LD is its high light output power from a small emitting area because of stimulated emission. Therefore, LD is more suitable for long distance and small target sensing in comparison with LED. On the other hand, LED is easy to use due to its high reliability and eye safety characteristics based on low optical power density with spontaneous emission. The history of light emitting devices is described as follows. The first lasing operation of GaAs and GaAsP semiconductor lasers was achieved in 1962 [1-4]. In 1970, double hetero-structure (DH) laser was developed and continuous wave (CW) operation was achieved by confining electrons and holes in the active region

[5-7]. After those successful results, this DH structure has been widely used for the purpose of carrier confinement in light-emitting semiconductor devices such as LDs and LEDs [8]. Up to now, many kinds of materials for semiconductor lasers have been investigated, for example, AlGaAs/GaAs infrared lasers for optical sensing and optical memory systems, AlGaInP/GaInP, GaInAsP/GaAs, GaInAsP/GaAsP and GaInAsP/AlGaAs for visible light sources and optical sensing systems. Recently, InGaN materials have been widely used for illuminations, color sensors and so on. But this material is not suitable for optical sensing because of its low detection sensitivity and high production cost. Among these materials, AlGaAs/GaAs is well investigated and widely applied to various systems as a key device of ubiquitous sensor systems and their business has formed a big market and keeps on growing up.

(2) Photodetectors

Photodetectors are sensors of light or other electromagnetic energy. There are several varieties as follows: (i) Photovoltaic cells or solar cells, which generate a voltage and supply an electric current when illuminated. (ii) Photodiodes, which can operate in photovoltaic mode or photoconductive mode. Especially, in terms of sensitivity, avalanche photodiode (APD) is the best candidate. (iii) Photomultiplier tubes, which are extremely sensitive detectors of light in the ultraviolet, visible and near infrared ranges of the electromagnetic spectrum. (iv) Infrared detectors, which are responding purely to the heating effect of the incoming radiation, such as pyroelectric detectors, Golay cells, thermocouples and thermistors, but the latter two are much less sensitive. Cryogenic detectors are sufficiently sensitive to measure the energy of single x-ray, visible or near infra-red photons. (v) Charge coupled devices (CCD) and MOS image sensors, which are used to record images in the fields of astronomy, digital photography, and digital cinematography.

Table 1 The background history of this thesis

	Light Emitting Device	Detector
1954		Practical solar cells 6%(D.M.Chapin) [17]
1962	First Lasing (GE,MIT,IBM) [1-4]	
1965		High Speed APD (K.M.Jonson) [18]
1970	RT CW, DH [5-8]	GaAs hetero-structure solar cell [19]
1978		AlGaAs DH-PD (R.C.Millar) [20]
1979	1.5 μm InGaAsP LD [9]	GaInAs PD (K.Ahmad) [21]
1981		SAM APD [22]
1982		Superlattice APD (F.Cappaso) [23]
1983	AlGaInP-LD RT pulse [10]	
1985	AlGaInP-LD RT [11]	
1990	630 nm laser RT CW [12]	
1991	InGaN- LD (pulse) [13]	
1997	InGaN RT-CW LD [14]	
2001		InGaN Schottky UV-sensor [24]
2004	Quantum cascade laser RT CW [15]	
2006		InGaN Schottky vacuum UV-sensor [25]
2008	GaN photonic crystal LD [16]	

It is important to choose the best device for each application. In this dissertation, the author introduces the mainstream topics. The APD （Avalanche Photodiode） based on a structure of SAM (Separated Absorption and Multiplication Regions) was proposed in 1981. This structure is composed of optical amplification regions and optical absorption layer, which shows the basic function of APD over wide wavelength range. In addition, Capasso and co-workers suggested a superlattice APD using the superlattice sub-bands and then achieved the basic structure of low-noise APD [23]. Furthermore, they succeeded in fast response of 40 Gbit/sec by the use of a pin-PD coupled with the waveguide. Next, the descriptions of solar cell follow. Initial solar cell researches dates even back to 1800's. Chapin and co-workers invented the first solar cells with the reported quantum efficiency of 6 % in 1954 [17]. And in 1970, the first highly effective GaAs heterostructure solar cells were created by Alfelov and co-workers [19]. Metal organic chemical vapor deposition (MOCVD) production equipment wasn't developed until the early 1980s, limiting the ability of companies to manufacture the GaAs solar cell. In the United States, the first 17 % efficient air mass zero single-junction GaAs solar cells were manufactured in production quantities in 1988 by Applied Solar Energy Corporation. Since then, many groups have been trying to develop higher quantum efficiency with CIGS (Copper Indium Gallium Di-Selenide) type, amorphous silicon type and dye-sensitized solar cells, etc, and additionally to provide them at much lower cost.

The most important issue of optical sensing is eliminating false detections under any circumstances. Regarding optical sensing, it is important to detect a small size, long distance object and a slight amount of constituent without fail. That is to say, high sensitivity and high signal to noise ratio (S/N) are eternal market needs. In addition, from a practical point of view, accessible tool to adjust optical axis, low cost, and high reliability are very important.

There are some causes of false detection as follows: (i) Changing of the spectrum pattern by object color and reflectivity. (ii) Optical disturbance from

outside and adjacent sensor light. (iii) Changing detection sensitivity by temperature dependence of emission and detection wavelength. (iv) Changing detection sensitivity by temperature dependence of light output characteristics and detector sensitivity. (v) Reincident light of reflection from detection surface.

The PIN photo diode is a diode with a wide, lightly doped near intrinsic semiconductor region between a p-type and an n-type semiconductor regions. Due to the intrinsic layer, a PIN photodiode must be reverse biased (Vr), and as the Vr increases the depletion region allows a larger region for electron-hole production. Avalanche photodiodes have a similar structure to regular PIN photodiodes, but they are operated with much higher reverse bias. This allows each photo generated carrier to be multiplied by avalanche breakdown, resulting in high gain within the photodiode, which increases the effective sensitivity of the device. Thus, by applying a high reverse voltage (typically 100-200 V), APDs show an internal current gain effect due to impact ionization. Since APD gain varies strongly with the applied reverse bias and temperature, it is necessary to control the reverse voltage and/or temperature in order to keep a stable gain. In general, for the measurement of UV rays, Si photo-detector components are used. However, light sensitivity often deteriorates due to radiation damage, particularly in the far-UV region of high photon energy at 200 nm or shorter wavelength.

The background of this study is summarized as follows: (i) As the semiconductor light source for photoelectric sensor and photo interrupter, high efficiency and temperature stable characteristics are very important. On the other hand, from the view point of eye safety, visible spontaneous emission light source is suitable in comparison with stimulated emission. (ii) Since APD gain varies strongly with the applied reverse bias and temperature, it is necessary to control the reverse voltage and temperature in order to keep a stable gain. Avalanche photodiodes become expensive by accompanying their control circuit. Therefore, a low cost, high efficiency and good temperature stabilized detectors are required. Also in the ultraviolet region, wide bandgap and more resistant

materials are suitable for high efficiency and high reliability.

In accordance with the background described previously, requirements for the optical sensing devices are summarized as follows: (i) To improve efficiency of light source and sensitivity of detector in order to obtain high S/N ratio and low current consumption. (ii) Pin-point light sources in order to detect smaller objects securely. (iii) High temperature stability of light output and wavelength. (iv) Visible light source in order to adjust the optical axis. (v) Detector with high temperature stability and low reflection surface.

This section discusses the issues of this study. There are three main objectives based on the above background.

(a) Optimal light emitting device structures as a light source for optical sensing.

- Improving the crystalline of the PN junction in order to obtain highly efficient and reliable laser diode.
- Optimization of quantum well active layer structures in order to obtain highly effective, highly temperature stable and visible laser diode.
- A proposal of new unique light source and its practical application for optical sensing.

(b) Formation of nano-structure for high sensitivity UV sensor.

- Fabrication of nano-structures by MOCVD method.
- A proposal of fabrication method for nano-structures by aqueous solution process.
- Evaluation of sensor sensitivity.
- Development of new sensor by using nano-structure.

(c) Proposal of high sensitivity infrared sensing devices by using femtosecond laser irradiation.

- Fabrication of anti-reflection structure by using femtosecond laser and their applications for high sensitivity infrared sensors.

2. Fabrication Methods of Optical Sensing Devices

The formation of nano-size structure by using quantum effects is important to semiconductor optical sensing devices because the nano-size structure improves device characteristics drastically. A crystal growth technology is important as a bottom-up technique, on the other hand, the formation of the top-down processing such as femtosecond laser processing is also important. In this session, the semiconductor crystal growth and femtosecond processing are described.

(1) Semiconductor Crystal Growth Technology

There are important techniques used to improve optical sensing characteristics. The epitaxial growth techniques which have profound effect on emission efficiency and reliability for light emitting device are presented. Most of the advances in semiconductor processing have centered on the ability to decrease the physical dimensions of the device structure. The control of vertical dimension can be easily realized by epitaxial deposition. Table 2 shows comparison of epitaxial methods which are now commonly used as semiconductor crystal growth technologies.

Table 2 Typical epitaxial growth methods

Growth Method	Time	Feature	Problem
LPE (Liquid Phase Epitaxy)	1958	Growth from supersaturated solution on substrates	Poor control over the growth of very thin layer
MBE (Molecular Beam Epitaxy)	1963	Epitaxial growth at ultra-high vacuum	Difficulty of epitaxial growth with high vacuum
MOCVD (Metal Organic Chemical Vapor Deposition)	1968	Use of metal organic sources for growth	Use of toxic gases

Since the pioneering work of superlattice by L. Esaki, various kinds of quantum enhanced devices were proposed. In order to realize these devices including the quantum well lasers, the sophisticated crystal growth techniques such as molecular beam epitaxy (MBE), and metalorganic chemical vapor deposition (MOCVD), both can precisely control the layer thickness, have been developed and some of these are now widely used in the production line. Recently the layer thickness can be much more precisely controlled within ±1 monolayer using the fine crystal growth techniques such as migration enhanced epitaxy (MEE) [26, 27], phase locked epitaxy [28], and atomic layer epitaxy [29]. In this session, the basic mechanism and some advantages of our crystal growth techniques are described.

Molecular beam epitaxy is the most suitable method to control the monolayer thickness of III-V compound semiconductors. A schematic diagram of the MBE system used in this thesis is shown in Fig. 1. The MBE system suitable for the growth of III-V compound films is based on three chambers, which are growth chamber, analysis chamber and load lock chamber, and the UHV system. All these chambers, except for load lock chamber, have UHV type pumping systems (ion-, cryo-, and titanium sublimation pumps). They also incorporate large area of liquid nitrogen cooled panels. The UHV is essential in order to avoid contamination of the surface and the growing epitaxial film. The base total pressure routinely achieved in MBE system is in the low 10^{-10} to 10^{-11} Torr range. The system includes a quadruple mass spectrometer for gas analysis and reflection high energy electron diffraction (RHEED) system for assessment of surface structure and growth dynamics. RHEED is a powerful method of in-situ monitoring for the monolayer growth. It provides a very sensitive, simple, diagnostic tool for observing changes in the structure of each surface layer as a function of growth parameters. It is possible to obtain information on surface structure and smoothness from RHEED patterns. The period of the oscillations from the specular beam of the RHEED corresponds exactly to the monolayer thickness on (100) oriented substrate. Figure 2 shows

the intensity associated with the specula beam for (100) GaAs growth. Typically the growth rate is one monolayer per second (approximately 1 μm per hour). By this phenomenon, precisely controlled AlGaAs/GaAs hetero-structures, including quantum well structure, is formed. The phase locked epitaxy method [28] based on above phenomenon is suitable for in-situ monolayer control by Al and Ga flux.

Metalorganic chemical vapor deposition (MOCVD) is a chemical vapor deposition method of epitaxial growth, especially for compound semiconductors from the surface reaction of metalorganic compounds. Formation of the epitaxial layer occurs after final pyrolysis of their compounds at the substrate surface. Metal organic chemical vapor deposition has some other names, but all of them refer to essentially the same growth method [OMCVD (Organo-Metallic Chemical Vapor Deposition), MOVPE (Metal Organic Vapor Phase Epitaxy), and OMVPE (Organo-Metallic Vapor Phase Epitaxy)]. Gas handling in MOCVD is very important to grow high quality epitaxial layers. The role of gas handling includes mixing and metering of the gases to be introduced onto the substrate. Timing and composition of the gases take effects on determined structures and qualities of epi-layers. For low-pressure growth, mechanical pump and pressure controller are used to control the growth pressure. The pump in the exhaust system should be designed to handle large gas load. The treatment of exhaust gas is a matter of safety. The MOCVD system for GaAs, InAs, and InP use toxic sources like AsH_3 and PH_3. The exhaust gases still contain undecomposed AsH_3 and PH_3, and normally, the toxic gas need to be removed by using a chemical scrubber. The partial pressure of the metal-organic (MO) source is important in MOCVD since it determines the concentration of deposition layer and the deposition rate on a substrate. The partial pressures of MO compounds are calculated according to the expression written below:

$$Log\ [P\,(torr\ )] = B - A / T \qquad \cdots\cdots\cdots\cdots (1)$$

P: partial pressure (torr)
T: Temperature (K)
A, B: Antoine constant

In addition, to calculate the molar flow rate (F) of MO source at 273 K:

$$F(mol/\min.) = P_{MO} / P_{bub} \times [\,flowrate(mol/\min.)]/ 22400 \qquad \cdots\cdots (2)$$

F: Molar flow rate of MO source (mol/min.)
P: Partial pressure (torr)

If alloy growth is required, the molar flow rate is an important guideline to estimate the composition of the alloys. When growing the AlGaAs for example, the Al concentration can be estimated using the following formula if the thermal-cracking and sticking efficiency of Al and Ga sources are the same:

$$^{\xi}X_{Al} = F_{Al} / [F_{Al} + F_{Ga}] \qquad \cdots\cdots\cdots\cdots (3)$$

$^{\zeta}X_{Al}$: Al Composition of AlGaAs alloy
F: Molar flow rate of MO source

In MOCVD, the growth proceeds as follows: (i) MO and other sources for growth are introduced onto the substrate. (ii) On the substrate, the temperature initiates the decomposition of source, forming the film precursors. (iii) The precursors are transported to the substrate. (iv) The precursors are absorbed on the substrate. (v) The precursors diffuse to the growth site. (vi) At the surface, ad-atoms incorporate into the growing film through surface reaction. (vii) The by-products of the surface reactions appear on the surface. (viii) The by-products are transported to the main gas flow region away from the deposition area toward the reactor exit.

In contrast to MBE, the growth of crystals is by chemical reaction and not

physical deposition. This takes place not in a vacuum, but from the gas phase at moderate pressures (2 to 100 kPa). This technique is preferred for the formation of devices incorporating thermodynamically metastable alloys. It has become the dominant process for manufacturing laser diodes, solar cells, and LEDs. On the other hand, the MBE have in-situ monitoring capability by using RHEED. Therefore the MBE is suitable for clarifying the growth mechanism.

⑵ Microstructure Fabrication Technology by Femtosecond Laser

Femtosecond (fs) laser processing is a powerful tool for developing new devices for future sensing and information technology and so on. Due to the very high power density, the interaction of femtosecond laser beams with materials is mainly based on nonlinear optical processes such as multiphoton ionization. The multiphoton absorption process is characterized by a certain laser power density threshold. For a focused beam with a Gaussian intensity profile, the heat affected volume becomes smaller than the focus size when the laser fluence is at or just above the threshold value. Once the plasma of free electrons is generated by multiphoton absorption and ionisation reaches a high enough density, irreversible material breakdown and ablation begin. The electrons transfer energy to the ions and the lattice, and the material is heated up to much higher temperatures compared to the long pulses cases. Due to the very short pulse duration, the heat diffusion to the surrounding volume of the material is negligible. A large fraction of the material in the small interaction volume is directly vaporized, going through the melt phase very quickly. For femtosecond pulses, the resulting melt layer thickness will be very small because most of the heated material reaches the vaporization temperature, and there is rapid cooling due to the steep temperature gradient. Practically, a large amount of the absorbed laser energy is carried away by the direct vaporization. As a result, ablation and material removal become very precise, in contrast to

the long pulse case, and the ablated area is significantly smaller than the focused beam size.

Our femtosecond laser apparatus is shown in Fig. 3. The irradiation sources employed was a re-generatively amplified 800 nm Ti-sapphire laser that emitted 1 kHz, modelocked pulses. The average of the laser beam power at the sample location was controlled approximately between 40 and 700 mW by neutral-density filters that were inserted between the laser and the microscope objective lens. With the help of an XYZ stage, the samples were transported at the rate of 100-10,000 mm/sec. either in parallel or perpendicular to the incident laser beam.

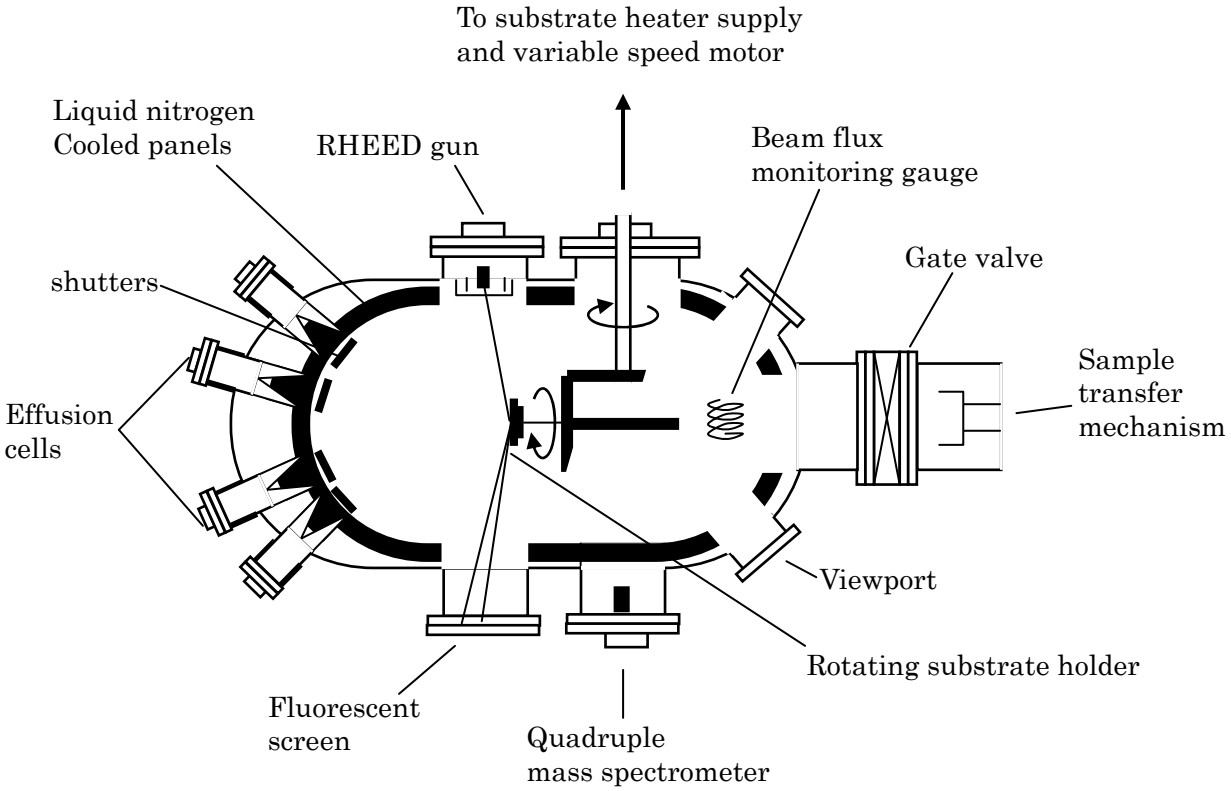

Fig. 1 Schematic diagram of molecular beam epitaxy system.

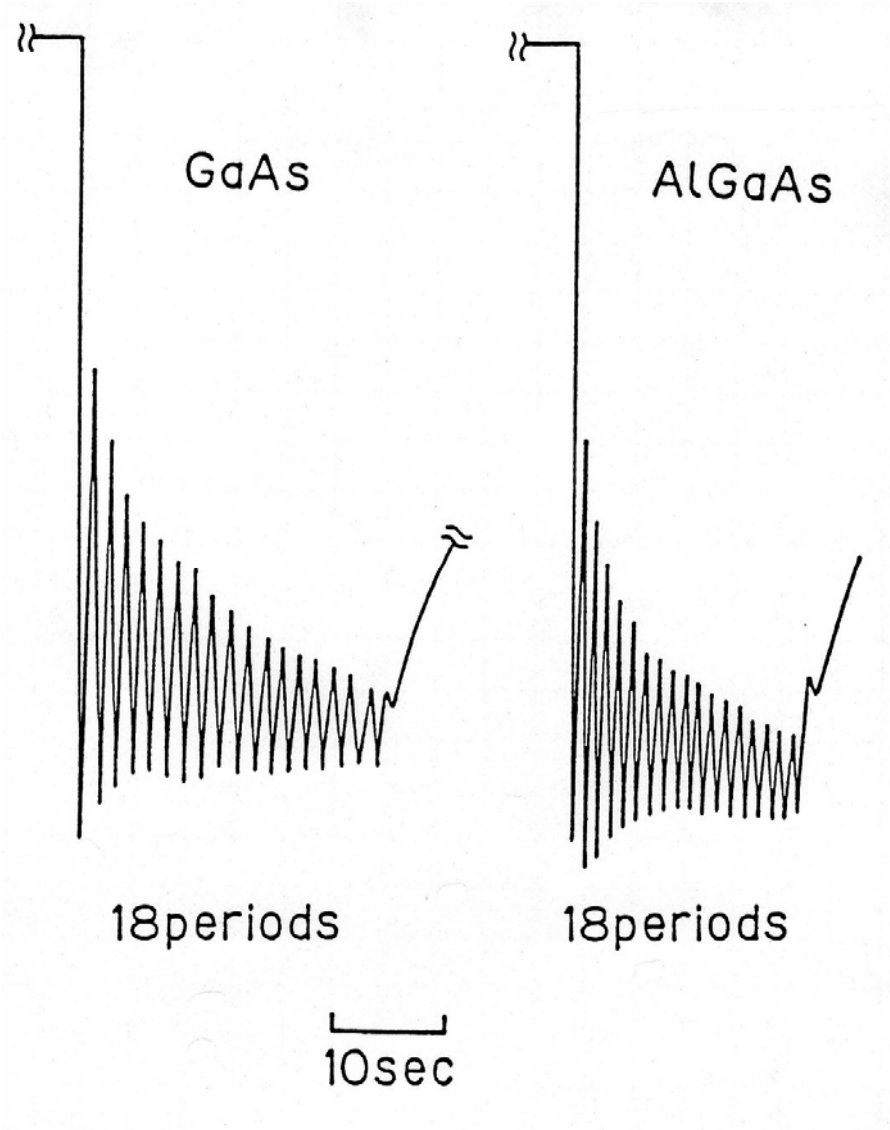

Fig. 2 RHEED intensity oscillation during (100)-GaAs/AlGaAs growth.

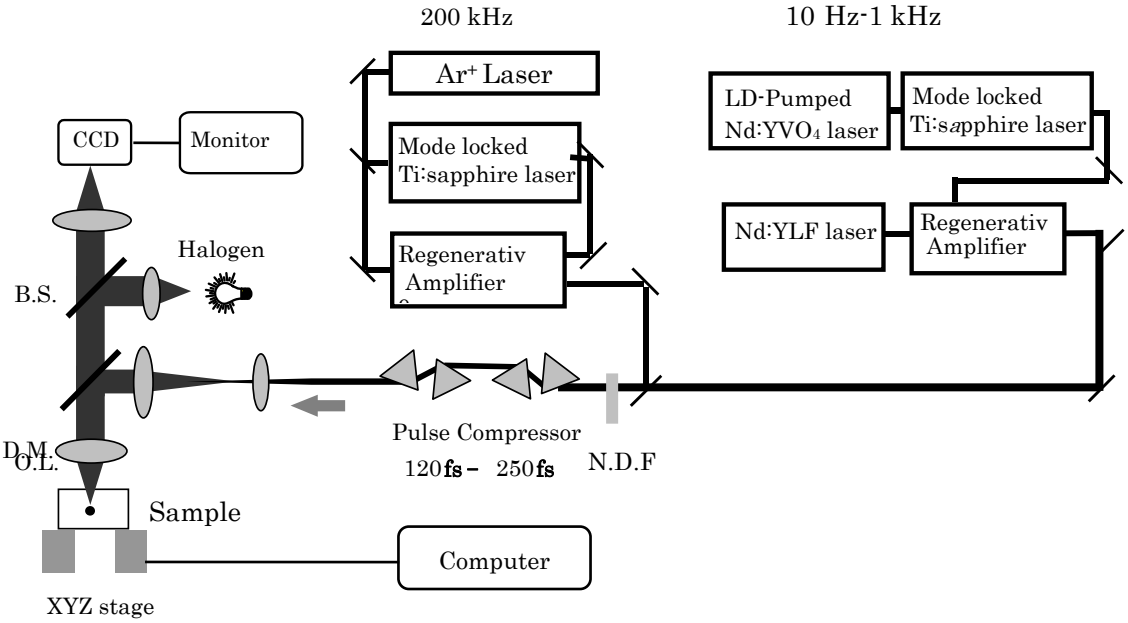

Fig. 3 Schematic diagram of a femtosecond laser.

3. Outline of this Thesis

The outline of this study is as follows.

In Chapter 1, light emitting devices, which are suitable for optical sensing, are described. Next, effects of introducing short-period superlattice structure are also discussed. Moreover, new pin-point LED device suitable for optical sensing is proposed and its characteristics are discussed.

In Chapter 2, ZnO materials are focused which are suitable for ultra violet sensors. The elucidation of ZnO crystal growth mechanism by MOCVD and aqueous solution is described. Moreover, the author has made a prototype of UV sensor fabricated by aqueous solution process and its performance results are presented.

In Chapter 3, an improvement of the sensor sensitivity was tried by using femtosecond laser. Trial to fabricate an anti-reflection structure (ARS) was made using femtosecond pulse laser beam, applied to the surface of photo-detectors, and the device evaluation result is discussed.

In Chapter 1 and Chapter 2, the improvements of the sensing characteristics by using crystal growth technique are explained. In chapter 3, the top down process using femtosecond laser irradiation is discussed.

In Summary, the essential results and discussions through the whole of this thesis are summarized.

Thus, the effects to improve optical sensing characteristics by several nanotechnologies are discussed from the viewpoint of top down processe and bottom up processes.

References

[1] R.N.Hall, G.E.Fenner, J.D.Kingsley, T.J.Solty and R.O.Carlson, Phys. Rev. Lett. **9**, 366 (1962).

[2] M.I.Nethan, W.P.Dumke, G.Burns, F.H.Dill, Jr. and G.Lasher, Appl. Phys. Lett. **62** , (1962).

[3] N.Holonyak, Jr. and S.F.Bevacqua, Appl. Phys. Lett. **1**, 82(1962).

[4] T.M.Quist, R.H.Rediker, R.J.Keyes, W.E.Krag, B.Lax, A.L.McWhorter and H.J.Zeiger, Appl. Phys. Lett. **1**, 91 (1962).

[5] Zh.I.Alferov, V.M.Andreev, D.Z.Garburov, Yu. V.Zhilyav, E.P.Morozov, E.L.Portnoi and V.G.Trofim, Sov. Phys. Semicond. **4**, 1573 (1971).

[6] I.Hayashi, M.B.Panish, P.W.Foy and A.Sumski, Appl. Phys. Lett. **17**, 109 (1970).

[7] H.Kressel and F.Z.Hawrylo, Appl. Phys. Lett. **17**, 169 (1970).

[8] H.C.Casey, Jr. and M.B.Panish, Academic Press, New York, (1978).

[9] S.Arai, M.Asada, Y.Suematsu and Y.Itaya, Jpn. J. Appl. Phys. **18**, 2333 (1979).

[10] I.Hino, A.Gomyo, K.Kobayashi, T.Suzuki and K.Nishida, Appl. Phys. Lett. **43**, 987 (1983).

[11] M.Ishikawa, Y.Ohba, H.Sugawara, M.Yamamoto and T.Nakanishi, Appl. Phys. Lett. **48**, 207 (1986).

[12] I.Yoshida, T.Katsuyama, J.Hashimoto, Y.Taniguchi and H.Hayashi, Electron. Lett. **28**, 628 (1992).

[13] S.Nakamura, M.Sanoh, S.Nakagawa, N.Inase, T.Yamada, T.Matsushita, H.Kiyoku and Y.Sugimoto, Jpn. J. Appl. Phys. **35,** 217 (1996).

[14] S.Nakamura, M.Sanoh, S.Nakagawa, N.Inase, T.Yamada, T.Matsushita, Y.Sugimoto and H.Kiyoku, Appl. Phys. Lett. **70**, 1417 (1997).

[15] A.Evans, J.S.Yu, S.Slinken and M.Razeghi, Appl. Phys. Lett. 85, 2166 (2004)

[16] H.Matsubara, S.Yoshimoto, H.Saito, Y.Jianglin, Y.Tanaka and S.Noda, Science 319, 445 (2008)

[17] D.M.Chapin, C.S.Fuller and G.L.pearson, J. Appl. Phys. **25** 676 (1954).

[18] K.M.Johnson, IEEE, Tran. Electron Devices **ED-12**, 55 (1965).

[19] Zh.I.Alferov, V.M.Andreev, M.B.Kagan, I.I.Protasov and V.G.Trofim, Sov. Phys. Semicond. **4**, 2047 (1971).

[20] R.C.Miller, B.Schwartz, L.A.Koszi and W.R.Wangner, Appl. Phys. Lett. **33**, 721 (1978).

[21] K.Ahmad and A.W.Mabbit, Solid State Elecrtron. **22**, 327 (1979).

[22] H.Ando, H.Kanbe, M.Ito and T.Kaneda, Jpn. J. Appl. Phys. **19**,277 (1980).

[23] F.Cappaso, W.T.Tsang, A.L.Hutchinson and G.F.Williams, Appl. Phys. Lett. **40**, 38 (1982).

[24] E.Munoz, E.Monroy, J.L.Pau, F.Calle, F.Omnes and P.Gibrat, J.Phys. Condens Matter. **13**,7115 (2001).

[25] T.Saito, T.Hitora, H.Ishihara, M.Matsuoka, H.Hitora, H.Kawai, I.Saito and E.Yamaguchi, Metrologia 46, 272 (2006)

[26] Y.Horikoshi, M.Kawashima and H.Yamaguchi, Jpn. J. Appl. Phys. **25**, 868 (1986).

[27] Y.Horikoshi, M.Kawashima and H.Yamaguchi, Appl. Phys. Lett. **50**, 1686 (1987).

[28] T.Sakamoto, N.J.Kawai, T.Nakagawa, K.Ohta and T.Kojima, Appl. Phys. Lett. **47,** 617 (1985).

[29] T.Suntola and J.Hyvaninen, Annual Review of Materials Science, August, **15**, 177 (1985).

Chapter 1

High Performance Semiconductor Light Emitting Devices

1.1 Introduction

Semiconductor optical devices, such as laser diodes and light emitting diodes, are widely used as light sources in a wide variety of applications due to their compactness, relatively high efficiency and well-controlled output.

Regarding optical sensing, there are many applications which require detection of distance, area, object, etc. and getting higher accuracy. The demand for optical device has been summarized as follows: (1) High output power for high sensitivity and long distance sensing, (2) Visible light emission for easy optical alignment, (3) High reliability with high temperature stability, (4) High efficiency and/or low threshold current for low power consumption, (5) Pin-point light source for sensing small target and achieving miniature optical module.
In accordance with the above requirements, improvements of light emitting device characteristics are discussed in detail in this section. At first, optimized crystal growth condition and semiconductor device structure in order to realize low threshold current injection, high luminescent efficiency, visible light and high temperature stability operation are discussed. Next, the author proposes a new pin-point light emitting device and bringing it into the commercial production. Finally, improvements of light output characteristics by using the other crystal axis and new crystal growth method are discussed.

1.2 Improvement of Semiconductor Laser for Sensing Applications

1.2.1 Problems in Semiconductor Laser for Optical Sensing

Visible semiconductor lasers are very important light sources in optical sensing, laser beam printing, optical memory system, and so on. In general, AlGaAs/GaAs double hetero-structure (DH) lasers emitting 780 nm have good temperature stability [1]. However, DH lasers are undesirable because of their low differential quantum efficiency and rather high threshold current (~50 mA). An AlGaAs/GaAs quantum well laser diode lasing at 0.8 μm band shows excellent characteristics [2], of low threshold current and high quantum efficiency. However, when applying the quantum well laser to shorter wavelength below 780 nm, the reproducibility becomes unacceptable caused by the thin GaAs active layer (~40 Å). And the threshold current and the temperature stability become larger and worse, respectively. This can be explained by the reduction of the radiative carrier's recombination probability in the active layer, caused by adjacency between X, indirect conduction band in the barrier, and Γ, direct conduction band in the well. The result is that thermally excited electrons easily leak out into the barrier layer.

Visible, high efficiency, high output and temperature stable light sources were strongly required for optical sensing because of easy optical alignment, high sensitivity, and low power consumption with high reliability. In this section, in order to improve laser characteristics, short period super lattice of various terms were examined.

The respective purposes of this study are described as follows;

1.2.2 To improve efficiency by using strained buffer structures.

1.2.3 To improve threshold current and temperature stability by identifying optimal quantum well active layer structure.

1.2.4 To improve temperature stability with low threshold current by using short period superlattice structure in modified multi-quantum well active layer in visible wavelength.

1.2.2 High Efficiency Quantum-Well Laser Diode by Strained Buffer Layer

A lattice matched AlGaAs/GaAs superlattice buffer (SLB) layers [3] and a GaAs substrate have been widely used in order to improve the device quality of the active layers. The SLB has been successfully applied to optical devices. In particular, a low-threshold current and high-quantum efficiency have been achieved [4] in AlGaAs/GaAs quantum well laser diodes prepared by MBE.

These improvements have been attributed to the capture of impurities, which could originate from either the substrate or from the AlGaAs epi-layers, at the SLB interfaces, or from the atomically smoothing effect by the growth of AlGaAs/GaAs superlattices [3, 5, 6].

However, when looking at the problem of internal stress in the active layer introduced during the cooling from the growth temperature to room temperature after crystal growth, the lattice-matched SLB would not be powerful enough as a buffer layer. The origin of the stress is the mechanical bending of the laser wafer, easily observed after thinning the substrate to fabricate laser diodes, which originates from the difference in thermal expansion coefficients between AlGaAs epi-layers and the GaAs substrate [7]. The problem of the internal stress is more serious when we desire a visible AlGaAs laser diode, in which high-aluminum content is adopted in the cladding layers [8].

A strained superlattice buffer (SSLB) layer lattice mismatched to each other and/or to the substrate seems to be attractive in order to overcome above problems. The SSLB has been successfully applied to the hetero-epitaxial systems, e.g., GaAs/Si and InP/Si, to eliminate threading and misfit dislocations by the relaxation of the stress [9, 10].

This session reports the first successful results of the introduction of SSLB composed of a short period AlGaAs/InGaAs superlattice in a lattice-matched AlGaAs/GaAs laser diode grown by MBE. By the combination of the SLB and SSLB, a high quantum differential efficiency, small cavity loss, and a high-output power operation have been achieved in a ridge waveguide graded

index separate confinement hetero-structure single quantum well (GRIN-SCH-SQW) laser diodes emitting at 770 nm.

First two SQW wafers with SLB alone and with both SLB and SSLB on (100)-oriented GaAs substrate were prepared as shown in Fig. 1.1(a) to demonstrate the ability of SSLB. The SQW was composed of a 50 Å-GaAs well inserted between $Al_xGa_{1-x}As$ (x = 0.5) barrier layers. The wafers were prepared by MBE (ANELVA832) at the substrate temperature of 650°C for AlGaAs and of 570°C for SSLB in order to avoid the adsorption of InAs. The SLB was composed of five pairs of $(Al_xGa_{1-x}As\ (x = 0.5))_{50}(GaAs)_{50}$ superlattice, where the subscript denotes the number of mono-layers [4]. On the other hand, the SSLB was composed of 50 pairs of short period $(In_xGa_{1-x}As\ (x = 0.15))_2(GaAs)_5$ strained superlattice. The composition of In in the lattice-mismatched InGaAs layer was chosen to avoid the problem of critical layer thickness [11], and the number of monolayers were determined by observing the recovery and continuation of the amplitude of specular beam intensity oscillation in the reflection high-energy electron diffraction (RHEED). These conditions assure excellent two-dimensional epitaxial growth. Photoluminescence spectra at 77 K from the SQWs with SLB alone and with both SLB and SSLB are shown in Fig. 1.1(b). Similar values of 20 meV full width at half maxima were observed for the emission from the SQW around 750 nm in two samples. However, the SQW wafer with both SLB and SSLB showed about 5 times higher emission from the SLB packed at around 800 nm, which is due to the multi-quantum well, and is also more intense than the wafer with both SLB and SSLB. Thus, the effectiveness of the SSLB could be verified.

A 770 nm emission GRIN-SCH-SQW laser structure with both SLB and SSLB is shown schematically in Fig. 1.2. The wafer structure was as follows: a 1 μm thick n-GaAs buffer layer (Si-doped, $n \sim 2 \times 10^{18}\ cm^{-3}$), an SSLB and SLB (Si-doped, $n \sim 2 \times 10^{18}\ cm^{-3}$) whose structure was same as mentioned in the above photoluminescence samples, a 1.5 μm thick n-$Al_xGa_{1-x}As$ (x = 0.7) cladding layer (Si-doped, $n \sim 7 \times 10^{17}\ cm^{-3}$), an undoped SQW layer composed of three pairs of a

short period $(Al_xGa_{1-x}As$ (x = 0.28))$_2(GaAs)_5$ superlattice [12, 13] inserted between parabolically graded 0.2 μm thick $Al_xGa_{1-x}As$ barrier layer (x = 0.7-0.28 and 0.28-0.7), a 1.5 μm thick p-$Al_xGa_{1-x}As$ (x = 0.7) cladding layer (Be–doped, p~1×10^{18} cm^{-3}), and a 1 μm thick p^+-GaAs contact layer (Be–doped, p~1×10^{19} cm^{-3}).

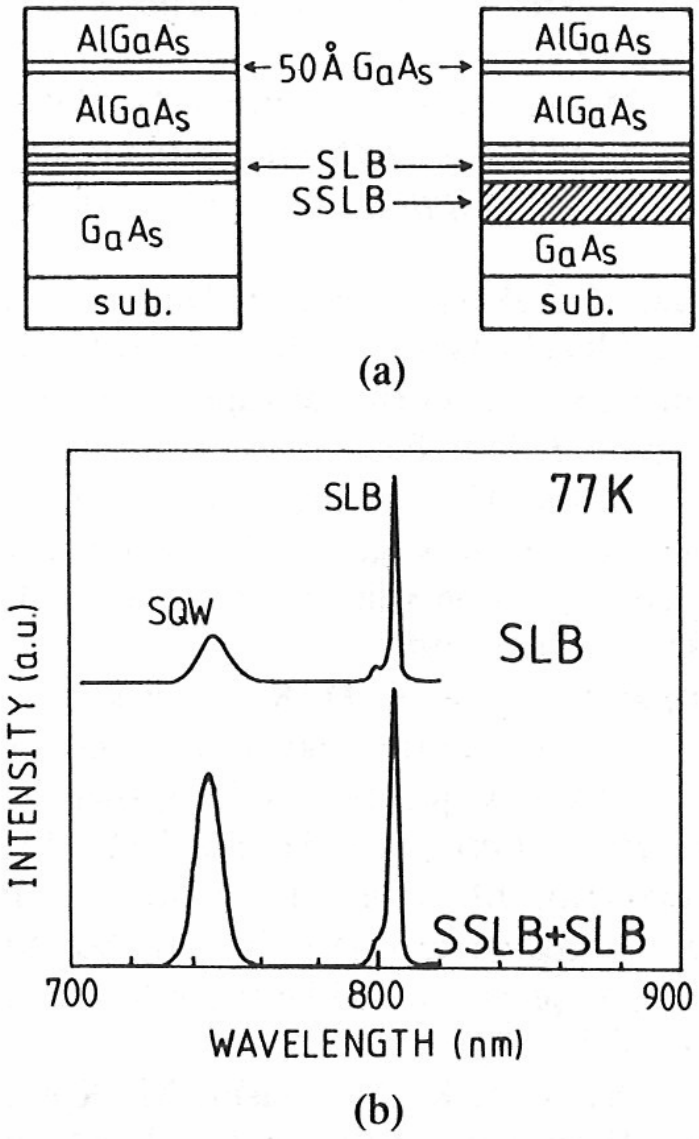

Fig. 1.1 (a) Cross section of the SQW structure with SLB and SSLB, and (b) 77 K photoluminescence spectra from the SQW with SLB alone and with SLB-SSLB.

A ridge waveguide laser diode has been formed in which the ridge is buried in a polyimide with a low thermal expansion coefficient close to that of AlGaAs, in order to reduce thermal stress to the junction and simplifies the wafer processing. A planar configuration, which is suitable for opto-electronics integrations, and for an epi-side down mounts toward high-power operation, has been achieved by an etch-back process. The steps used to process the wafer are shown in Fig. 1.3(a)-(d).

A 4 μm wide and 2.3 μm deep ridge was formed by plasma assisted reactive ion etching in BCl_3 gas (110 sccm, 6 Pa). The RF power density was 0.32 W/cm^2 at 13.56 MHz. A striped Au/Cr ohmic electrode prepared by the lift off process was used as an etching mask [Fig. 1.3(a)]. Special care was taken to control the ridge width and depth in order to assure fundamental transverse mode operation. This experiment achieved a 5 μm thick low thermal expansion polyimide (PIX-L110, Hitachi Chemical, thermal expansion coefficient is 5×10^{-6} K^{-1}) [Fig. 1.3(b)]. The upper layer surface was planer. After a three-step curing of the polyimide (150°C-60 min., 300°C-60 min., and 400°C-30 min.) under N_2 ambient, the top of the ridge was bared by etching the polyimide in O_2 plasma [Fig. 1.3(c)]. After the substrate was thinned to 100 μm, an ohmic metal, Au/AuGeNi, and a bonding Metal, Au/Cr were evaporated onto the n and p side, respectively, and were metalized in infrared flash lamp anneal furnace at 410°C for 30 sec. [Fig. 1.3(d)]. Laser with a cavity length of 300 μm was fabricated by cleaving the wafer and soldered on silicon sub-mounts with Au-Sn in epi-side down configuration. The measured thermal resistance was as low as 50 ± 10°C/W, which is less than half of the 100°C/W measured for devices with p-side-up mount.

Figure 1.4 shows a typical power output versus injected current under CW operation at 25°C for 675 μm long PBR laser without facet coatings. Power output is almost linear to above 50 mW/facet. Temperature dependence of the threshold current showed a rather high characteristic temperature, T_0, of 180 K.

An excellent characteristic in the present PBR laser with SSLB has been found in the quantum efficiency. In Fig. 1.5, differential quantum efficiency η_d has been depicted as a function of the cavity length between 300 μm and 3200 μm. According to the well-known equation.

$$\eta_d^{-1} = \eta_i^{-1}[\alpha L + \ln(1/R)]/[\ln(1/R)] \qquad \cdots\cdots\cdots\cdots (1)$$

where η_i, α, L, and R represent the internal quantum efficiency, the cavity loss, the cavity length, and the facet reflectivity respectively; parameters were determined from the best fit. A very high-efficiency η_i of 0.95 and small loss factor α of 3 cm^{-1} were obtained. These values should be compared to the best values reported so far in similar MBE grown narrow ridge waveguide GRIN-SCH-SQW laser with SLB by Wada et al. [14], 0.90 and 5.3 cm^{-1} for η_i and α respectively. Their results are shown in Fig. 1.5 by broken lines for reference.

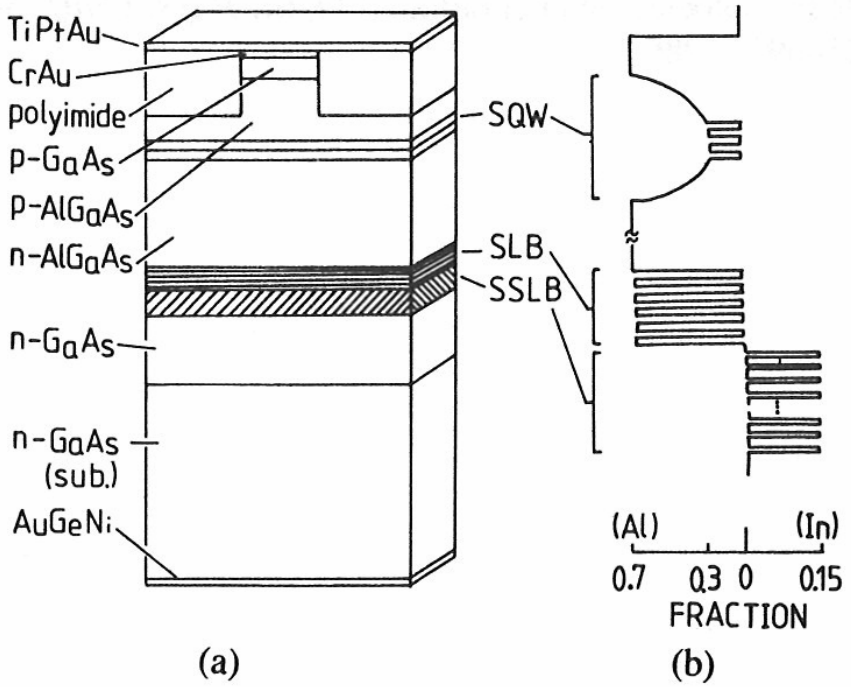

Fig. 1.2 (a) Cross section of the polyimide buried ridge waveguide GRIN-SCH-SQW laser diode with the SLB-SSLB, and (b) Al and In mole fraction for each layer.

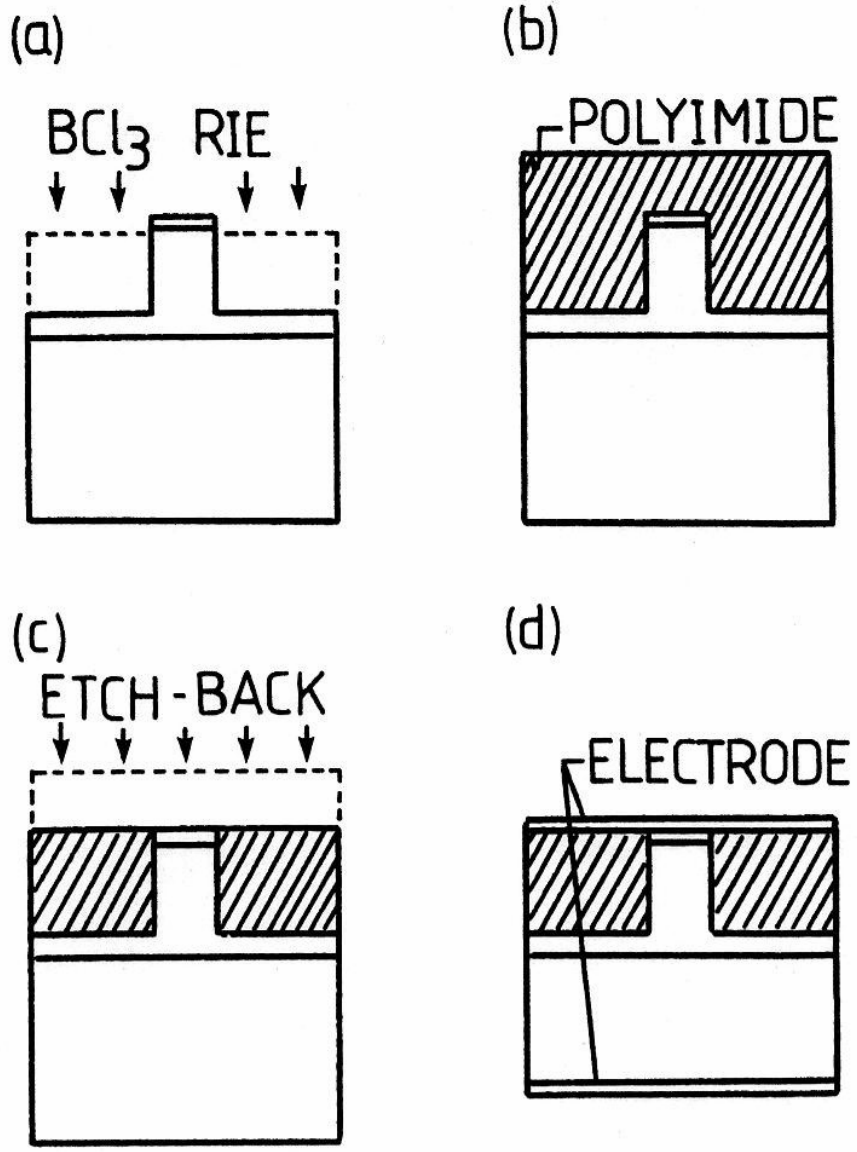

Fig. 1.3 Fabrication of the PBR laser: (a) ridge formation, (b) burying the ridge by polyimide, (c) etch-back process, (d) electrode formation.

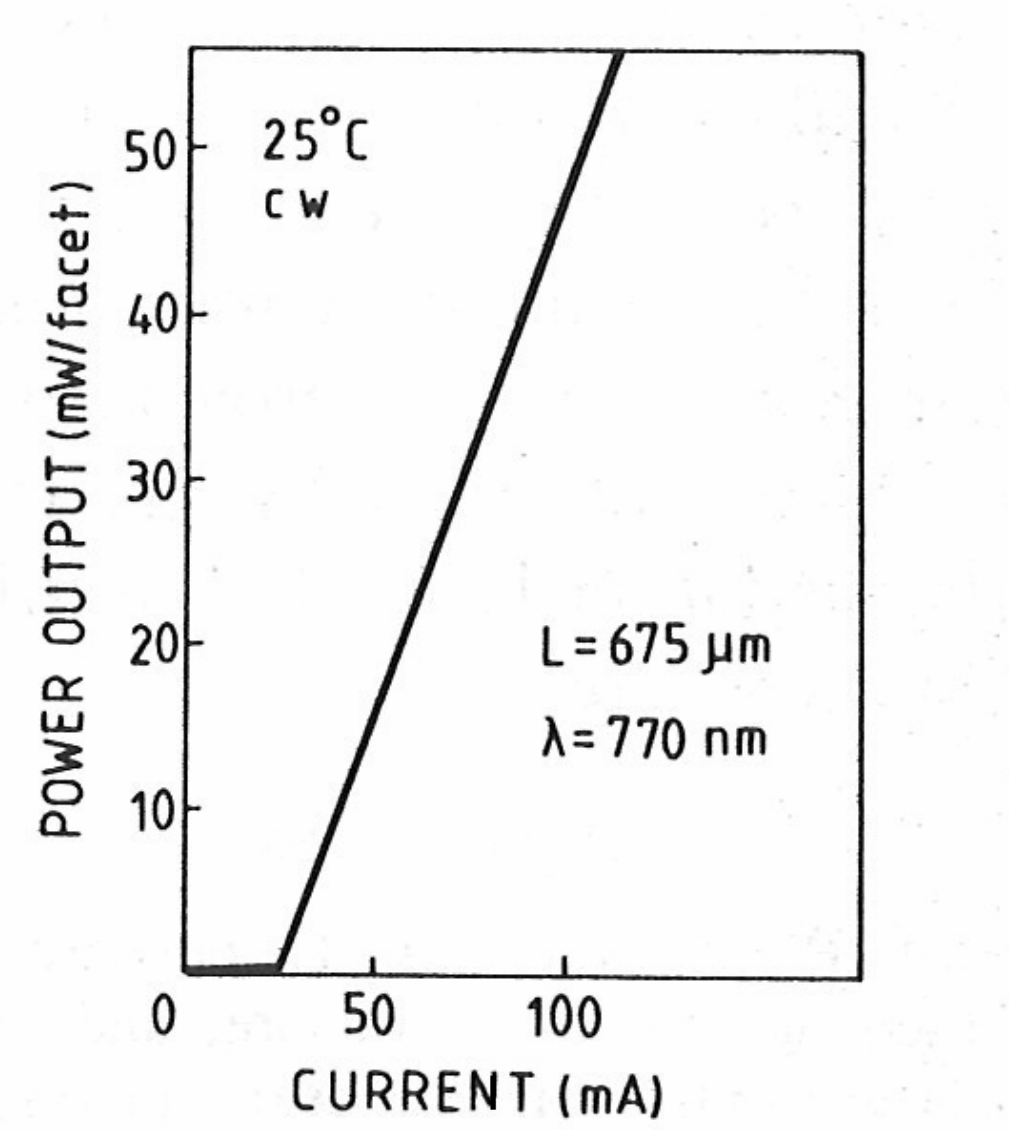

Fig. 1.4 Typical Light output-current characteristics of the GRIN-SCH-SQW laser diode under CW operation at 25°C.

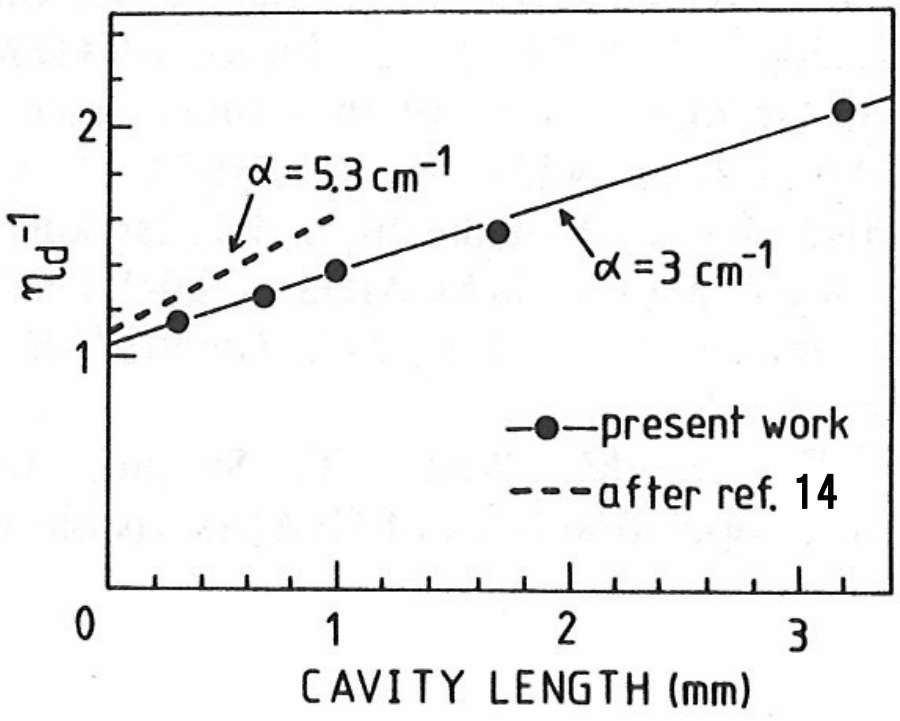

Fig. 1.5 Reciprocal of the differential quantum efficiency $\eta_{d\text{-}1}$ as a function of cavity length L.

1.2.3 High Efficiency Quantum Well Laser Diodes with Short Period Superlattice Barriers

AlGaAs/GaAs lasers emitting at around 780 nm were widely used. However, usually when shorter wavelengths are achieved, laser characteristics become poorer. In particular, threshold current density is increased [15, 16].

This degradation has been explained by non-uniformity in GaAs wells which are thinner than 40 Å caused by the hetero-interface roughness. To overcome such a problem, an $(AlGaAs)_m(GaAs)_n$ short period superlattice well, where the subscripts denote the number of mono-layers, has been proposed by Hayakawa et al [13]. This structure gives a thicker well which contributes to decrease the influence of interface roughness. The author applied this superlattice well structure to a polyimide buried ridge (PBR) waveguide laser emitting at 780 nm and achieved low current threshold characteristics. However, the temperature dependence was not so good in comparison with that prepared by liquid phase epitaxy (LPE). The reason for the poor temperature characteristics was supposed to be the employment of Al atoms in the well. Since AlAs is less mobile than GaAs [17], the optical quality of AlGaAs is lower than GaAs. Furthermore, in deposition like crystal growth in MBE and MOCVD, Al metal is not as pure as what expected in LPE under H_2 ambient. Therefore, we should not employ AlGaAs in the well. If the barrier-well interface flatness is improved, a GaAs quantum well laser emitting below 800 nm can be expected to have excellent characteristics. In order to improve the interface quality, a migration enhanced epitaxy (MEE) was used, and laser diodes were successfully growing at very low temperature of 350°C [18]. The MEE method, however, is not practical because of time consumption and excessively frequent shutter on-off. Therefore, an $(AlGaAs)_m(GaAs)_n$ short-period superlattice barrier layer is proposed instead to improve the interface flatness between AlGaAs barrier and GaAs quantum well. Using the superlattice barrier, a laser diode was successfully fabricated with high temperature stability and low threshold current having a graded index

separate confinement hetero-structure (GRIN-SCH) with a thin GaAs quantum well (38 Å). A GRIN-SCH laser emitting at 780 nm was grown on a (100) oriented Si-doped n-type GaAs substrate by MBE (ANELVA832) at 650°C. The laser subsequence was as follows: a Si doped n-GaAs buffer layer (2 μm, n ~2 × 10^{18} cm^{-3}), a Si doped superlattice buffer layer [4] composed of ten periods of n-GaAs (15 nm) and n- $Al_xGa_{1-x}As$ (x = 0.85, 15 nm), buffer layer (2 μm, n ~2 × 10^{18} cm^{-3}), a Si doped n- $Al_xGa_{1-x}As$ (x = 0.85) cladding layer (1.5 μm, n ~1 × 10^{18} cm^{-3}), an undoped $Al_xGa_{1-x}As$ GRIN layer (x is parabolically graded from 0.85 to 0.5, 150 nm), an undoped active layer region, an undoped $Al_xGa_{1-x}As$ GRIN layer (x = 0.5-0.85, 150 nm), a Be-doped p- $Al_xGa_{1-x}As$ (x = 0.85) cladding layer (1.5 μm, p~2 × 10^{18} cm^{-3}), and a Be-doped GaAs cap layer (1 μm, p~1 × 10^{19} cm^{-3}).

The laser structure is a PBR waveguide [12] as shown in diagrammatic form in Fig. 1.6 (a). The ridge width and depth are 5 and 2.3 μm, respectively. Figure 1.6 (b) shows the construction of the active layer: a double quantum well structure is shown as an example. The superlattice barriers near the GRIN region are composed of 50 nm $(Al_xGa_{1-x}As$ (x = 0.5))$_2(GaAs)_2$ short period superlattice which have an average Al mole fraction of 0.25.

The intermediate layer coupling barrier superlattices between two GaAs wells is 10 nm thick. The GaAs well thickness is set to be 38 Å to obtain 780 nm emission.

The author prepared a single quantum well (SQW), a double quantum well (DQW), and a triple quantum well (TQW), each containing one GaAs well, two wells, and three wells, respectively.

First, a SQW laser was tested. The T_0 value of 180 K was high enough: however, the threshold current density (J_{th}) of 700 A/cm^2 was rather high in the broad area laser (300 x 300 μm^2). This high J_{th} could be due to carrier leakage caused by the thin well.

The DQW PBR laser was the next to be examined. Figure 1.7 (a) shows the light output-current characteristic at various heat sink temperatures for

the DQW laser. A low threshold current of 20 mA and a high differential quantum efficiency of 75 % were obtained at 20°C. The threshold currents were plotted as a function of ambient temperatures as shown in Fig. 1.7 (b). The characteristic temperature To was as high as 205 K between 20 and 70°C and 114 K between 110 and 150°C. An extremely low threshold current density of 260 A/cm^2 in a broad area (300 × 300 μm^2) laser has been achieved. In spite of two quantum wells, the threshold current density is low enough in comparison with the value in those reported in single quantum well lasers [15, 19].

The fundamental transverse mode operation was observed over 30 mW both in parallel to and perpendicular to the junction plane. CW emission spectra for different light output powers are shown in Fig. 1.8. The lasers were operated in a single longitude mode at a wavelength of 780 nm. Longitudinal mode shifted linearly against power output, and mode hopping did not occur up to 30 mW; however, the stable longitudinal mode operation reported by Garret et al. [20] could not be observed.

In the TQW laser, no definite difference in laser characteristics (temperature dependence, quantum efficiency, lasing spectra, and so on) was observed in comparison with the DQW laser except for an increase in threshold current due to the increase of the number of wells. Thus, the author concludes that two wells (DQW) are enough.

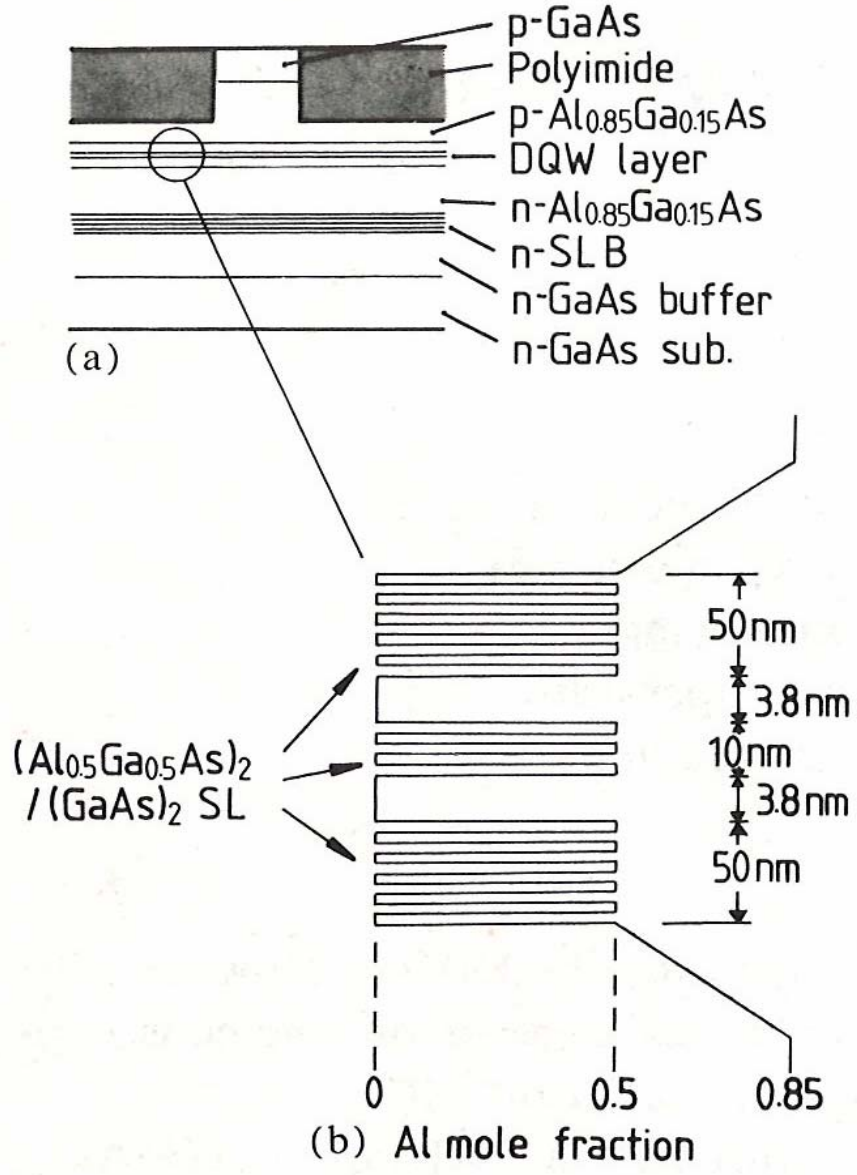

Fig. 1.6 (a) Schematic diagram of a PBR waveguide laser, and (b) Al mole fraction of DQW active layer.

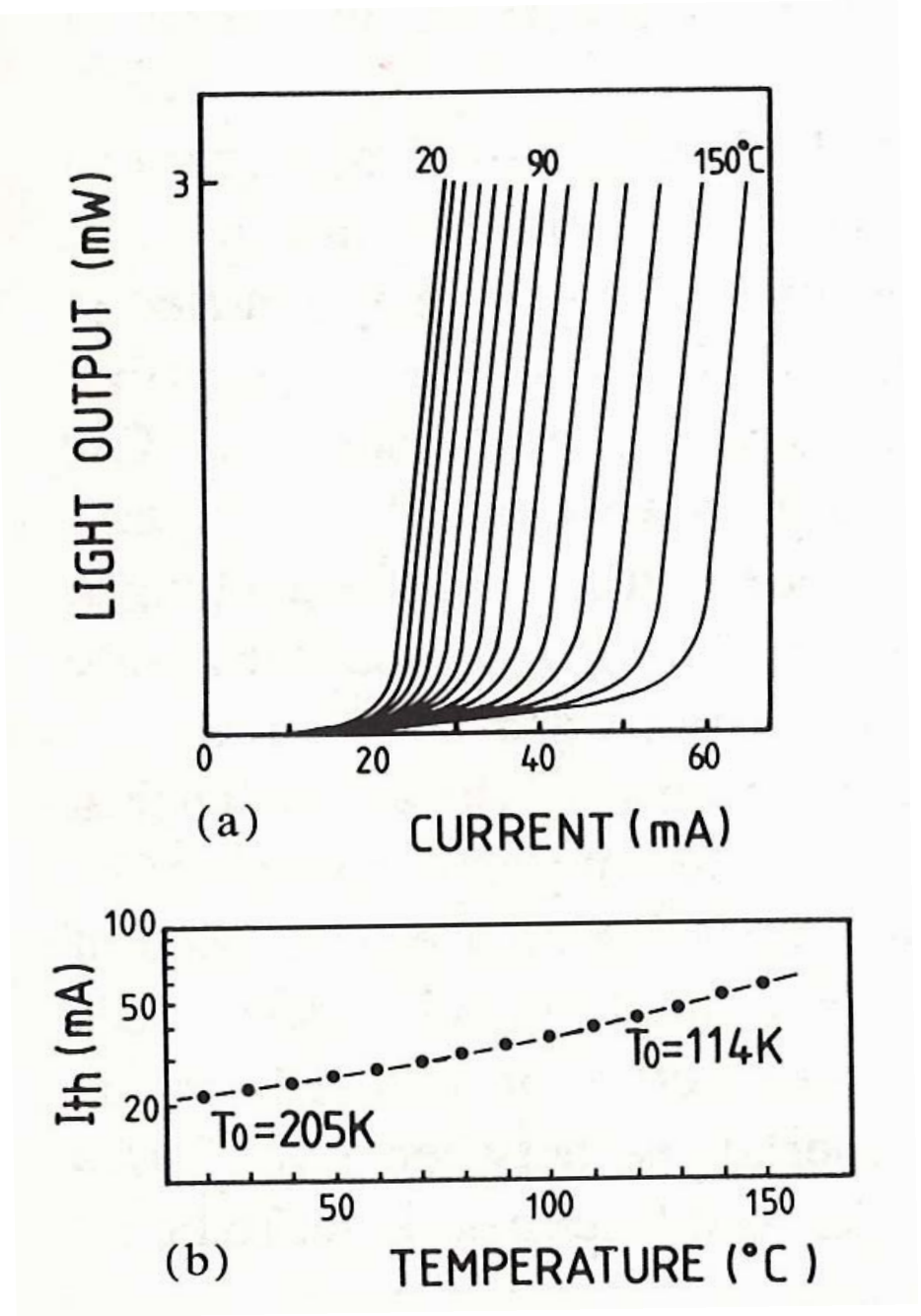

Fig. 1.7 (a) Light output-current characteristic per facet, and (b) The threshold current plotted at various temperatures.

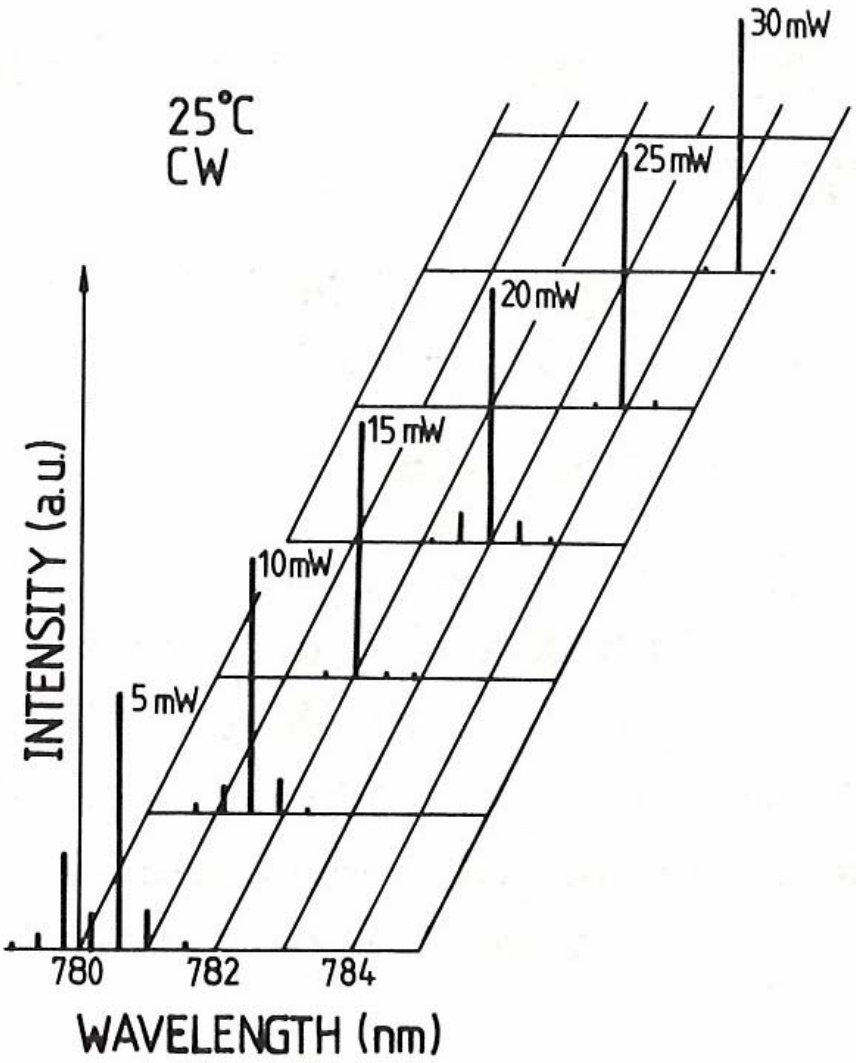

Fig. 1.8 CW emission spectra for different light output power at 25°C.

1.2.4 Visible Laser Diode Composed of AlGaAs Short Period Superlattice Active Layer

When applying the quantum well (QW) laser to shorter wavelength below 750 nm, the threshold current increases and temperature stability deteriorates, because of the reduction of carrier recombination probability caused by adjacency between the X and Γ bands.

In order to reduce the overflow of carriers, the multi-quantum well (MQW) structure seems to be useful because of its wide active layer, and furthermore the modified MQW seems to be effective for lower threshold current [21].

Therefore, the author applied short period $(AlGaAs)_m(GaAs)_n$ superlattices to a GRIN-SCH (GRaded INdex, Separate Confinement Hetero-structure) MQW laser diode emitting at 720 nm.

Both barriers and wells in the MQW region were prepared by short period superlattices, and the MQW structure is easily employed without changing the Al molecule flux.

A GRIN-SCH laser emitting at 720 nm was grown on a (100) oriented Si-doped n-type GaAs substrate by MBE at 650°C. The growth rate was measured by the oscillation period of the reflection high-energy electron diffraction (RHHED) intensity in the run just prior to the laser wafer growth.

The layer sequence of the laser diode was as follows: an n-GaAs buffer layer (2 μm, Si 2×10^{18} cm^{-3}), a superlattice buffer layer [4] composed of ten periods of n-GaAs (15 nm) and n-$Al_xGa_{1-x}As$ (x = 0.85) (15 nm), an n-$Al_xGa_{1-x}As$ (x = 0.85) cladding layer (1.5 μm, Si;1×10^{18} cm^{-3}), an undoped $Al_xGa_{1-x}As$ GRIN layer (x = 0.45-0.85), an undoped quantum well region, an undoped $Al_xGa_{1-x}As$ GRIN layer (x = 0.45-0.85), a p-$Al_xGa_{1-x}As$ (x = 0.85) cladding layer (1.5 μm, Be; 2×10^{18} cm^{-3}), and a p-GaAs cap layer (0.5 μm, Be; 1×10^{19} cm^{-3}).

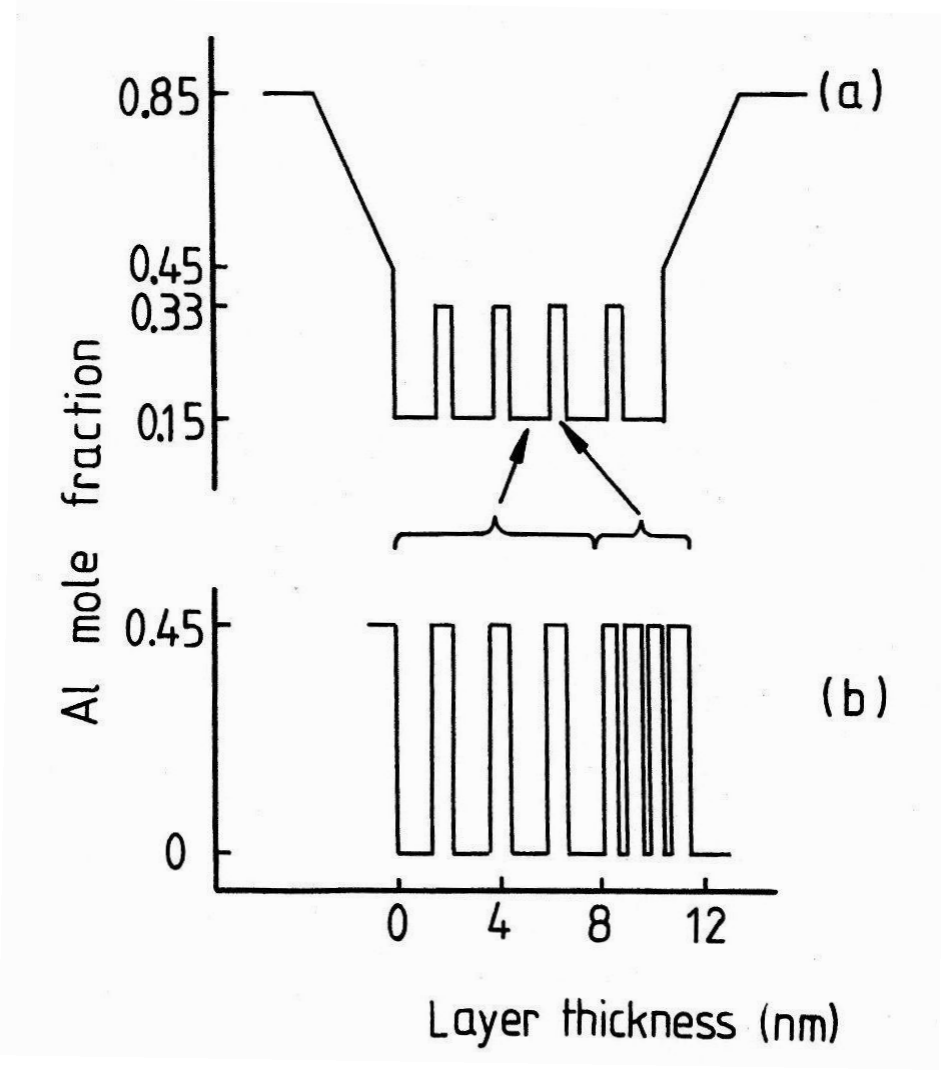

Fig. 1.9 Al mole fraction profile of Modified MQW structure
a) Average Al mole fraction
b) Al fraction of superlattice well and superlattice barrier

Figure 1.9 shows the Al mole fraction around the MWQ active region. The MQW region consisted of five quantum wells. The $(AlGaAs)_m(GaAs)_n$ short period superlattice were adopted for both wells and barriers. The wells and barriers were consist of 80 Å thick $Al_xGa_{1-x}As$ (x = 0.45))$_2(GaAs)_2$ superlattices and 30 Å-thick $Al_xGa_{1-x}As$ (x = 0.45)$_2(GaAs)_2$ superlattices, respectively, as shown Fig. 1.9(a). The average Al mole fractions for wells and barriers were 0.15 and 0.33, respectively, as shown in Fig. 1.9(b).

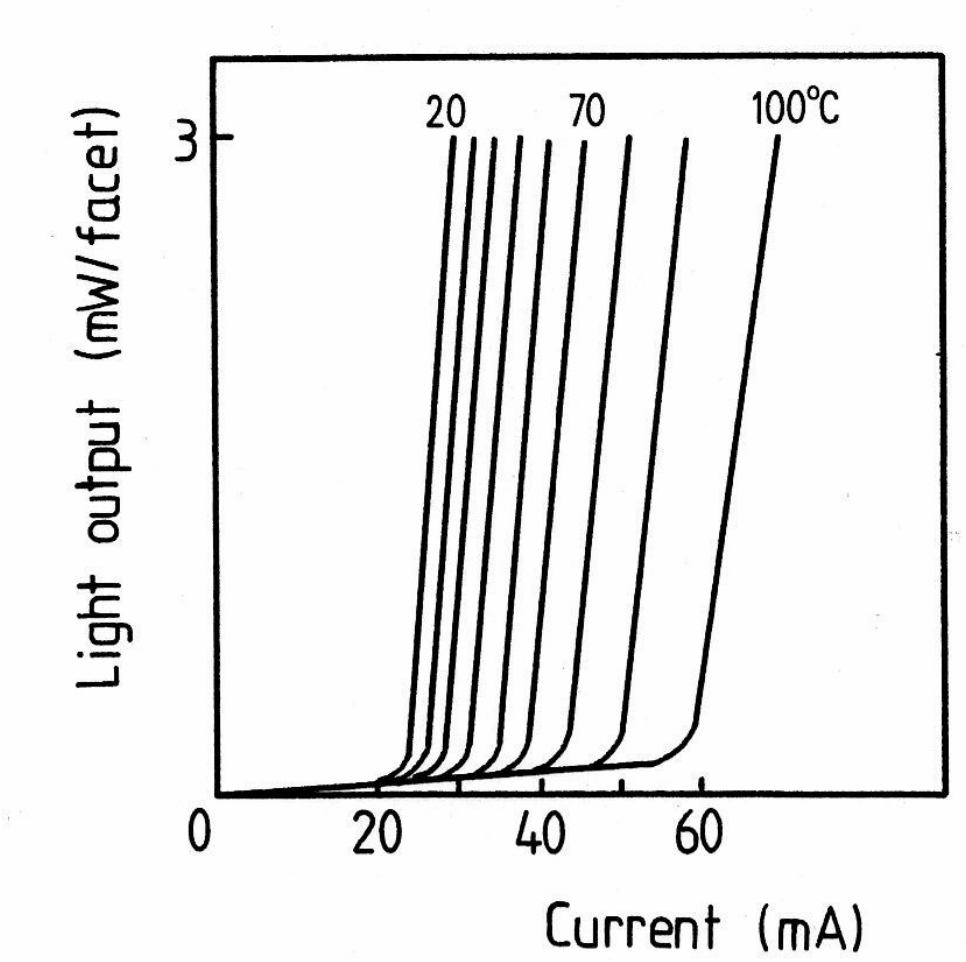

Fig. 1.10 Light output characteristics at various temperatures under CW operation.

Thus the barrier height is lower than the carrier injection level (x = 0.45); the improvement of laser characteristics has been expected for the reason proposed by Tsang [21]. The temperature dependence of typical CW light output/current curves is shown in Fig. 1.10.

A low threshold current of 24 mA with lasing at 720 nm and high temperature operations at over 100°C have been achieved. The differential quantum efficiency is as high as 75 %. The characteristic temperature T_0 for the threshold current in the form of exp (T/T_0) is 175 K up to 90°C under pulsed operation of this sample. These excellent results are considered to be caused by short period $(AlGaAs)_m(GaAs)_n$ superlattices in the active layer region to form a modified MQW structure.

1.2.5 Discussion

Three types of laser diodes by short period superlattices were proposed and examined.

At first, the strained superlattice buffer layer has been proposed for the lattice matched AlGaAs/GaAs system. By the introduction of short period InGaAs/GaAs strained superlattice buffer layer, a high differential quantum efficiency (η_d> 50 % even at 3 mm long cavity), a small cavity loss ($\alpha \sim 3\ cm^{-1}$), a high internal quantum efficiency ($\eta_i \sim 0.95$), and a high-output power have been achieved in a 4 μm wide ridge waveguided 770 nm GRIN-SCH-SQW laser diode. These improvements could be due to the relaxation of internal stress by the introduction of the strained superlattice buffer layer. The detail physical origin has not been clarified. However, one possible explanation could be similar to the hetero-epitaxial system. The internal stress originating in the mechanical bending introduced into the active layer during the cooling from the crystal growth temperature to the room temperature could be relaxed by the large lattice vibration originating in the lattice matched superlattice.

Next, AlGaAs/GaAs short period superlattice was applied to the barrier

layer with thin GaAs quantum wells. As the result of optimization of well number, a low threshold current density of 260 A/cm^2 and a high characteristic temperature of 205 K have been achieved in a ridge waveguide GRIN-SCH laser diode emitting at 780 nm.

Thirdly, AlGaAs/GaAs short period superlattices were applied to the modified multi quantum well active region. A short wavelength of 720 nm and high temperature CW operation at over 100°C were achieved with low threshold current of 24 mA and high quantum efficiency of 75 % at room temperature.

The reasons of these superior characteristics are considered as follows: Through the application of AlGaAs/GaAs short-period superlattice, (1) the hetero interface flatness between the short period superlattice barrier layer and the quantum well was improved because of the large diffusion length of Ga atoms in MBE growth. (2) a high quality AlGaAs quantum well crystal was obtained by the effect of trapping residual impurities in the barrier layer before quantum well growth, (3) AlGaAs-related defects and non-radiative recombination centers, were stopped, and (4) the strain at the hetero interface was reduced.

1.3 Demonstration of Visible High Power Pin-point LED

1.3.1 Problems in Light Emitting Diode for Optical Sensing

Recently, visible light emitting diode (LED) is widely used for traffic information, illumination, signals and lighting with the advantages of small size, light weight, low current consumption, and high reliability in comparison with the bulb light sources. The market volume is rapidly expanding because of recent improvement in light output characteristics.

In the optical sensing market, visible red LEDs having emitting wavelength of around 650 nm, were widely used for photo-interrupter and photoelectric switches because they work as a sensing light source and an indicator of operation at the same time. Moreover, the red emissions around 650 nm were suitable for optical fiber sensors because of low optical absorptions in the plastic optical fibers.

Recently, higher sensing accuracy and longer distance sensing without additional cost were required. Corresponding to these requirements, a small pin-point light source was desired for optical sensing, i.e. laser diode, super-luminescent diode and so on.

But, in general, the laser diode (LD) and super-luminescent diode (SLD) have some problems in comparison with LED. The controversial points of LD and SLD in comparisons with LED are described as follows: (1) higher production cost because of their complicated structure and some additional production process, i.e. scribing process, facet coating, mounting on a heat sink, screening test and so on, (2) sensitive to temperature fluctuations, (3) shorter operational life time, and (4) hard to use for eye safety (IEC 60825-1).

Therefore, a new pin-point light emitting diode with current confinement structure was suggested in order to satisfy these requirements and overcome the above problems, simultaneously.

1.3.2 Design of AlGaInP Pin-Point LED

The various LED structures are shown in Fig. 1.11. From the viewpoint of emission areas, these LED structures are classified into the group (a), (b) and the group (c), (d). The emission areas of the group (a), (b) are the whole chip. On the other hands, the emission areas of the group (c), (d) are centralized by using electrode masks. The center emission structures are effective for obtaining small focal spots and narrow beams. Therefore, the LEDs with large emission area are suitable for lighting and signs, and the center emission LEDs are suitable for sensing applications.

The structures of Fig. 1.11(b) and (d) have a current blocking layer near the active layer. The function of these layers is preventing the light emission under the electrode. Therefore, the external quantum efficiency is improved. For use in optical sensing, Fig. 1.11(d) structure, which has central emission with pi-point light emitting area and current confinement structure, is suitable for optical sensing applications. We call this LED structure with small light emitting area as “pin-point LED”.

The compound semiconductor materials emitting at 650 nm are GaP, GaAsP, AlGaAs and AlGaInP. Among these candidates, the AlGaInP quaternary alloys are the most promising materials for the 650 nm emitting wavelength region because this material has the widest direct bandgap among semiconductor compounds completely lattice matched to a GaAs substrate.

The author has developed a new pin-point LED emitting at 650 nm. The schematic diagram of the LED structure is shown in Fig. 1.12. The structure of the LED was grown on a (100) oriented Si-doped n-type GaAs (Si; 1×10^{18} cm^{-3}) substrate by MOCVD. The layer sequence of the LED was as follows: an n-GaAs buffer layer (1.5 μm, Si; 1×10^{18} cm^{-3}), 50 pairs of n-AlAs / $Al_xGa_{1-x}As$ (x = 0.5) Bragg reflector (the layer thickness is λ/4n, Si; 1×10^{18} cm^{-3}), n-type InAlGaP cladding layer (1.5 μm, Si; 5×10^{17} cm^{-3}), undoped InGaP active layer (0.5 μm), p-InAlGaP cladding layer (1.5 μm, Zn; 5×10^{18} cm^{-3}), and a p-GaAs contact layer (0.2 μm, Zn; 1×10^{19} cm^{-3}). After the epitaxial growth, a pin-point

LED with current confinement structure as shown in diagram form in Fig. 1.12 was fabricated. The LED process flow is described as follows; (1) the above InAlGaP LED structure was grown by MOCVD technique. (2) The current confinement structure was formed by proton (H^+) implantation (100 keV, dose of $1\text{-}10^{15}$ cm^{-2}) and the wafer was slightly annealed in infrared flash lamp anneal furnace at 350°C for 1 minute. (3) Au/Cr electrode was evaporated on to the top surface, and AuGeNi / Au metals was evaporated on the back-side of the wafer and alloyed at 410°C for 1 minute in the flash lamp anneal furnace to form ohmic contacts. (4) Etching of the GaAs cap layer in order to reduce the absorptions of the light from active layer. (5) Separating the chips by the dicing process.

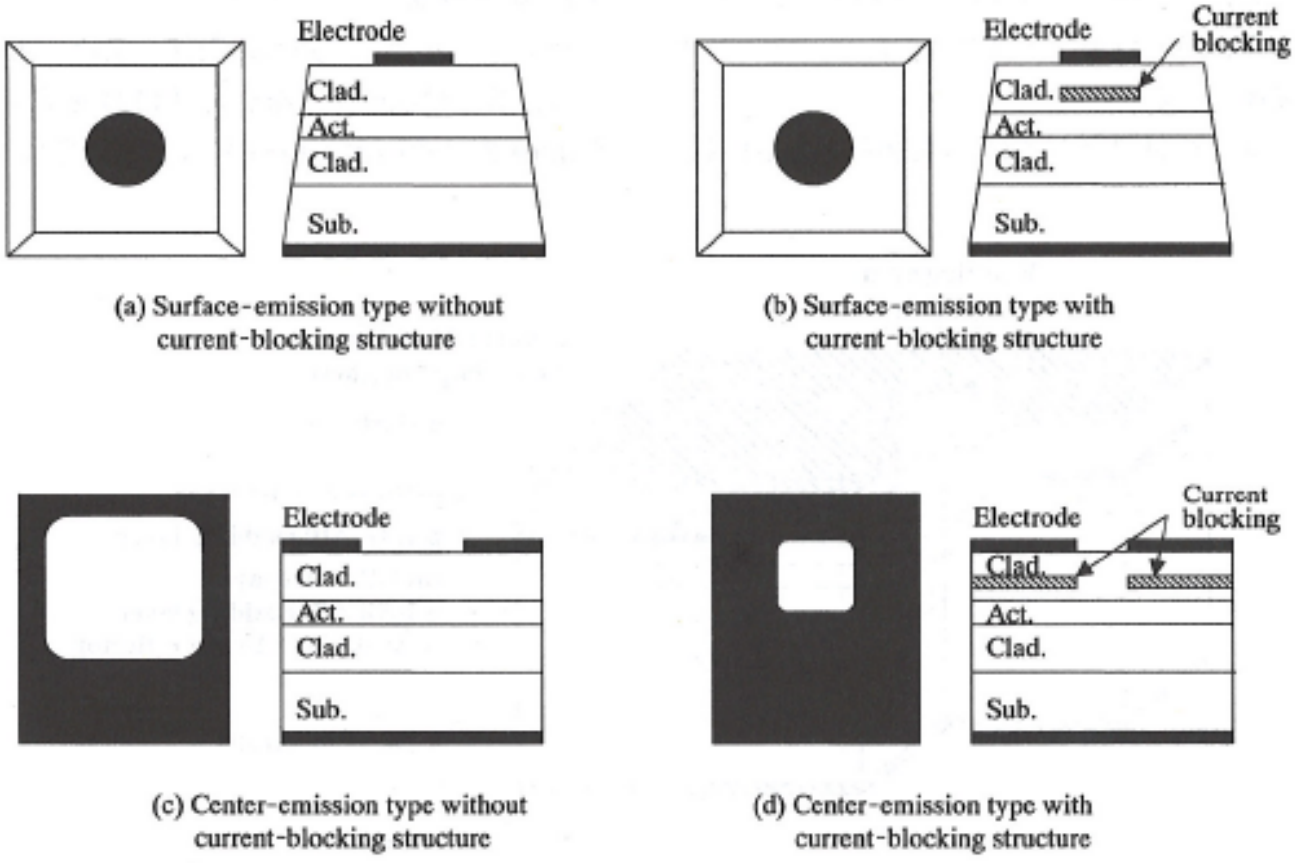

Fig. 1.11 Chip structures of LEDs.

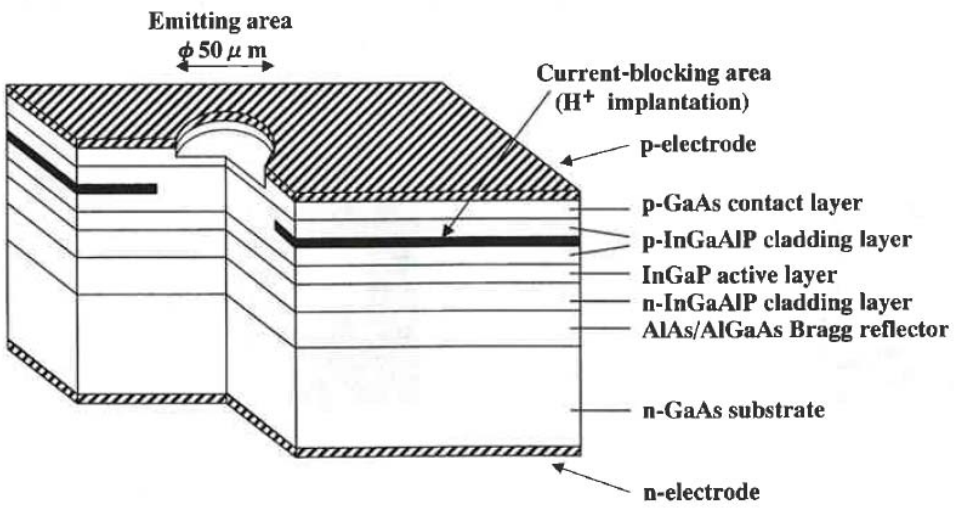

Fig. 1.12　Chip structures of InGaAlP pin-point LED.

1.3.3 Device Characteristics and Reliability

The emission area of ϕ50 μm was shown in this Fig. 1.12, the emission diameters can be chosen arbitrarily. The specifications of this pin-point LED assembled in a plastic package are shown in Table 1.1. The external quantum efficiency of the pin-point LED was 2.1 %, which was around 1/3 of the efficiency of the conventional whole emission LED, and this value was caused by restricted emission areas.

Figure 1.13 shows the near field pattern (NFP) at 20 mA forward current. The light output of center of the emission area was weak. This indicates that the current has not been spread sufficiently because of the high resistivity of p-InGaAlP cladding layers [22]. Moreover, this phenomenon becomes worse with larger emission area. Therefore, the author suggested introducing a new electrodes mesh structure in order to spread the current to the active layer sufficiently and their NFP is shown in Fig. 1.14.

Figure 1.15 shows the light-output characteristics and NFP's of pin-point LED of 50 μm diameter with and without mesh electrodes. The light output of the LED with mesh electrode is around 30 % higher than that of the LED without mesh electrode. This indicates that the mesh electrodes structure has contributed to improve the external quantum efficiency and obtain higher light output. As the result, this pin-point LED with mesh electrode was applied to OMRON photoelectric switches produced as model E3T.

Samples of the pin-point LED of 50 μm diameter in plastic package were aged for a constant current operation at various conditions as shown in Fig. 1.16. The aging conditions were 25°C 40 mA, 85°C 8 mA, -25°C 8 mA and -25°C 40 mA. After 15,000 hour aging test, all the samples did not show a notable degradation. This LED has exhibited high reliability both in yield and longevity despite its high current density. The LED's operational life time (τ) is

estimated by the equation below. The τ is defined as the time taken to degrade 50 % of the initial output power.

$$\tau = \frac{\log 2}{\beta} \exp \frac{Ea}{k / Tj} \qquad \cdots\cdots\cdots\cdots (2)$$

β :degradation coefficient
k: Boltzmann constant
T_j: junction temperature
Ea: activation energy

As the result, the activation energy Ea was 0.55 eV and the τ was estimated to be above 100,000 hours for DC operation. These aging results were sufficient for sensing use in pulsed operations.

Figure 1.17 shows the accelerated aging test results of DC operation in the inferior condition of 85°C 85 % with forward current (If) of 5 mA DC in comparison with AlGaAs conventional LED. This high humidity reliability test item is effective to confirm the quality of the LED. To estimate the passivation effect on reliability, two types of pin-point LEDs were tested, one with the GaAs cap layer completely removed, and the other with the GaAs thin layers slightly left for ~ 100 Å.

The light degradation of the conventional AlGaAs LED was around 50 % for 1000 hours. On the other hand, the light output power of pin-point LED with GaAs passivation did not changed over 1000 hours. Thus, this InGaAlP pin-point LED was confirmed to have high enough reliability even at high current densities in comparison with the conventional AlGaAs LED and was successfully put into commercial production as shown in Fig. 1.18.

Table 1.1 Main specifications of AlGaInP pin-point LED molded in plastic package.

Ta = 25°C

Item	Symbol	Condition	Specification
Emitting Area			φ50 ± 5 μm
Operating Temperature	Ta		-25 - 85°C
Forward Current	If	Ta = 25°C	Max. 40 mA
		Ta = 85°C	Max. 8 mA
Output Power	Po	If = 20 mA	Typ. 0.9 mW Min. 0.5 mW
Forward voltage	Vf	If = 20 mA	Typ. 2.1 V Max. 2.6 V
Reverse Current	Ir	Vr = 4V	Max. 60 μA
Peak Wavelength	λ	If = 20 mA	Typ. 670 nm

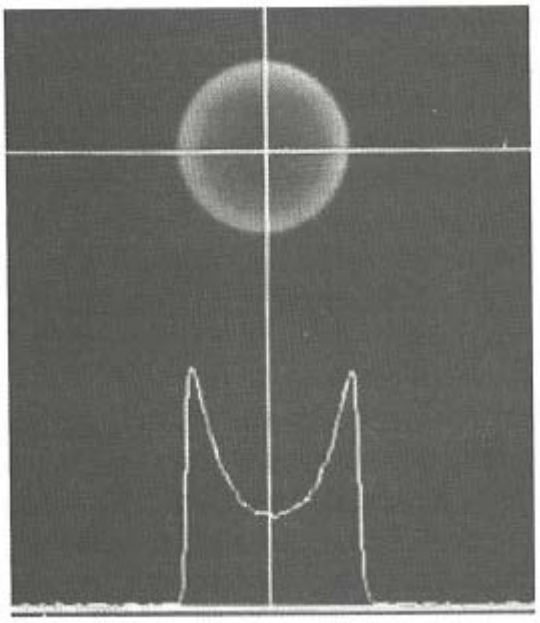

Fig. 1.13 Near field patterns of AlGaInP pin-point LED.

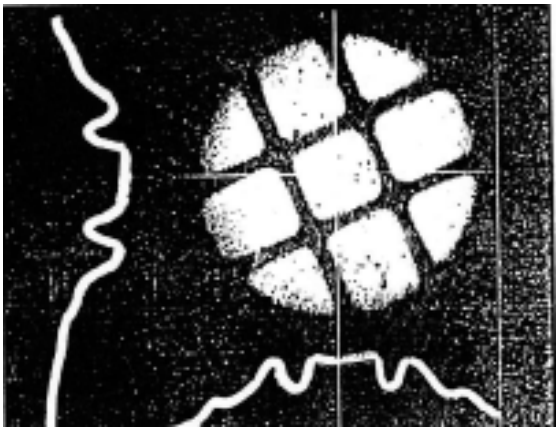

Fig. 1.14 Near field pattern of AlGaInP pin-point LED with mesh electrode.

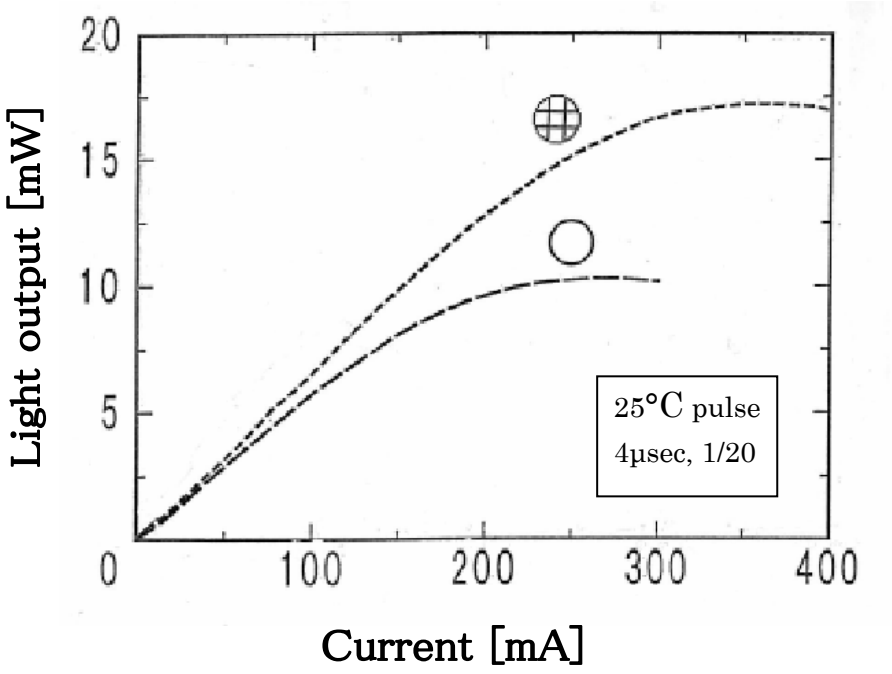

Fig. 1.15 Light-output characteristics of pin-point LED with and without mesh electrode.

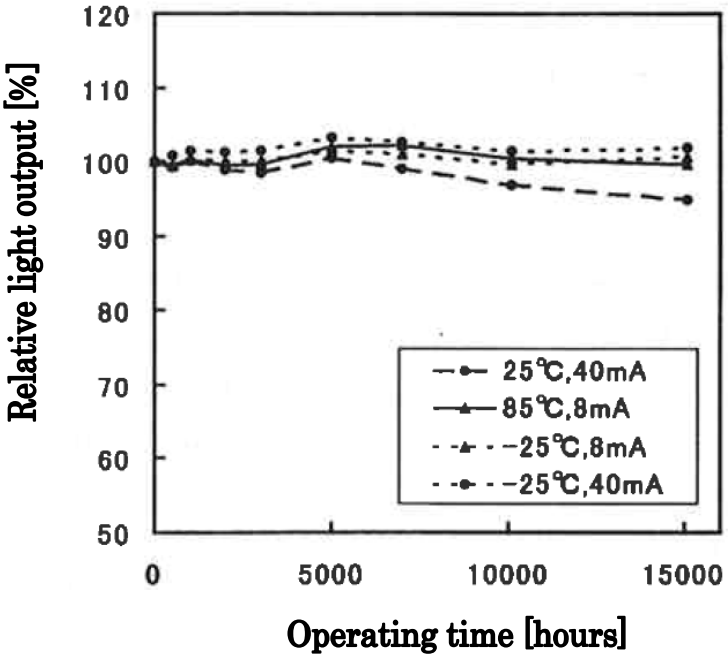

Fig. 1.16 Operating test results for AlGaInP pin-point LED molded in plastic package.

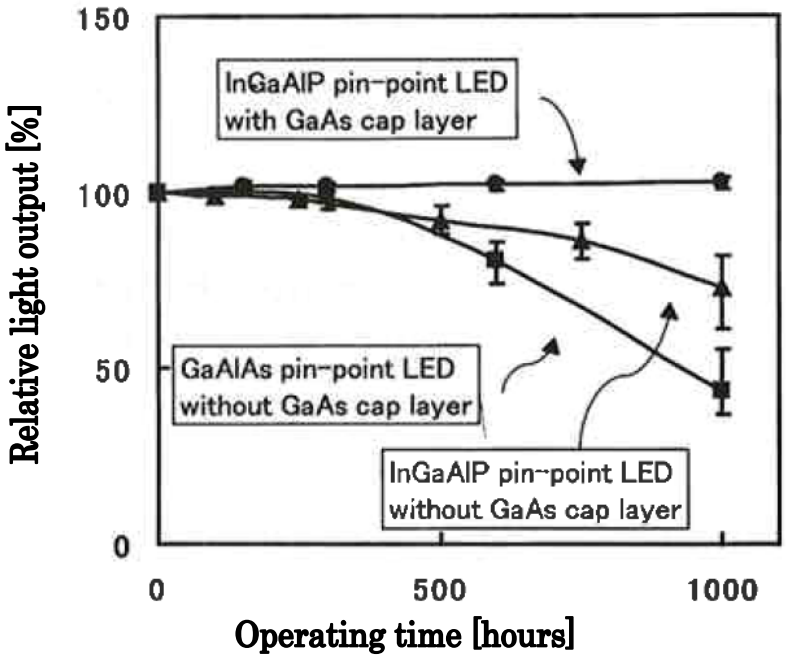

Fig. 1.17 Operating test results for AlGaInP pin-point LED and AlGaAs pin-point LED.

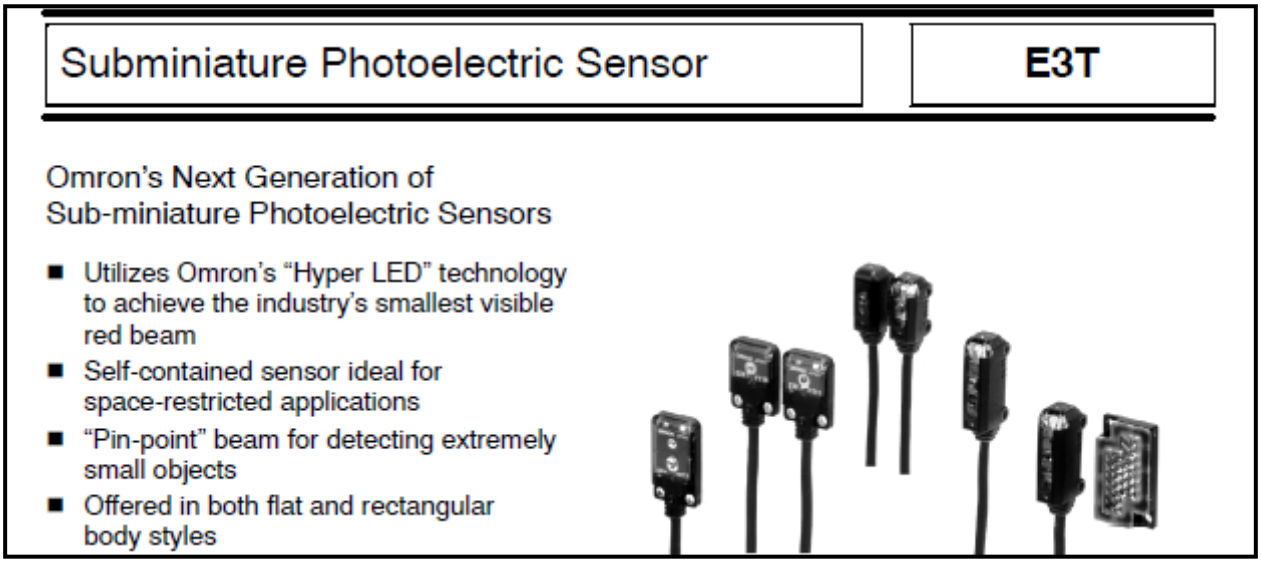

Fig. 1.18　Photoelectric Sensor (E3T) which has visible pin-point LED (Hyper LED).

1.4 Application to (111)-Substrate Expecting for Higher Performance

The use of quantum well hetero-structures on the (111)B oriented surface, instead of a conventional (100) surface, has been proposed by Hayakawa et al. [23], and they showed that the photoluminescence intensity from the (111)B oriented single quantum well (SQW) was several times higher than that from the highest quality (100) SQW. Further more, a lower threshold current density (J_{th}) of 145 A/cm^2 [24], than the (100) case, was demonstrated in a graded-index separate-confinement hetero structure (GRIN-SCH) laser diode fabricated on a (111)B oriented surface. These superior characteristics originated in the different quantization axis of QWs. In their crystal growth using molecular beam epitaxy (MBE), a rather high temperature (720°C) and a slightly mis-oriented (0.5° toward the (100) axis) surface were adopted. Otherwise, at lower growth temperature and on exact (111)B surface, AlGaAs-GaAs epitaxial layer exhibits an extremely rough surface due to the short diffusion length of AlGaAs and GaAs. Little has been reported on a reflection high-energy electron diffraction (RHEED) intensity oscillation, which is the most powerful in-situ monitoring method for the crystallinity of epitaxial layers in MBE on (111)B oriented GaAs substrate because of their rough surface [23, 25].

In order to overcome this problem, a migration enhanced epitaxy (MEE) method [26, 27] was applied, in which group III (Ga and/or Al) and group V (As) elements are deposited alternately on a substrate to improve surface morphology using the longer migration length of Ga (and/or Al) atoms than that in a conventional MBE, to the (111)B oriented GaAs surface. The RHEED intensity oscillation was observed at low temperatures between 500 and 700°C. A featureless AlGaAs specular surface has been grown on the (111)B oriented GaAs substrate without surface mis-orientation even at a very low temperature of 400°C.

First, two samples were prepared to show the ability of the MEE method using MBE system (ANELVA832) on an exactly (111)B oriented (degree of

mis-orientation ± 0.1°) GaAs substrate. One was grown at 580°C by conventional MBE; the other was grown by MEE at low temperature of 400°C. The epitaxial structure consists of a 1-μm thick $Al_{0.2}Ga_{0.8}As$ layer above a 0.2 μm thick GaAs buffer layer.

All the epitaxial layers were unintentionally doped. Each growth rate was unified to be 0.29 μm/h, which was precisely determined by the measurement of the oscillation period of the RHEED intensity on the (100) GaAs substrate in the run just prior to the epitaxial growth. The irradiation cycle of the MEE growth consists of 1 sec in which the As shutter is open (Ga closed).

The surface morphology of the epitaxial layer grown by conventional MBE consists of many small trigonal pyramids as shown in Fig. 1.19. This feature is unsuitable for optical waveguides including the QW hetero-structure. On the other hand, the epitaxial layer grown by MEE shows a featureless specular surface. Thus the MEE method is also confirmed to be powerful for the epitaxial growth on exactly (111)B oriented surface.

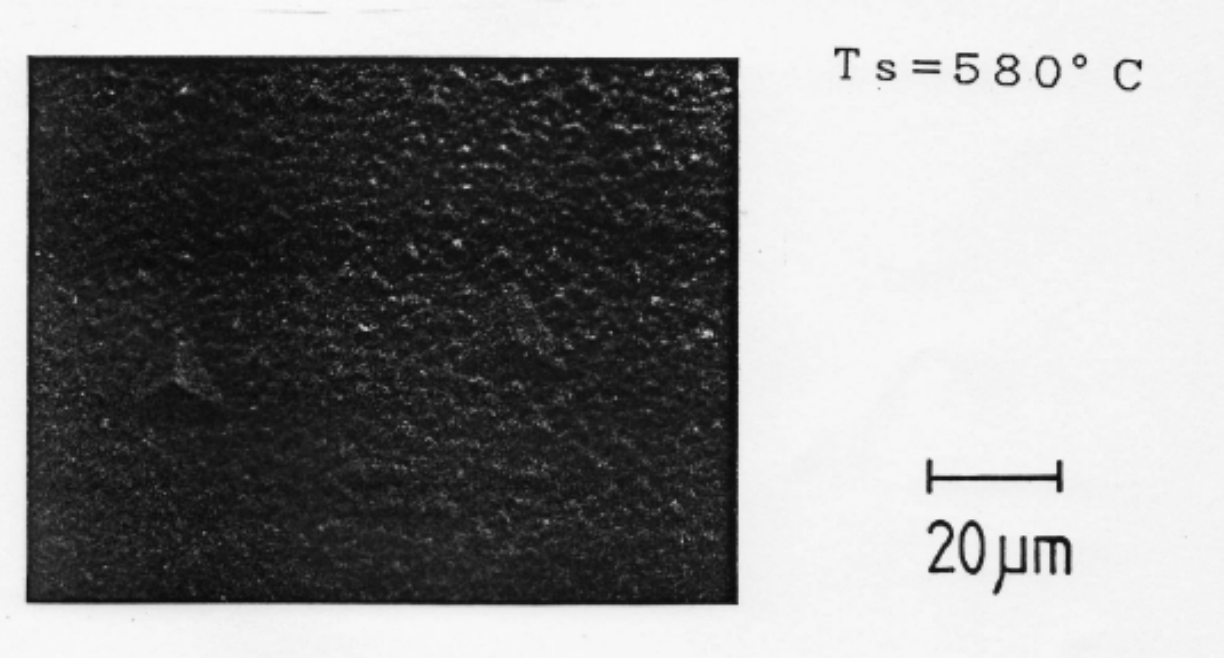

Fig. 1.19 Normarski interference contrast micrograph of $Al_{0.2}Ga_{0.8}As$ layers grown at 580°C on exactl (111)B substrate by conventional MBE.

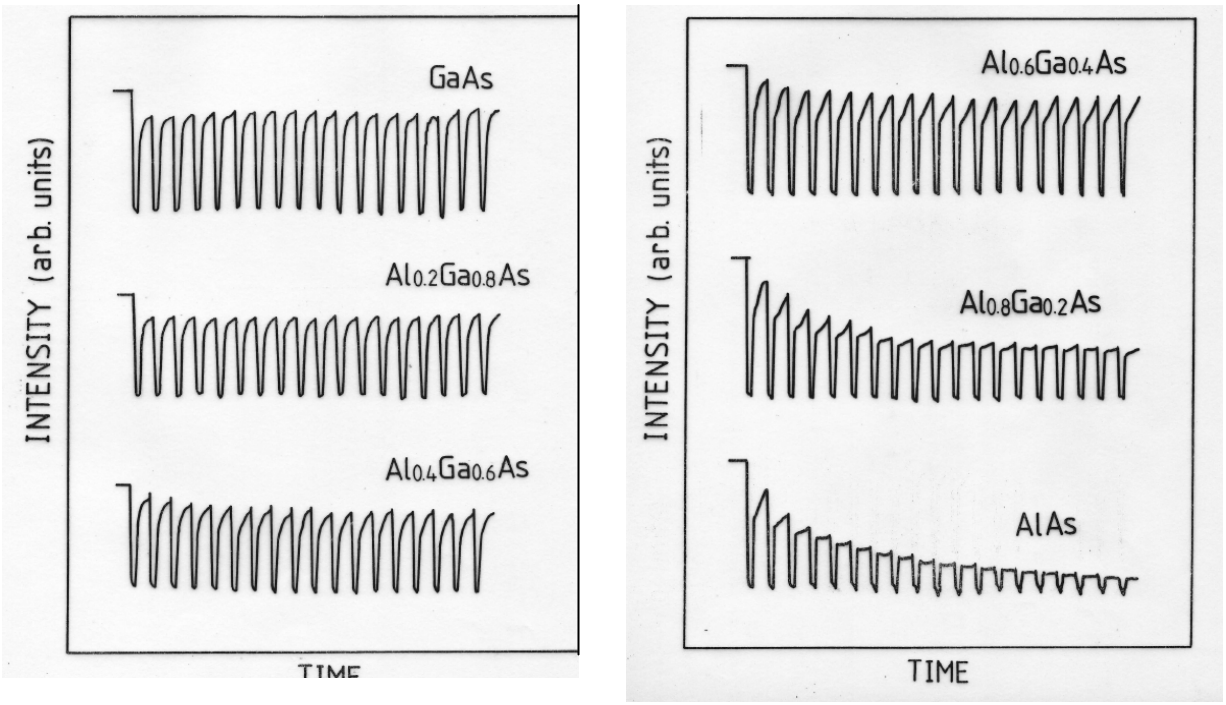

Fig. 1.20 RHEED intensity oscillation of various $Al_xGa_{1-x}As$ grown at 580°C monitored from <1$\bar{1}$0> azimuth.

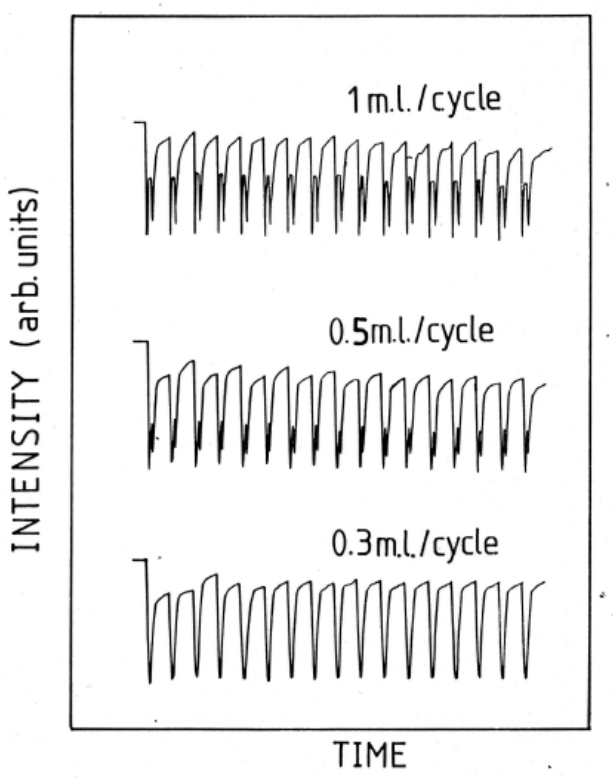

Fig. 1.21 RHEED intensity oscillation of various Ga irradiation from 0.3 to 1.0 monolayer per cycle monitored from <211> azimuth.

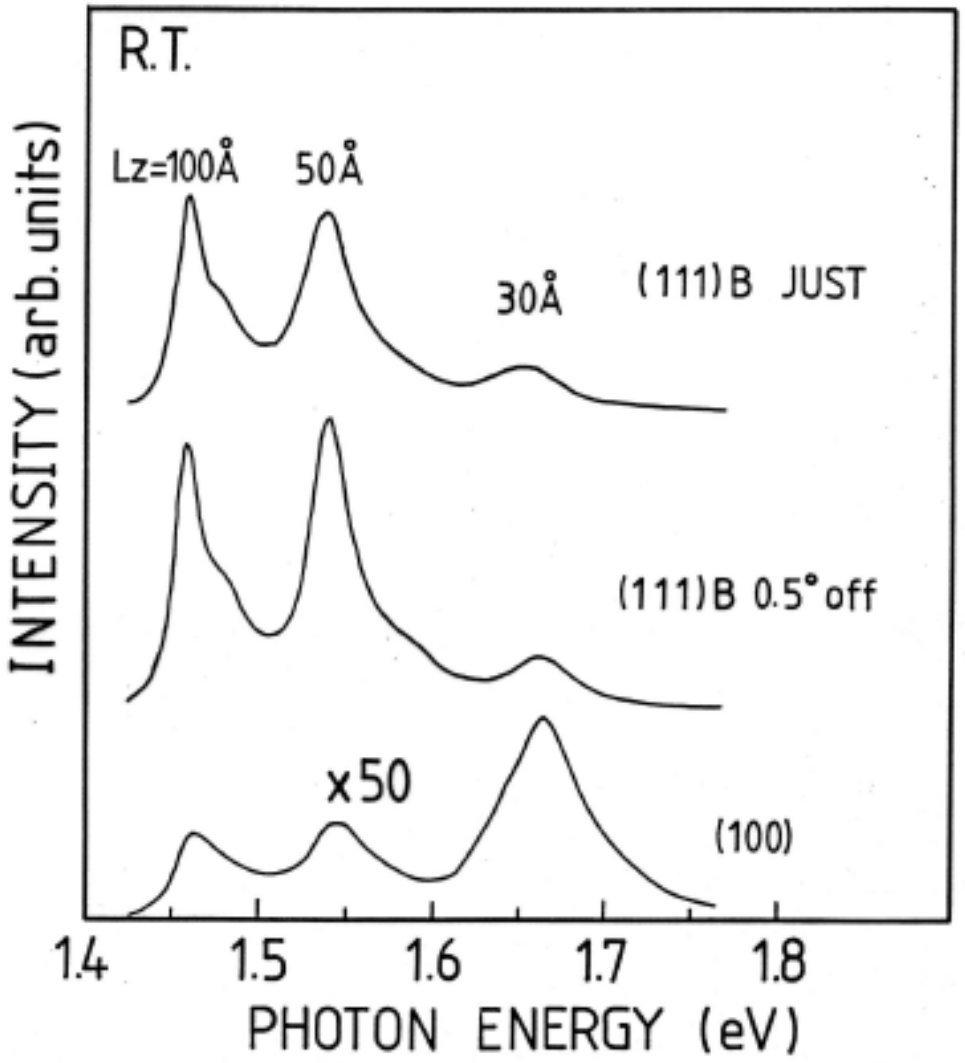

Fig. 1.22 Photoluminescence spectra of AlGaAs-GaAs SQWs grown on (100), exact (111)B and mis-oriented (111)B substrates.

A RHEED intensity oscillation was monitored from the (1$\bar{1}$0) and (211) azimuth using 30 keV high energy electron beam. MEE growth for GaAs was tested at various growth temperatures, and two-dimensional growth was confirmed, because of no damping of the oscillation amplitude of the RHEED specular beam, even after the lapse of 1000 periods, and surface reconstruction was clearly observed in the RHEED pattern during the MEE growth. The maximum amplitude of the oscillation, which is comparable to that of growth on the (100) surface, was obtained at 570°C growth.

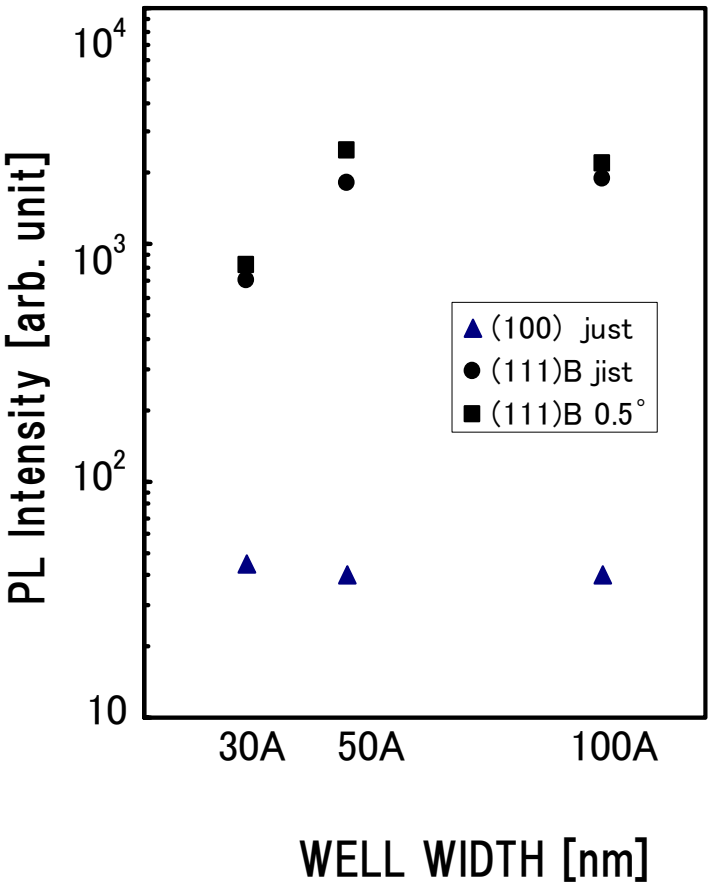

Fig. 1.23 Photoluminescence intensity of AlGaAs-GaAs SQWs grown on (100), exact (111)B and mis-oriented (111)B substrates.

Figure 1.20 shows the RHEED intensity oscillation of various AlGaAs grown at 570°C monitored from <1$\bar{1}$0> azimuth. As the Al mole fraction increases, the amplitude of the oscillation intensity decreases gradually. This could be explained that the surface migration length of Al atoms is shorter than that of Ga atoms.

Figure 1.21 shows the RHEED intensity oscillation of various Ga irradiations from 0.3 to 1.0 monolayers per cycle. The RHEED intensity oscillation is monitored from <211> azimuth. When the Ga irradiation was exactly 1.0 monolayer per cycle, the amplitude of the RHEED intensity did not change. However, when the Ga irradiation was 0.3 and 0.5 monolayers per cycle, the amplitude of the RHEED peak intensity changed at the beginning of epitaxial growth. And when the Ga supply corresponded to integer monolayer, the amplitude of the peak intensity was maximum. This effect is very similar to that by Horikoshi et al. [28] on (100) surface.

Figure 1.22 and Fig. 1.23 show the PL spectra and typical PL intensity of AlGaAs-GaAs SQWs on (100), exact (111)B, and 0.5° mis-oriented (111)B substrate grown simultaneously. Each layer contained three wells of 3.0, 5.0 and 10 nm thickness, respectively. The difference in the PL intensity was not observed from the SQW between the exact and mis-oriented (111)B GaAs surfaces. However, the PL intensities from the SQW on (111)B surface with and without mis-orientation were about 50 times higher than that of the (100). Thus it was confirmed that the MEE is powerful even on (111)B GaAs substrate, and the (111)B SQW is superior to the (100) ones.

In summary, migration enhanced epitaxy (MEE) has been successfully employed to grow AlGaAs. On an exactly (111) oriented GaAs substrate, featureless specular surface morphology is obtained at growth temperature between 570 and 400°C. Using the RHEED monitoring system, intensity oscillation was observed even on a (111)B oriented GaAs surface. The author has shown that PL intensities from the SQW on the (111)B surface with and without mis-orientation were about 50 times higher than that of the (100)

surface. The MEE method must be the most suitable technique to grow AlGaAs on a (111)B oriented substrate, because Ga and As are placed alternately on the substrate.

1.5 Conclusion

In this chapter, the author investigated improvement of light emitting device characteristics based on III-V compound semiconductors.

At first, AlGaAs/GaAs short period superlattice was applied to various part of AlGaAs quantum well laser diode. By using short period superlattice, upper side of the crystal quality has been improved. As the result, the improvement of the laser characteristics were confirmed which were high efficiency, low threshold current, and high light output power with high temperature stability. On the other hand, redeeming the demerit of laser diode such as eye safety, life time and so on, the author suggested a new pin-point LED and successfully put it into commercial production as shown in Fig. 1.18.

Finally, the author investigated using the other crystal axis instead of (100) and confirmed that (111) oriented substrate has new possibility to improve the light output characteristics. Also the MEE method was confirmed as the most suitable technique to grow AlGaAs on (111)B oriented substrate.

References

[1] W.T.Tsang and R.L.Hamittman, Appl. Phys. Lett. **38**, 502 (1981).

[2] H.Z.Chen, A. Ghaflari, H.Morokoc and A.yariv, Electron. Lett. **23**, 1334 (1987).

[3] P.M.Petroff, R.C.Miller, A.C.Gosard and W.Wiegmann, Appl. Phys. Lett. **44,** 217 (1984).

[4] O.Wada, T.Sanada, M.Kuno, and T.Fujii, Electron. Lett. **21**, 1025 (1985).

[5] W.T.Maselink, M.V.Klein, Y.L.Sun, Y.C.Chang, R.Fischer, T.I.Drummound and H.Morokoc, Appl. Phys. Lett. **44**, 435 (1984).

[6] T.Fujii, S.Hiyamizu, S.Yamakoshi and T.Ishikawa, J. Vac. Sci. Technol. B **3**, 776 (1985).

[7] H.Shimizu, K.Ito, M.Wada, T.Sugino and I.Teramoto, IEEE J.Quantum. Electron. vol.**QE-17**, 763 (1981).

[8] T.Hayakawa, N.Miyauchi, S.Yamamoto, H.Hayashi, S.Yano, and T.Hijikata, Appl. Phys. Lett. **42**, 23 (1983).

[9] S.Sasaki, T.Soga, M.Takeyasu and M.Umeno, Appl. Phys. Lett. **48**, 413 (1986).

[10] M.Razzeghi, F.Omnes, M.Defour and PH. Maurel, Appl. Phys. Lett., **52**, 209 (1988).

[11] T.G.Amderson, Z.G.Chen, V.D.Kulalovski, A.Uddaim and J.T.Vallin, Appl. Phys. Lett. 51, 752 (1988)

[12] F.Sato, H.Imamoto, M.Asai, T.Inoue, K.Imanaka and M.Shimura, J. Appl. Phys. **63**, 964 (1988).

[13] T.Hayakawa, T.Suyama, K.Takahashi, M.Kondo, S.Yamamoto and T.Hijikata, Appl. Phys. Lett. **49**, 636 (1986).

[14] O.Wada, T.Sanada, N.Nobuhara, M.Kuno, M.Maliuchi and T.Fujii, Instit. Phys. Conf. Ser. **79**, 685 (1986).

[15] W.T.Tsang, in Semiconductor and Semimetals, edited by R.Dingle (Academic, San Diego, 1987), Vol.**24**, Chap.7.

[16] T.Hayakawa, T.Suyama, K.Takahashi, M.Kondo, S.Yamamoto and T.Hijikata, Appl. Phys. Lett. **52**, 339 (1988).

[17] B.A.Joyce, P.J.Dobson, J.H.Neave and J.Zhang, in proceedings of 2nd International Conference Kyoto **1**, (1985).

[18] F.Sato, H.Imamoto, M.Asai, K.Imanaka and M.Shimura, J. Appl. Phys. **63** 964 (1988).

[19] S.D.Hersee, B.de Cremoux and J.P.Dochemin, Appl. Phys. Lett. **44**, 476 (1984).

[20] B.Garret, I.H.White and D.F.G.Gallagher, Electron. Lett. **23**, 371 (1987).

[21] W.T.Tsang, Appl. Phys. Lett. **39**, 786 (1981).

[22] R.M.Fletcher, C.P.Kuo, T.D.Osentowski, K.H.Huang, M.G.Craford and V.M.Robbins, J. Electron. Material. **20**, 1125 (1991).

[23] T.Hayakawa, M.Kondo, T.Suyama, K.Takahashi, S.Yamamoto and T.Hijikata, Jpn. J. Appl. Phys. **26**, 302 (1987).

[24] T.Hayakawa, T.Suyama, K.Takahashi, M.Kondo, S.Yamamoto and T.Hijikata, Appl. Phys. Lett. **52**, 339 (1988).

[25] T.Fukunaga, T.Takamori and H.Nakashima, J. Crust. Growth **81**, 85 (1987).

[26] Y.Horikoshi, M.Kawashima and H.Yamaguchi, Jpn. J. Appl. Phys. **64**, 432 (1988).

[27] M.Asai, F.Sato, H.Imamoto, K.Imanaka and M.Shimura, J. Appl. Phys. **6**4, 432 (1988).

[28] Y.Horikoshi, M.Kawashima and H.Yamaguchi, Jpn. J. Appl. Phys. **27**, 169 (1988).

Chapter 2

Fabrication of Ultraviolet Sensors with Nano-Structured ZnO

2.1 Introduction

The sensing capability of light wave ranging from visual to infrared, realized by using AlGaAs and AlGaInP, was discussed in Chapter 2. Nanostructures of zinc oxide (ZnO), which is a wide band-gap (3.37 eV) semiconductor, have become attractive recently in order to take advantage of its unique optical properties with large binding energy (60 meV) [1] of free excitons. For example, lasing action in ZnO nanowire arrays at room temperature was recently reported [2]. Research on low-dimensional nano-structures such as nanowires, nanorods, and nanosheets have received increasing attentions also due to their potential use as active components or interconnects in fabricating nanoscale electronic, optical, optoelectronic, electrochemical, and electromechanical devices.

Due to these properties, ZnO has been focused in consideration of its adequateness for application in short wavelength like UV light emitting and detecting devices. Ultra violet photodetectors with ZnO have been studied. Zinc oxide growth is extendedly investigated and discussed in this chapter through various processes such as vapor liquid phase.

2.2 Formation of ZnO Nano-dots for UV sensors Grown by Metal Organic Chemical Vapor Deposition

The nanostructures of ZnO have been well known to dynamically vary depending on the growth conditions [3-6]. The quasi one dimensional structures among various nanostructures have particularly received considerable attentions as a component of low dimensional devices in nano-scale science and technology [2, 7-9]. For example, the formation of ZnO nanodot arrays using focused ion beam (FIB) nanopatterning was reported in the past few years [10]. Another promising technique to fabricate quasi-one-dimensional structures is to use atomic steps on a substrate surface as nucleation sites of the nanostructures. Dot formation of IV or III-V semiconductor along the step edges on semiconductor substrates has been well known in high vacuum or ultra high vacuum (UHV) using molecular beam epitaxy (MBE) or metalorganic molecular beam epitaxy (MOMBE) [11-13]. High vacuum is necessary for arraying these semiconductor nanostructures because the surface of the substrates are easily oxidized and/or contaminated with the residual gases in the atmosphere. On the other hand, sapphire surface is very stable against the oxidation and therefore it may be an ideal template for arraying the nanostructures along their step edges even in near atmospheric pressure in a metalorganic chemical vapor deposition (MOCVD) system, which matches with actual device fabrication without UHV.

2.2.1 Fabrication of Arrayed ZnO Dots along Steps

Sapphire with $(11\bar{2}0)$, (0001) and $(10\bar{1}2)$ planes (A-plane, C-plane and R-plane, respectively) were employed as substrates for alignment of nanostructures. They were firstly cleaned by ultrasonic washing with acetone and isopropanol. To prepare optimized templates with the single step arrays, the substrates were annealed at 900-1150°C for 1-24 hours in air after the chemical treatment. The ZnO nanodots were prepared by MOCVD. Diethylzinc (DEZn) and nitrous oxide (N_2O) were employed as zinc and oxygen sources, respectively. Highly pure N_2 was used as a carrier gas, which carries sources onto substrate. The flow rate of DEZn was varied from 1-2 × 10^{-6} mol/min and that of N_2O in the range of 7-28 × 10^{-3} mol/min.

Annealing techniques and conditions of linear single step arrays at regulated intervals have been established for the surface of a C-plane sapphire [14, 15]. However, they have not been fully clear for A-plane and R-plane sapphire yet. Then in order to enhance dry and wet processes of pretreatment with sapphire substrates, the optimum annealing conditions for different surfaces were investigated by changing the annealing temperature and time, they were identified as, for example, 1,000°C and 3 hours, respectively.

Figure 2.1 (a)-(c) show the atomic force microscope (AFM) images of the sapphire substrate surfaces of A-plane, C-plane and R-plane, respectively, subjected to the annealing on the above conditions after the chemical treatments. Each arrow of thick line in the images indicates the step down direction. From the images it is seen that on C-plane and R-plane sapphire's stepped surfaces can easily be prepared only through the simple treatment.

In contrast, it was difficult to align the straight step with more than a micrometer long on A-plane sapphire; there were a lot of kinks of several ten nanometers long, which were wider than the average terraces width on the surface. The separate experiments have shown that the energy for forming linear steps along the $[\bar{1}100]$ and [1000] directions is very high; the steps tend to be formed along these directions without forming a number of kinks. This

means that on A-plane the relatively long steps of several ten nanometers along [$\bar{1}$100] direction are formed without many kinks but are suddenly interpreted when the internal energy of avoiding formation of kinks, which is accumulated during the formation of steps along [$\bar{1}$100] direction meeting miss-cut of the substrate surface, cannot stand for any more, resulting in extending to [1000] direction with large kinks and large zigzag structures. On the other hand, on C- or R-planes the step formation process is so often interpreted by the miss-cut and this results in small kinks, that is, in atomic scale the step edges are actually formed by zigzag structure of short steps and small kinks but in larger scale the steps are seen to be extended for more than micrometers; while on A-plane the relatively long steps of several ten nanometers are formed without many kinks but are suddenly interpreted when the internal energy of avoiding formation of kinks cannot stand for any more, resulting in large kinks and large zigzag structures. The longer annealing time, for example, 6-12 hours at 1,000ºC, resulted in multi-step and wider terrace structure, and for 24 hours giant steps and wide terraced structure were formed. These surface structures on A-plane sapphire such as irregular step arrays and giant step-terraces are not also suitable for the formation of nanodot arrays in this study.

Therefore it is concluded that the C-plane and R-plane sapphire obtained by a simple way, that is, the annealing in air for 3 hours at 1,000ºC, can be used as optimized templates for the arraying of ZnO nanodots. Further, it should be noted that the similarly stepped surfaces were observed by AFM even after several weeks, indicating that the sapphire templates are very stable against surface reaction and degradation in air and are very easy to be handled in air as a template, different from the semiconductor templates.

2.2.2 Characterization of Nano-Structured ZnO

Then in order to investigate the initial nucleation processes on different substrate surface, the ZnO growth was made at 600ºC for 10 seconds. Here the dots were formed not only on the terraces but also on the step edges. On A-plane notable difference of the dot density on the terraces and on the step edged was hardly observed. However on R-plane and C-plane, 55 % and 72 % of dots were aligned on the step edges respectively. In the growth of ZnO, it is assumed that several nuclei diffuse on the terraces. Within the diffusion length on the terraces they form dots, or if step edges exist within the diffusion lengths they nucleate on the step edges and form the dot array. The above results suggest that the diffusion length on R-plane is larger than on other planes. This implies that the R-plane is better for the dot arrangement along the step edges. The exact reason is not known why the diffusion length on R-plane is larger, but a preliminary consideration can be given by the comparison of the dangling bond density on each plane. The dangling bond densities assuming no surface reconstruction were calculated as 34 nm^{-2}, 31 nm^{-2} and 25 nm^{-2} on A-plane, C-plane and R-plane respectively, showing the lowest density on the R-plane. Because of this reason, the diffusion length on R-plane is the largest and therefore the sticking probability on step edges should be higher than that on other planes. The detailed discussions on the formation mechanism of nanodots will be given in other publications.

From the above results, therefore, it is expected that R-plane sapphire can be a good template for the linear dot arrays of semiconductor on an insulator substrate. According to this knowledge, formation of ZnO nanodot arrays was examined on the templates. In order to enhance the diffusion length more, the growth was made at a higher substrate temperature of 700ºC. After the growth for 10 seconds, well aligned ZnO nanodots were formed along the step edges of R-plane sapphire, compared to A-plane and C-plane.

Fig. 2.1 shows the AFM images of the surface. It is clearly seen that ZnO nanodots are arranged linearly at about the same interval along steps. The

figure indicated that the dot arrays only 5 micrometers long, but the length of the dot arrays was actually more than several ten micrometers. This fact shows that nanostructures of II-VI compound semiconductor on an insulator can be formed even under near atmospheric pressure by MOCVD.

Finally the crystallinity of the dots was investigated using a conventional x-ray diffraction (XRD) measurement. Unfortunately the dots shown in Fig. 2.2 were too small for the measurement, so the investigation was made for the larger islands or films evolved from the nanodots. Figure 2.3 shows the XRD pattern of the sample formed by the growth of 30 minutes on R-plane sapphire, where single peak of ZnO $(11\bar{2}0)$ diffraction was observed. From this result it is reasonable to assume that the nanodots along the step edges are crystalline with A-plane perpendicular to the R-plane of sapphire.

The well aligned ZnO nanodot arrays have been formed along the step edges of R-plane sapphire over more than several ten micrometers. This is supported by the properties of R-plane sapphire, that is, formation of step structures with simple thermal annealing process, stability of the step structure in air, and large diffusion length of the nuclei on the surface. The fact implies that sapphire can be a good template for manufacturing the semiconductor nanostructures on it, and as the result II-IV semiconductor nanostructures can be manipulated on an insulator even at near atmospheric pressure by a conventional MOCVD.

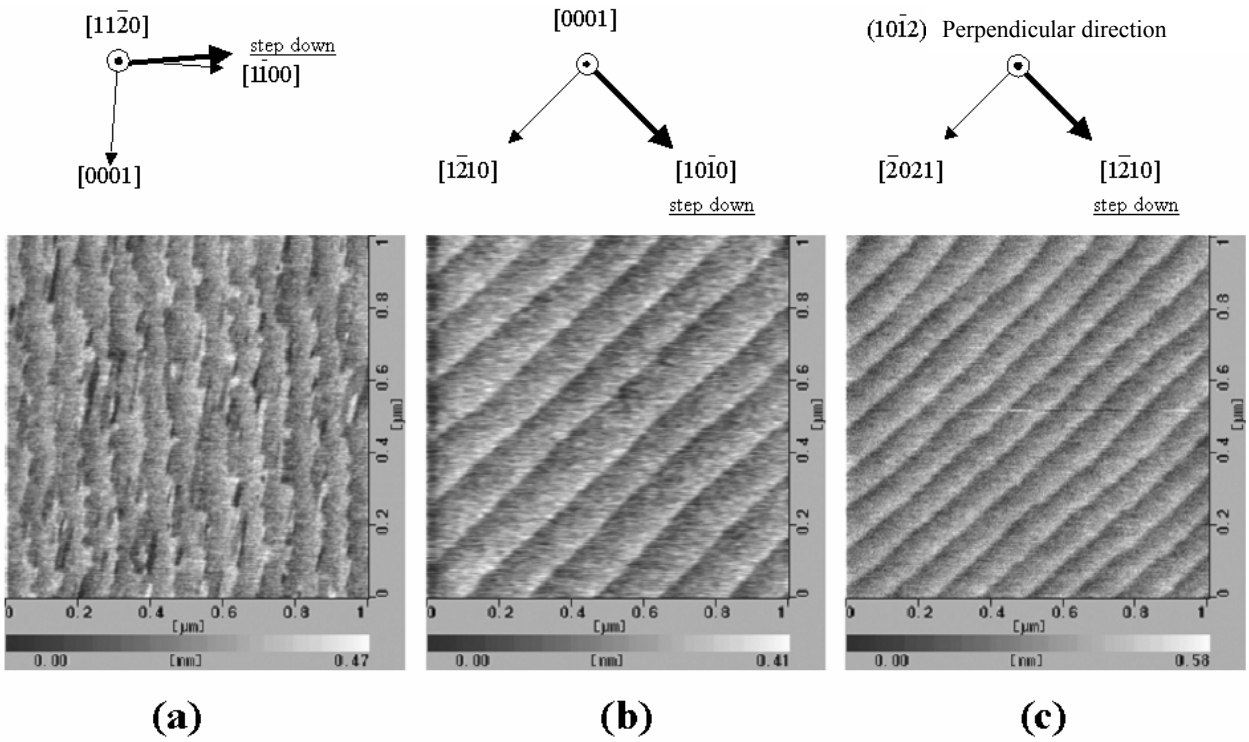

Fig. 2.1 AFM images of the surface on each plane of sapphire substrate annealed by 1000°C for 3 hours: (a) A-plane, (b) C-plane and (c) R-plane. Arrows of thick line in the images indicate each step's down direction.

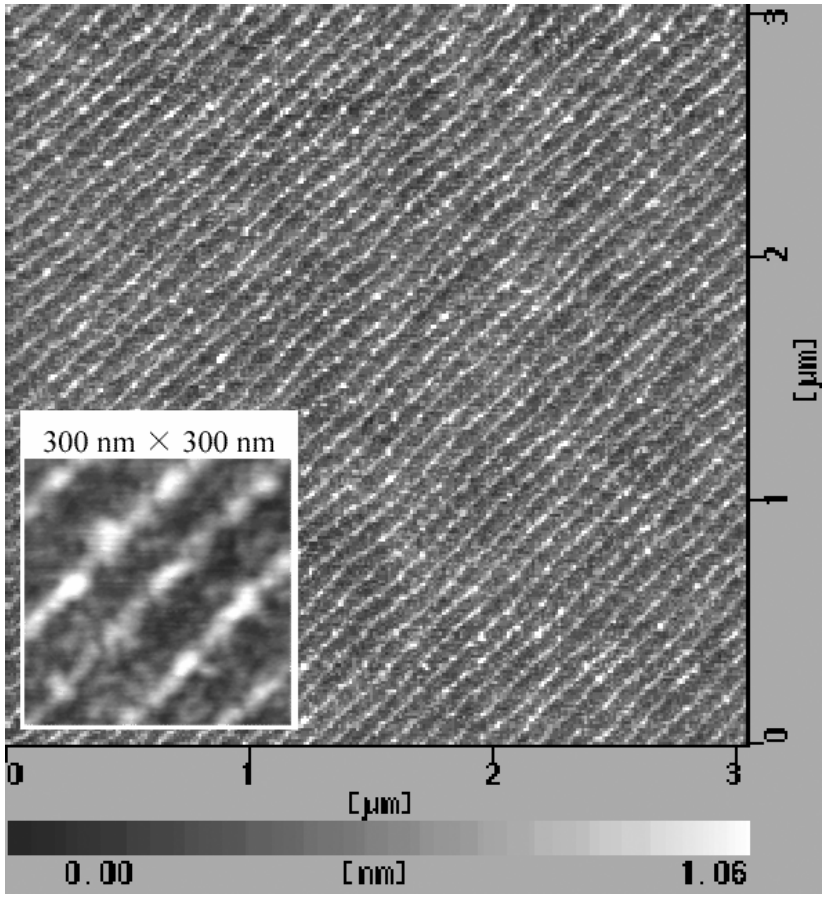

Fig. 2.2　AFM images of dot alignment along steps on sapphire substrates. The condition of the formation was at 700°C for 10 seconds by MOCVD: (a) the large area image and (b) enlarged image of the surface.

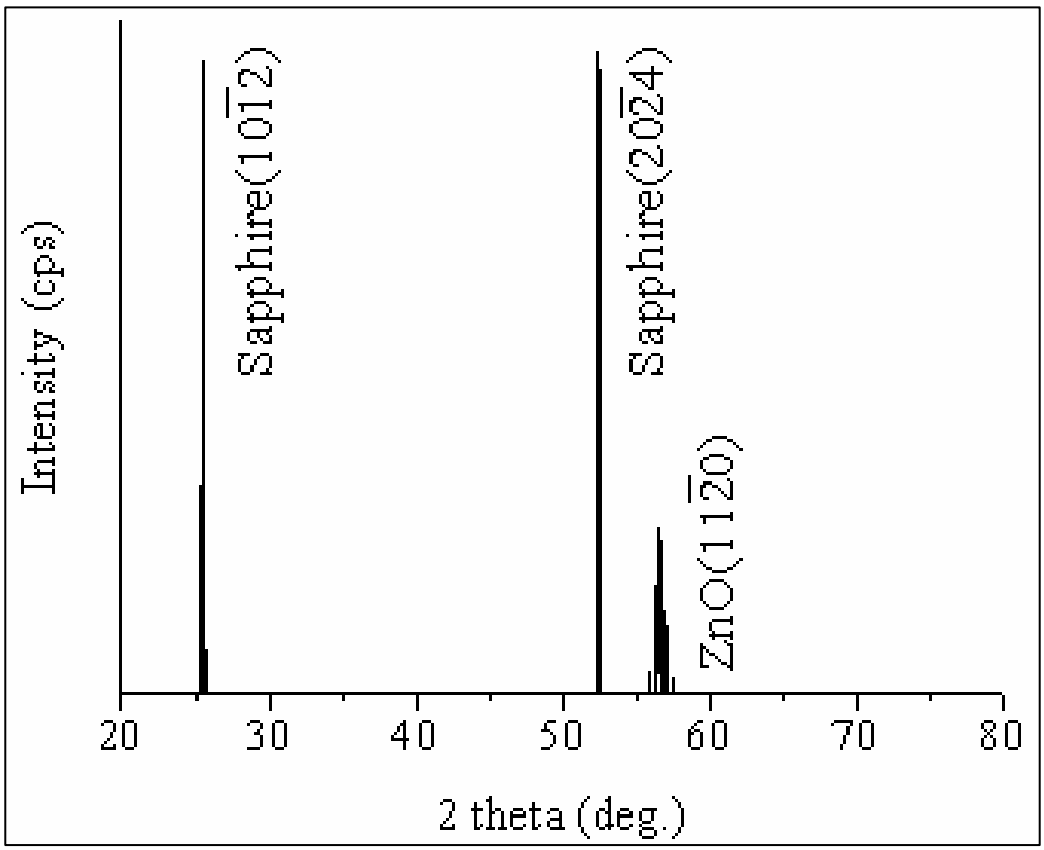

Fig. 2.3 XRD pattern of the sample treated at 600°C for 30 minutes on R-plane sapphire.

2.3 ZnO Whiskers between Micron-gap Electrodes in Aqueous Solution Process

2.3.1 Particles of ZnO through Solution Process

Among functional ceramics, ZnO is of great interest for photonic applications due to its wide band gap (3.37 eV) and large excitons binding energy (60 meV). Therefore it has wide applications in the fields of lasers, solar cells and optoelectronic devices. It is well known that ZnO crystal is one of polar crystals whose positive polar plane is rich in Zn and the negative polar plane is rich in O. The information has made it more crucial for designing and manufacturing more sophisticated devices. It has been reported that ZnO nanostructures can be prepared by various methods including anodic alumina template, vapor–liquid–solid (VLS) mechanism growth, metal-organic vapor-phase epitaxial growth (MOVPE) and sol-gel technique. Sol–gel process is a method that has a possibility to easily realize single crystal growth, doping and alloying in the period of the preparation of functional films. There is aqueous solution process method among sol-gel methods realized by using various organic solvents. However this method requires only water in the process of the film growth. Therefore the method has been employed in this study for its safe and easy handling characteristics.

For the growth of ZnO nanorods on SiO_2 glass substrates, a two-step sol–gel process was used in this study. The sols were prepared by dissolving zinc nitrate hexahydrate ($Zn(NO_3)_2 \cdot 6H_2O$) and hexamethylenetetramine ($C_6H_{12}N_4$, HMT or methenamine) as basic ingredient in deionized water and stirred for several minutes at room temperature until a white suspension was formed. During the heating process up to 90°C, HMT causes the increase of Zn^{2+} and OH^- in the solution and then $Zn(OH)_2$ is finally formed. So the heterogeneous precipitation of $Zn(OH)_2$ on substrate, which requires lower ionic product than the homogeneous precipitation, can be effectively prevented in the

initial stage of the thermolysis process. The overall growth of ZnO can be written according to the following reaction.

$$Zn^{2+} + 2OH^- \rightarrow Zn(OH)_2 \rightarrow ZnO + H_2O \quad \cdots\cdots\cdots\cdots (1)$$

The initial concentration of ($Zn(NO_3)_2 \cdot 6H_2O$) in the liquid was started at 0.1 M. Lower concentrations, down to 6.25×10^{-3} mol/L, were obtained by successive dilution of the initial solution with deionized water. Different molar ratio experiments of Zn^{2+}/methenamine, including 1:1, 1:2 and 1:5, were carried out while the other conditions were kept unchanged. The solution was kept in a flask bottle with SiO_2 glass substrate in an oven for 1-6h thermal treatment at 90°C. After the reaction had been completed, the resulted deposit products on glass were washed with deionized water to remove the residual of salts and organic substances remaining in the final products.

X - ray diffraction (XRD) $\theta/2\theta$ patterns of the ZnO deposit are shown in Fig. 2.4. Most of XRD spectra exhibits dominant peak at $2\theta = 31.7°$ corresponding to the hexagonal wurtzite structure of ZnO (100) plane (JCPDS No. 36-1451). From this XRD pattern and the former SEM images, it is indicated that these single crystal ZnO were grown along [0001] direction. No peaks at $2\theta = 34.36°$ (0002), or 36.18° ($10\bar{1}1$) could be observed as it is often reported. The influence of ($Zn(NO_3)_2 \cdot 6H_2O$) initial concentration on the structure of the ZnO is very strong as no X-ray diffraction peak could be observed for the highest concentration, i.e. 0.1 M. It was apparent that all the ZnO films consisted of a single ZnO phase oriented with its *c*-axis parallel to the substrate surface, no diffraction from randomly oriented grains or impurity phases could be observed from the X-ray patterns.

The morphology of the ZnO was observed by Scanning Electron Microscopy. A close observation on the surface coverage and the microstructure of the ZnO nanorods for two initial concentrations of 0.05 M and 6.25×10^{-3} mol/L (1h reaction time at 90°C) are shown in Fig. 2.5 (a)- (b). Both the size and the shape

of ZnO are affected by the zinc ion concentration. Aggregated hexagonal structures with a rather flat shape were obtained at the highest concentration (a) while morphology shows ZnO to nucleate almost completely parallel to the substrate and tends to be rod-like as nanorods shaped structure with 1-2 mm length and 0.05-0.1 mm in diameter for the lowest concentrations (b). The surface coverage presented by the nanorods is estimated at < 5 % for a single deposit.

Figure 2.6 shows the room temperature fluorescence spectra of the ZnO obtained at different concentrations for the excitation wavelength of 340 nm. It can be seen that all samples show a strong single violet emission centering around 370-380 nm without any accompanying deep level. It is also seen (not shown) that the violet emission peak position shifted slightly depending on the excitation wavelength.

The transmittance spectra for the as-grown ZnO nanostructures are shown in Fig. 2.7 for several concentrations. Almost all exhibit a transmittance of 50 % in the 400-1200 nm range. Transmission, however, changes very sharply at 350 nm due to the absorption edge of ZnO at room temperature. A correlation between structural, morphological and optical properties of zinc oxide nanostructures deposited on a glass substrate by the sol-gel process has been observed through several analyses. It is shown that the initial Zn^{+} concentration has strong effects even after the nucleation of ZnO. Further studies on the growth behavior, like the effect of surfactants, doping, alloying with Mg, and the use of those nanostructures for future nano-based devices, have been an ongoing development.

2.3.2 Fabrication of UV Sensors with ZnO

In this study the author formed whiskers between electrodes in the aqueous solution by only one step and investigated electrical properties of the whiskers.

The interdigital structured electrodes (Au/Cr) with 10 micron gap were fabricated by conventional photolithography. ZnO nanorods on glass substrates between 10 μm gap electrodes were synthesized in aqueous solution. The solutions consist of zinc nitrate hexahydrate ($Zn(NO_3)_2 \cdot 6H_2O$) and hexamethylenetetramine ($(CH_2)_6N_4$, HMT) in deionized water. The solution was then heated in an oven at 90°C for 1-12 hours. The initial concentration of zinc nitrate and HMT ($mol_{Zn}/mol_{HMT} = 1$) was at 0.1 mol/L or less. The process resulted in the increase of Zn^{2+} and OH^- in the solution and then $Zn(OH)_2$ is produced. The homogeneous reaction and heterogeneous reaction of $Zn(OH)_2$ occurred above and on the substrate respectively. The formation of ZnO can be represented according to the following reactions.

$$(CH_2)_6N_4 + 6H_2O \rightarrow 6HCHO + 4NH_3 \quad \cdots\cdots\cdots\cdots (2)$$

$$NH_3 + H_2O \Leftrightarrow NH_4^+ + OH^- \quad \cdots\cdots\cdots\cdots (3)$$

$$2OH^- + Zn^{2+} \rightarrow Zn(OH)_2 \rightarrow ZnO + H_2O \quad \cdots\cdots\cdots\cdots (4)$$

After the reaction, the resulting products on the substrate were washed by ultrasonic cleaning for 10 minutes to remove residuals on the substrate.

X-ray diffraction (XRD) patterns and scanning electron microscope images showed that the main products were wurtzite ZnO nanorods like hexagonal column whose sides were composed of (1000) faces. After cleaning, among nanorods hence formed, only those directly grown on electrodes remain. The conditions of nanorods formation and substrates cleaning have been carefully chosen so that nanorods bridge the gap between two electrodes. The resistance of one nanorods bridging between the electrodes was estimated to be several kΩ in the atmosphere.

There are numbers of works for bridging ZnO whiskers between electrodes. The following technique has generally been developed for this purpose; (1) collect the functional material which was produced beforehand, (2) disperse it in the volatile solvent, (3) drip the liquid droplet on the electrodes, (4) a bridge between the electrodes is achieved accidentally. But, it is difficult to crave highly-reproducible with the characterization of the structure because the structure obtained by this technique cannot be stabilized from the viewpoint of mechanical strength.

In this report in order to fabricate a bridge firmly connecting two electrodes, ZnO growth was directly conducted on the electrodes in the aqueous solution. The aqueous solution with zinc nitrate hexahydrate and hexamethylenetetramine were heated at 90°C for 0.5-9 hours. After the synthesizing, the sample was washed with deionized water, and then the whiskers grown through homogeneous nucleation were removed. Moreover, the samples were applied with ultrasonic agitation to remove the whiskers weakly attached on the electrodes. As the result only the whiskers sticking firmly onto electrodes were left selectively. In this process, ZnO whiskers bridging between micron-gap electrodes were successfully fabricated. The electric resistance of the structure is several mega-ohms in a room, while it is irradiated by the UV light of 390-nm wavelength with applied voltage of 5 V, high photoconductivity with more than 20 μA is confirmed. The response characteristics for other external stimuli have also been confirmed.

It is one of the next-generation technologies to securely bridge a functional material between two electrodes with a narrow gap. The important features with respect to this structure are high current density and low power consumption. Especially, with the low dimensional structure of materials, a bigger ratio of the surface to the volume, in other words, an increase in the specific surface area is remarkable. Therefore, increased response characteristics for external stimuli can be developed, and a highly sensitive sensor which operates at low electric power consumption can be expected as one

of the applications. As the material to bridges two electrodes, the functional materials such as carbon nanotubes, whiskers of the semiconductor, and so on have been reported. Among those materials, ZnO has been extremely expected for optical and electronic devices as well as sensors supported by its wide band gap (3.37 eV), the large binding energy of excitons (60 meV), the chemical activity of surfaces, together with the strong tendency of forming whiskers.

A bridge was fabricated which firmly connects two electrodes, and the growth of ZnO formed between the electrodes was directly took place on the electrodes in the aqueous solution. In this process, ZnO whiskers bridging between micron-gap electrodes were successfully fabricated. The value of electric resistance of the structure was several mega-ohms in a room in the atmosphere. The values of electric resistance vary often because of the sensibility to gases in the air so that in use for photo devices the active area must be encapsulated in the future. Furthermore, when it is irradiated by the UV light of 390-nm wavelength with applied voltage of 5 V, high photoconductivity with more than 20 μA was confirmed. The response characteristics for other external stimuli have also been confirmed.

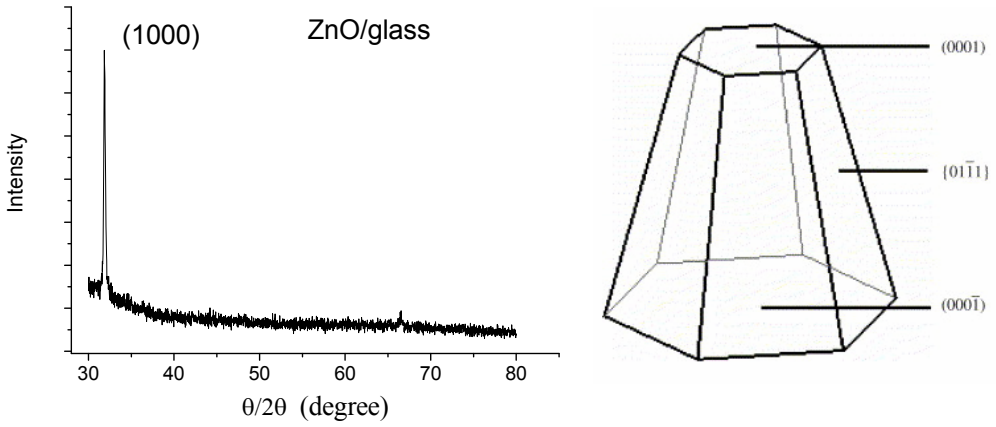

Fig. 2.4 X-ray diffraction pattern and indexing lattice plane for hexagonal ZnO.

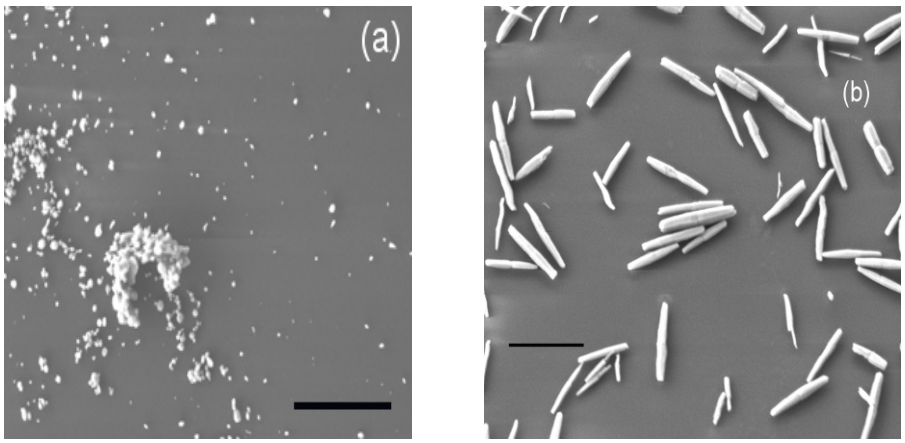

Fig. 2.5(a)-(b) SEM image of ZnO nanostructure at (a) 0.05 M and (b) 6.25×10^{-3} mol/L concentration. Markers represent 2 μm.

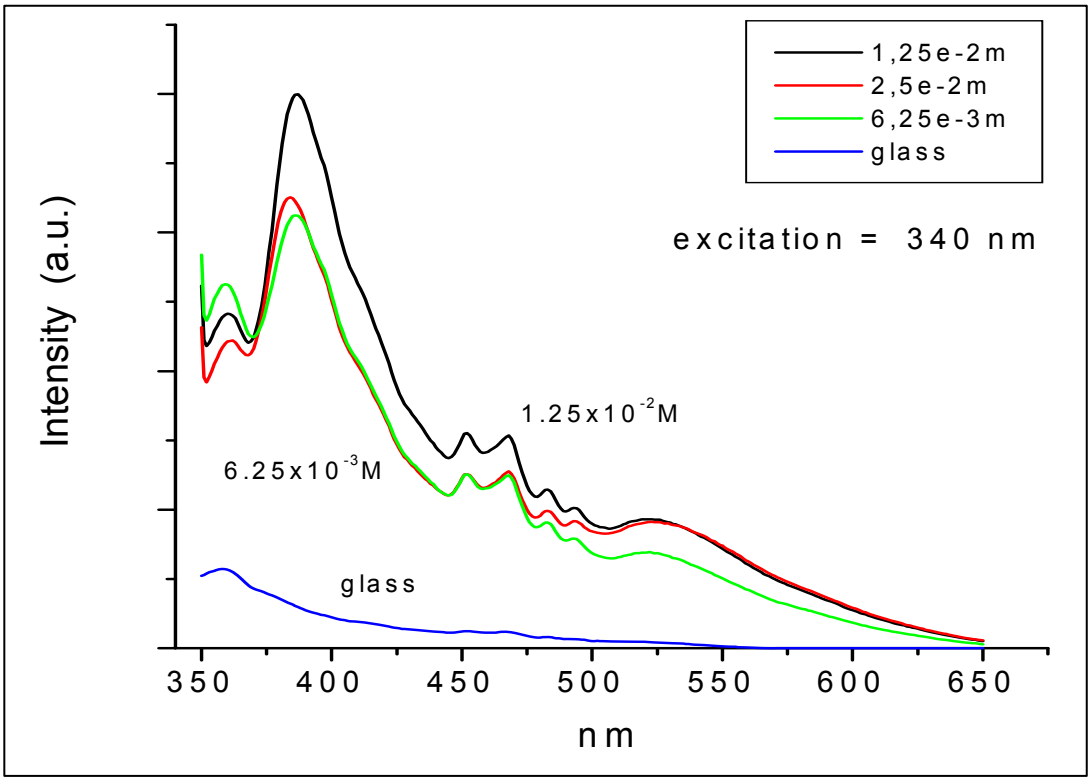

Fig. 2.6 Fluorescence spectra.

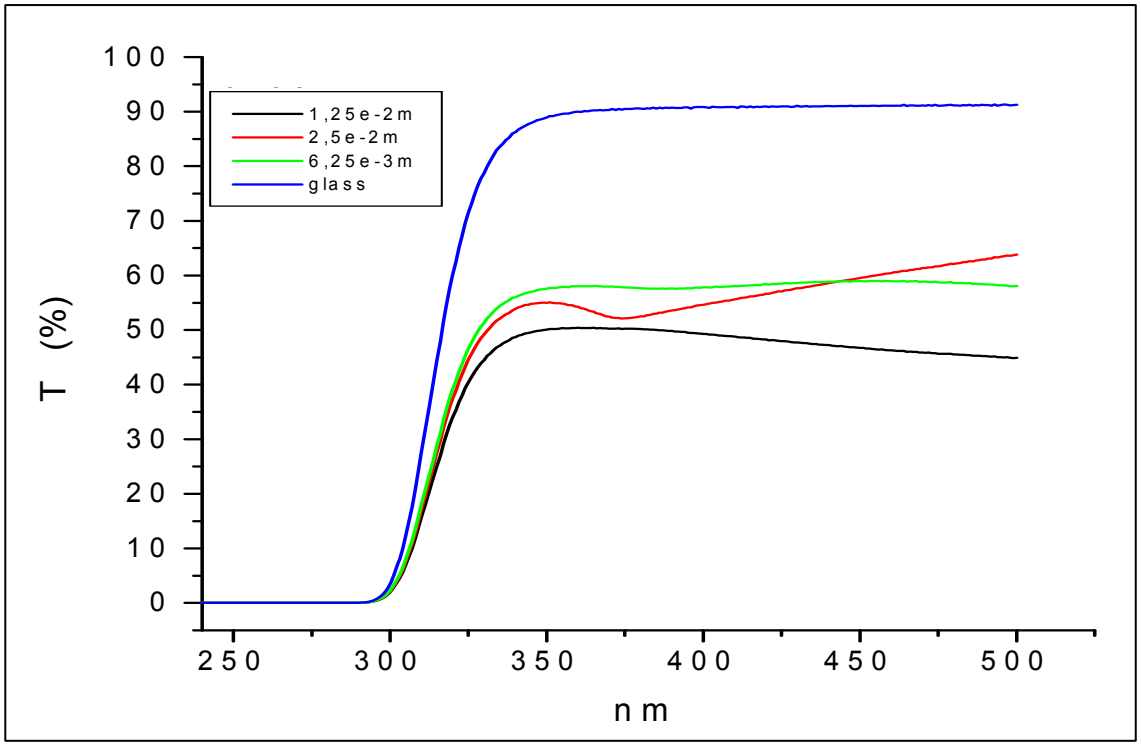

Fig. 2.7 UV transmittance of ZnO nanostructures.

2.3.3 Another Sensing Characteristics by ZnO Whiskers

Zinc oxide (ZnO) has been conventionally used in the field of gas sensors such as H_2 and CO [16, 17]. Highly sensitive gas sensors have been increasingly expected for safety as monitoring devices of living environment and chemical processes. In recent years, there also have been many reports about the fabrication and characteristics of ZnO gas sensors composed of nanostructures as a sensing area owing to their high surface-to-volume ratio [18, 19]. However, it is actually difficult to control the nanostructures of the sensing component and placing them at the desired positions [20, 21].

An approach was investigated to artificially fabricate a ZnO structure gas sensor bridging two micron-gap electrodes by using electrolytic deposition. The above photo devices are responsive to air due to their particular structure. In other words the ZnO with the structure has high potential for gas sensors. Electrolytic deposition, which does not require high temperature heating, complex systems, or toxic sources, is a simple and cost-effective method to fabricate ZnO [22-24]. The application of this technique to highly-functional materials is highly advantageous to mass application of highly-functional devices at low cost.

In this chapter, the author reports the selective electrolytic deposition of ZnO micro-structures selectively bridging micro-gap electrodes by applying electric field between the electrodes in aqueous solution of zinc ions. The H_2 gas sensing characteristics of the device hence fabricated significantly encourage this technique for future nano-scale devices with downsizing the electrode configuration as well as providing low cost gas sensors.

Micron-gap electrodes (Au/Cr), used both for the sensor device and the plating electrodes, were formed by a conventional photolithography. The optical microscope photograph of the electrodes, together with their dimensions, is shown in Fig. 2.8.

Schematic drawing of the electrolytic deposition system is shown in Fig. 2.9. Our objective is to fabricate ZnO bridging the electrodes under electric field

without any lithographic technique. The source materials in the solution for Zn was zinc nitrate ($Zn(NO_3)_2$ $6H_2O$) or zinc acetate ($Zn(CH_3COO)_2$ $2H_2O$). No critical difference in the deposition characteristics was found for the both source materials, and therefore only the number of zinc ions is crucial for the formation of the devices. The source materials were diluted in pure water to the concentration of 0.001-0.1 mol/L. The AC bias voltage was applied between the two electrodes. The voltage and frequency have been widely varied to optimize the deposition conditions, and as a result they were determined as 10 V and 30-100 kHz respectively. In order to discuss the effect of these parameters, the deposition time was fixed at 10 min in the present experiments.

The composition of the electrolytic deposits was analyzed by energy dispersive X-ray spectroscopy (EDX) equipped in a scanning electron microscope (SEM). Gas sensing characteristics were investigated by the exposure to diluted hydrogen (H_2) gas.

In the wide range of the deposition conditions successful bridging was achieved between the electrodes with electrolytic deposits, which were found to be almost stoichiometric ZnO (shown later). Figure 2.10 demonstrates the optical microscope images of the bridged structure as a function of the frequency of the applied voltage. Here the source material is $Zn(CH_3COO)_2$ and the concentration of the aqueous solution is 0.01 mol/L. The higher frequencies did not result in deposition, probably because the drift velocity of Zn^{2+} ions in water was not able to respond completely to the frequencies. On the other hand, heavy deposition occurred at the lower frequencies, and this may be attributed to the deposition of ZnO with metal zinc rather than stoichiometric ZnO.

Figure 2.11 shows the optical microscope images of the deposits as a function of the $Zn(NO_3)_2$ source concentration in water. Here the frequency of applied voltage was 30 kHz. More deposits were formed between the electrodes with higher concentration. Figure 2.12 summarizes the deposited area, measured from the microscope images, against the source concentration. The deposited area monotonically increases with the concentration.

The SEM image of the deposits is shown in Fig. 2.13, that is, the sample deposited at the $Zn(CH_3COO)_2$ source concentration of 0.01 mol/L and the applied voltage frequency of 30 kHz. The deposited area was found to be 90 μm^2 with the height of 7-8 μm. The EDX spectrum of the deposits is shown in Fig. 2.14, together with that of a standard ZnO thin film. Comparing the intensity ratio between Zn and O, it may be concluded that almost stoichiometric ZnO has been directly and selectively fabricated connecting the micron-gap electrodes.

The formation of ZnO in the aqueous solution is assumed to be

$$H_2O \rightarrow H^+ + OH^-,\ 2H^+ + 2e^- \rightarrow H_2, \quad \cdots\cdots\cdots\cdots (5)$$

$$2Zn^{2+} + 2OH^- \rightarrow 2ZnO + H_2. \quad \cdots\cdots\cdots\cdots (6)$$

However, the formation of metallic Zn is simultaneously expected due to the reaction

$$Zn^{2+} + 2e^- \rightarrow Zn. \quad \cdots\cdots\cdots\cdots (7)$$

In Fig. 2.10, the low frequency (1 kHz) of applied voltage resulted in heavy deposition compared to the higher frequencies (30 and 100 kHz). This can be speculated to be the deposition of metal Zn and/or Zn-rich ZnO, according to eq.(12). At lower frequencies, it is plausible that the drift of Zn^{2+} ions effectively follows the applied electric field and Zn^{2+} ions are effectively transferred to the electrodes. This can enhance the reaction of eq.(7), resulting in deposition of metallic ZnO_n, on the other hand at higher frequencies the drift of Zn^{2+} ions to the electrodes is gradually limited and therefore eq.(5) rather than eq.(7) can become dominant, successfully forming ZnO rather than metallic Zn. Of course, when the frequency is too high the drift of Zn^{2+} ions is completely suppressed and this does not allow the bridging of the electrodes with ZnO.

Gas sensing characteristics were investigated by exposing the device to a 500-ppm H_2 gas for 15 min at room temperature. The resistivity before exposure, R_{air} = 91.7 MΩ, was changed after exposure to R_{gas} = 70.4 MΩ, where the sensitivity of $|R_{gas} - R_{air}| / R_{air}$ = 0.23 was obtained. It is noteworthy that the gas sensing was done at room temperature.

However, the present device still has a large dimension than what have been intended, which is against the high sensitivity and low power consumption. The present device can easily be fabricated by conventional photolithography. However, an important issue is that the device can be scaled down to nanometer dimensions by using the sub-micron-gap electrodes and by optimizing the electrolytic deposition conditions. The present results encourage development of highly-functionalized nanometer-sized devices with the simple technique and low cost.

In summary, the author proposed the simple but convenient method to fabricate ZnO selectively and artificially between two micron-gap electrodes using the electrolytic deposition in aqueous solution of $Zn(NO_3)_2$ or $Zn(CH_3COO)_2$. The electrodes used for electrolytic deposition can be readily diverted to the contact electrodes for sensing devices. The device showed the 500 ppm H_2 gas sensing capability without external heating. The fabrication method possesses the advantages of technological simplicity and it can facilitate low-cost gas sensors to mass applications.

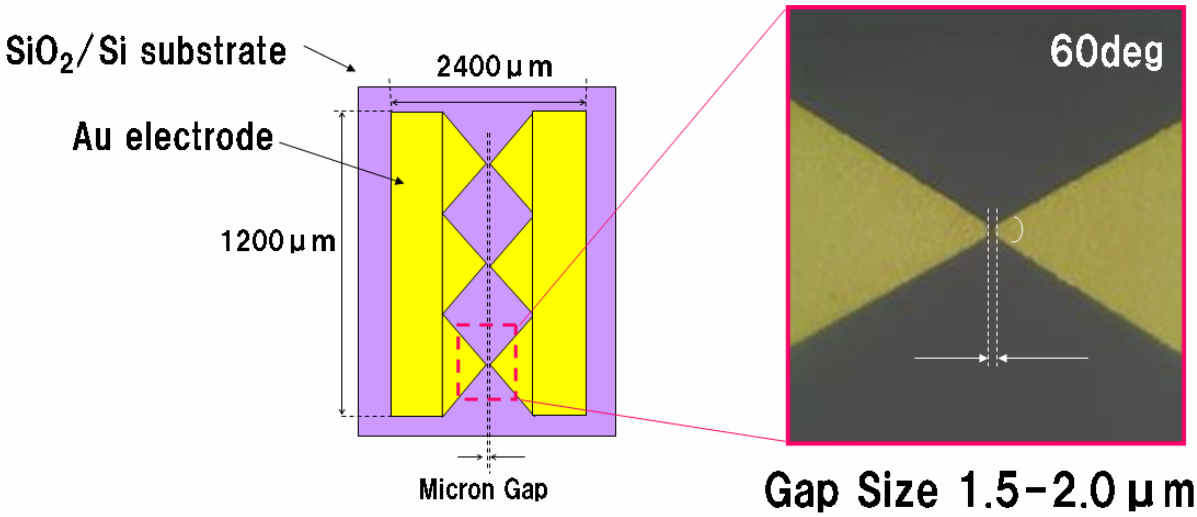

Fig. 2.8 Schematic drawing and photograph of micron-gap electrodes.

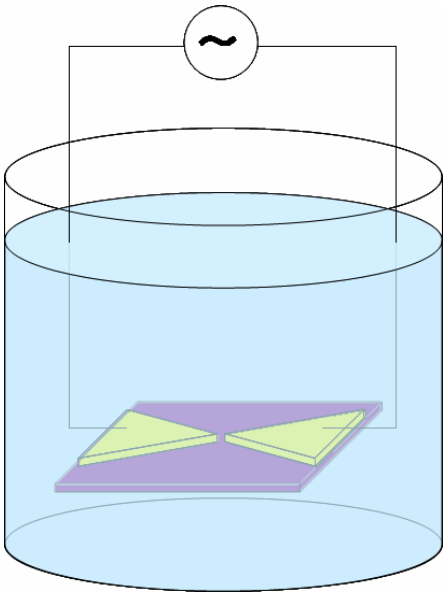

Fig. 2.9 Schematic drawing of the electrolytic deposition system.

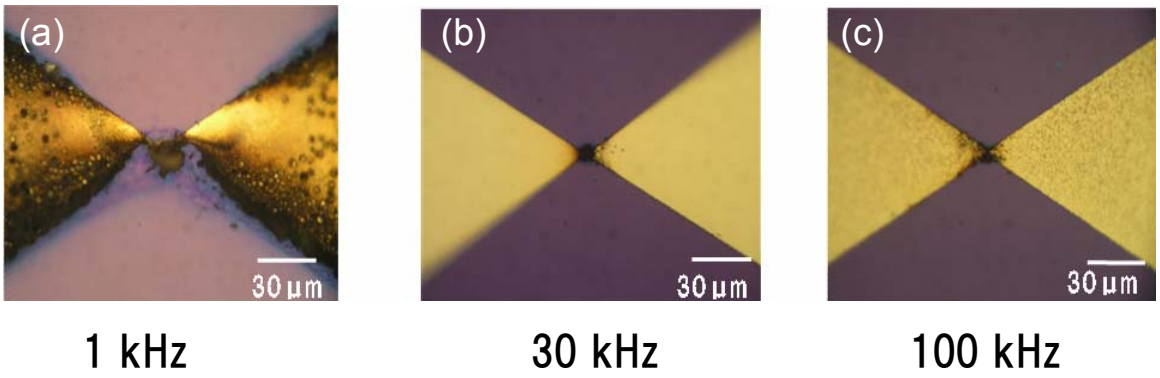

Fig. 2.10 Optical microscope images of the electrolytic deposits as a function of the frequency of applied voltage. The source material is $Zn(CH_3COO)_2$ and the concentration of the aqueous solution is 0.01 mol/L.

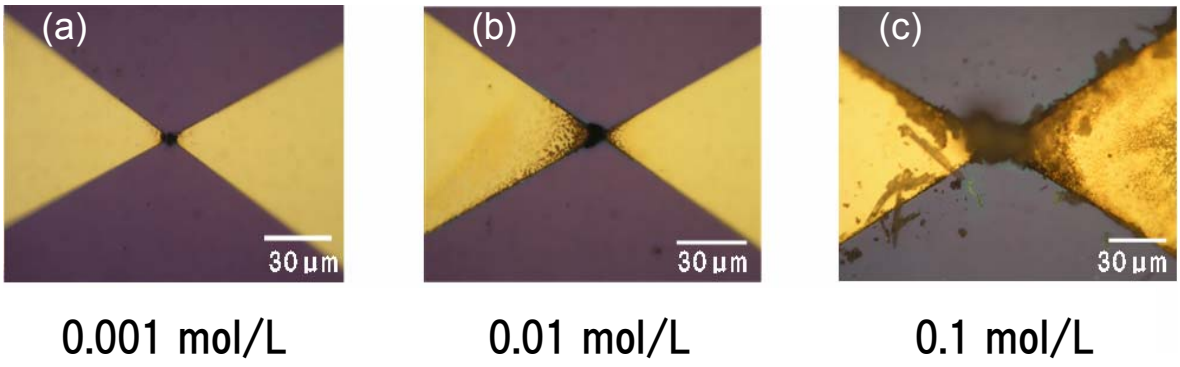

Fig. 2.11 Optical microscope images of the electrolytic deposits as a function of the concentration of source material. The applied voltage frequency is 30 kHz and the source material is $Zn(NO_3)_2$.

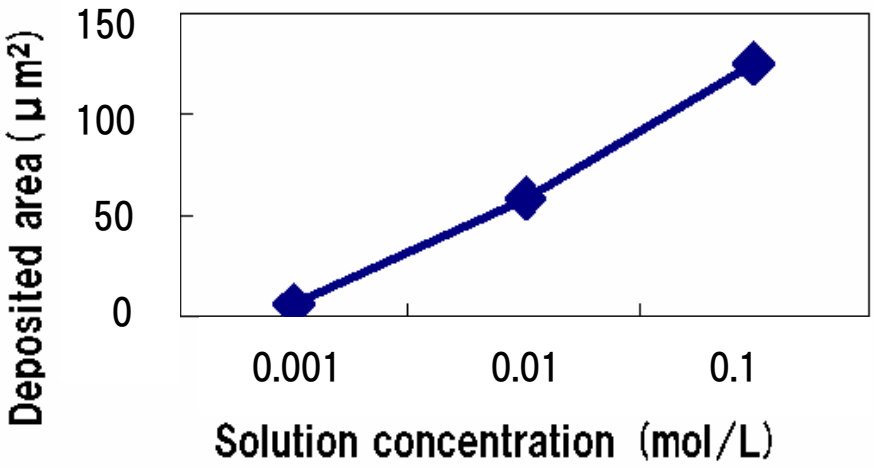

Fig. 2.12 Relationship between the source concentration and the bridged area with the deposits.

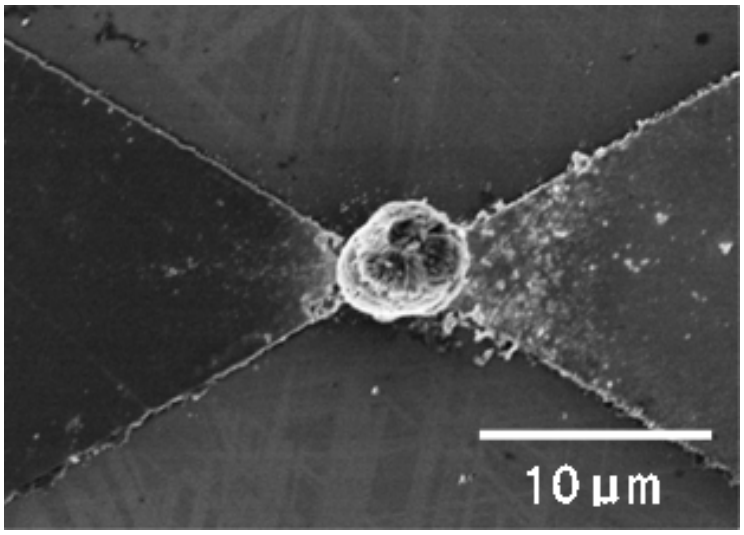

Fig. 2.13 The enlarged SEM image of the deposits shown in Fig 2.10(b), where the $Zn(CH_3COO)_2$ source concentration was 0.01 mol/L and the applied voltage frequency was 30 kHz.

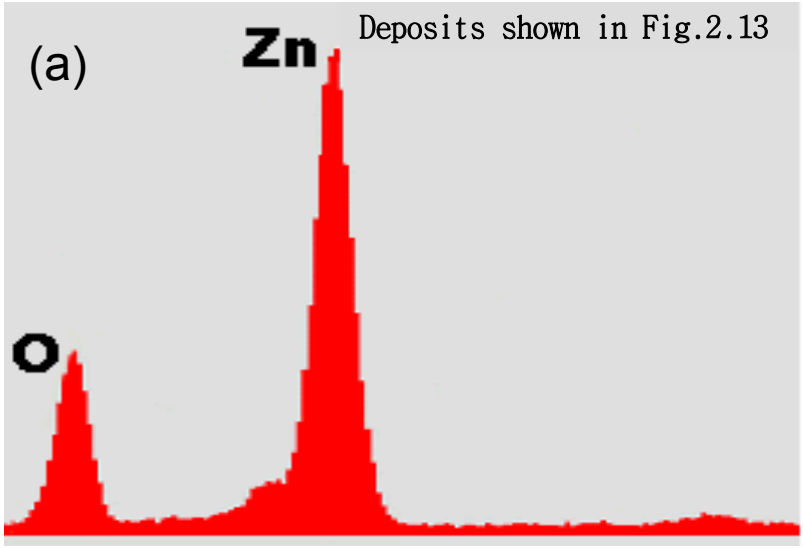

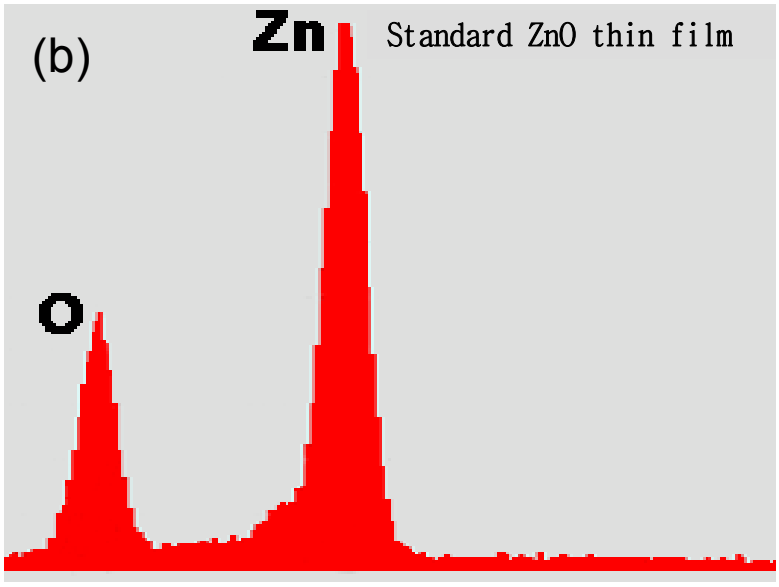

Fig. 2.14 EDX spectra of the deposit shown in Fig. 2.13 in comparison with that of a standard ZnO thin film.

2.4 Conclusion

The high vacuum is necessary for arraying these semiconductor nanostructures because the substrates are easily oxidized and/or contaminated with the residual gases in the atmosphere. On the other hand, sapphire surface is very stable against the oxidation and therefore it may be an ideal template for arraying the nanostructures along the step edges even in near atmospheric pressure in a metal organic chemical vapor deposition (MOCVD) system, which can be matched for actual device fabrication without UHV.

The author fabricated a bridge firmly connecting two electrodes. The growth was directly conducted on the electrodes in the aqueous solution. The aqueous solution with zinc nitrate hexahydrate and hexamethylenetetramine were heated at 90°C for 0.5-9 hours. After the synthesizing, the samples were rinsed and the whiskers which grew through homogeneous nucleation were removed. Moreover, the samples were applied by ultrasonic agitation to remove the whisker weakly attached on the electrodes. As the result only the whiskers sticking firmly onto electrodes were left selectively. In this process, ZnO whiskers bridging between micron-gap electrodes were successfully fabricated. The value of electric resistance of the structure was several mega ohm in a room, while when it is irradiated by the light of 390-nm wavelength with applied voltage of 5 V, high photoconductivity with more than 20 μA was confirmed. The response characteristics for other external stimuli have also been confirmed.

Moreover, the author proposed the simple but convenient method for the fabrication of ZnO selectively and artificially between two micron-gap electrodes using the electrolytic deposition in aqueous solution of $Zn(NO_3)_2$ or $Zn(CH_3COO)_2$. The electrodes used for electrolytic deposition can be rapidly diverted to the contact electrodes for a sensing device. The device shows 500ppm H_2 gas sensing capability without external heating. Both the fabrication method and the device structure possess the advantages of

technological simplicity and they can facilitate the low-cost gas sensors contributing to mass applications.

References

[1] P.Zu, Z.K.Tang, G.K.L.Wong, M.Kawasaki, A.Ohtomo, H.Koinuma and Y.Segawa, Solid State Commun. **103**, 459 (1997).

[2] M.H.Huang, S.Mao, H.Feick, H.Yan, Y.Wu, H.Kind, E.Weber, R.Russo and P.Yang, Science **292**,1897(2001).

[3] K.Ogata, K.Maejima, Sz.Fujita and Sg.Fujita, J. Crystal Growth **248** ,25 (2003).

[4] Z.W.Pan, Z.R.Dai and Z.L.Wang, Science **291**, 1947 (2001).

[5] K.Maejima, M.Ueda, Sz.Fujita and Sg.Fujita, Jpn. J. Appl. Phys. **42**, 2600 (2003) .

[6] H. Yoshikawa and S. Adachi, Jpn. J. Appl. Phys. **36**, 6237 (1997).

[7] M.Law, D.J.Sirbuly, J.C.Johnson, J.Goldberger, R.J.Saykally and P.Yang, Science **305**, 1269 (2004).

[8] J.C.Johnson, H.Yan, R.D.Schaller, L.H.Haber, R.J.Sayakally and P. Yang, J. Phys. Chem. B **105**, 11387 (2001).

[9] M.C.Jeong, B.Y.Oh, W.Lee and J.M.Myoung, Appl. Phys. Lett. **86**, 103105 (2005).

[10] S.W.Kim, T.Kotani, M.Ueda, Sz.Fujita and Sg.Fujita, Appl. Phys. Lett. **83**, 3593 (2003).

[11] C.Teichert, J.C.Bean and M.G.Lagally, Appl. Phys. Lett. **67,** 675 (1998).

[12] D.Leonard, S.Fafard, K.Pond, Y.H.Zhang, J.L.Merz and P.M.Petroff, J. Vac. Sci. Technol. B **12**, 2516 (1994).

[13] J.Stangl, T.Roch, V.Holy, M.Pinczolits, G.Springholz, G.Bauer, I.Kegel, T.H.Metzger, J.Zhu, K.Brunner, G.Abstreiter and D.Smilgies, J. Vac. Sci. Technol. B **18**, 2187 (2000).

[14] M. Yoshimoto, T. Maeda, T. Ohnishi, H. Koinuma, O. Ishiyama, M. Shinohara, M. Kubo, R. Miura and A. Miyamoto, Appl. Phys. Lett. **67**, 2615 (1995).

[15] O. Kurnosikov, L. Pham Van and J. Cousty, Surface Science **459**, 256 (2000).

[16] S. Roy and S. Basu, Mater. Sci. **25**, 513 (2002).

[17] T. Yamazaki, S. Wada, T. Noma and T. Suzuki, Sens. Actuators B **13**, 594 (1993).

[18] H.T. Wang, B.S. Kang, F. Ren, L.C. Tien, P.W. Sadik, D.P. Norton, S.J. Pearton and J. Lin, App. Phys. A **81**, 1117 (2005).

[19] Q.H. Li, Y.X. Liang, Q. Wan and T.H. Wang, Appl. Phys. Lett. **85**, 6389 (2004).

[20] H. Kind, H. Yan. B. Messer, M. Law and P. Yang, Adv. Mater. **14**, 158 (2002).

[21] M.S. Arnold, Ph. Avouris, Z.W. Pan and Z.L. Wang, J. Phys. Chem. B **107**, 659 (2003).

[22] L.Vayssiers, Adv. Mater. **15**, 464 (2003).

[23] Q.Li, V.Kumar, Y.Li, H.Zhang, T.J.Marks and R.P.H. Chang, Chem. Mater. **17**, 1001 (2005).

[24] M. Yoshimura, W.L. Suchanek and K. Byrappa, MRS Bulletin **25**, 17 (2000).

Chapter 3

Anti-Reflection Structure Fabricated by Femtosecond Laser Irradiation

3.1 Introduction

Reduction of the surface reflectance of optical sensors contributes greatly to the improvement of sensitivity and S/N ratio, the latter by reduced amount of re-incoming light caused by reflection. It is well known that at the interface of materials with different refractive index, light reflects according to the difference [1].

The following merits are expected by suppressing the reflection. (1) Improved light emission efficiency out of the light sources [2], (2) Higher sensitivity of photoelectric sensors by reduced reflection loss. (3) Clearer screen images on display of mobile phones, personal computers, car navigation systems, etc. by reduced reflection of external objects [3, 4].

For photoelectric sensors, the reduction of surface reflection not only increases their sensitivity by the reduced reflection loss, but also greatly improves their S/N ratio by reducing re-incoming light, which is the light from other objects sending out reflection light of the very light reflected at the surface of the sensors.

Regarding infrared sensors used to detect human body etc., thermopiles, thermoelectric sensors, and bolometers are known all of which require infrared optical systems. Silicon is extensively used here as it has high transmittance for the wavelength of around 10 μm and inexpensive. Optical components made of silicon have, however, big disadvantage of high optical loss caused by multiple reflections at their surfaces with refractive index of 3 or greater. As the result, actual amount of light reaching the final component is just a small portion of the incoming light. Incorporating reflection-free structure should contribute a lot to solve this problem.

Generally speaking, reflection-free structures are divided into multi-layer-film method and moth-eye one. Multi-layer-film method works fine when the light angle and wavelength are fixed, but when they are not fixed or the light comes from a low angle, its performance deteriorates considerably, resulting in limited feasible application area.

The moth-eye method, on the other hand, is less affected by wavelength and hence incoming angle, making it a better solution for many applications [2-7]. This moth-eye structure, however, requires fine patterning with the accuracy of tens of nanometers when fabricating periodic structure dimensioned less than wavelength by electron beam projector etc. As each periodic pattern is very small, it takes excessively long time to process one wafer, as long as 300 hours for one 3 inch wafer, for example.

Although being an ideal reflection-free structure, moth-eye had a great difficulty in commercialization due to the lack of established fabrication process, expensive production equipment, and time-taking procedure. It is also possible to use the mold made by electron beam patterning for imprinting. The following issues are encountered here. (1) Materials to be imprinted are usually limited to polymers for use in visible and infrared lights.
(2) Electron beam projector is required in preparing the mold whose initial cost is very high and operation time ratio would be very small. Excessive time needed for making mold further increases its cost. (3) The lifetime of mold is shorter than conventional molds doomed by partial defect and stuck polymer, making it more expensive.

Above mentioned limited usage and high cost hinder its practical use. In order to solve above hurdles, a new method was studied to readily fabricate reflection-free structure towards highly sensitive optical sensors.

This paper focuses in infrared sensors for the wavelength of around 10 μm strongly awaited for detecting human bodies. More precisely, this paper reports the designing of reflection-free structures for 10 μm infrared light, fabrication of it using femtosecond laser, and their evaluation results.

3.2 Design of Anti-reflection structure for Infrared Ray

The concept structure of ARS is indicated in Fig. 3.1. The unit structure has an array structure of the paraboloidal surface and its pitch Λ should be set shorter than half wavelength of incident light in order to function as ARS. Incident light will become an evanescent wave without high-order diffracted lights and the incoming light goes through the surface as zero-dimensional diffracted ray. The refractive index n at a certain space within the ARS layer will be proportional to the mean value of the aperture area of the structure sliced at that height and the cross-sectional surface area of the unit structure, which varies continuously from n_1 to n_2, n_1 and n_2 here correspond to the refractive index of air and that of the structural material respectively. This change of refractive index is constant and slow when the unit structure is a paraboloid, the reflectance ratio becomes minimum in that case. The reflectance in Fig. 3.1 (a) is defined by the following equation, for a ray of light incident on a flat interface with the refractive index of n from air.

$$Ref = (n_2 - n_1)^2 / (n_2 + n_1)^2 \qquad \cdots\cdots\cdots\cdots (1)$$

where Ref, n_1, and n_2 are reflectance, refractive index of air, and refractive index of the material respectively. Putting $n_1 = 1$ and $n_2 = 3.4$ (silicon for $\lambda = 10$ μm) gives the resulting reflection rate of around 30 %.

The loss of incident light is a crucial problem on the surface of sensors with big refractive index differences. Figure 3.1 (b) indicates that the microscopic difference in index of refraction shifts slowly when the pitch of the convexo-concave structure is shorter than half wavelength of the incident light on the interface. When the reflection is controlled on each interface, total

degree of reflection can be efficiently suppressed because of this structure. A related simulation model is shown in Fig. 3.2. Gsolver was used as the commercial design tool and the following parameters were fixed for simulation. The cross-sectional shape of the microstructure was selected to be two dimensional parabola which provides the smallest change of refractive index, and defined the aperture ratio as the ratio of array area to the aperture area. Wavelength was varied from 8 μm to 12 μm. The cross-sectional shape was parabola, which is the structure providing linear change of refractive index in perpendicular direction. The array allocation was set as hexagonal closest packed. Refractive indexes were fixed as n_{air} = 1, $n_{silicon}$ = 3.42, respectively. Incident light was set to enter vertically into the surface with aperture ratio of 75 %.

Figure 3.3 shows the result of a reflectance ratio on condition that the pitch of hexagonal closest-packed structure is 3 μm, 4 μm and 5 μm are set as the heights of the structure. Rigorous Coupled Wave Analysis (RCWA method) is generally used to optimize the height of ARS. This method is a way to decompose incident light as plane wave and analytically define the refractive index. It is commonly used design approach in the region of sub-wavelength where only zero-order diffracted light exists. Wavelength dependence of reflectance can be confirmed from the figure, the reflectance around 10μm is the lowest under the condition of 5 μm height.

In the real fabrication using femtosecond laser, concave structure is easier to fabricate than convex one as the lighted spot is carved. Figure 3.4 shows the calculated results of a reflectance ratio on condition that the aperture ratio of the hexagonal closest-packed structure is 68 %, 79 %, and 91 %, which correspond to the concave width of 2.6 μm, 2.8 μm and 3.0 μm, respectively.

The absolute reflectance is larger and the dependence to the aperture ratio is bigger compared to the convex structure. This result is considered as caused by insufficient smoothness of change with regard to refractive indexes at the

interface of incident light path. On the other hand, the lower reflectance of convex structure can be explained that the interface is located nearer to the substrate, which results in low virtual difference between refractive indexes.

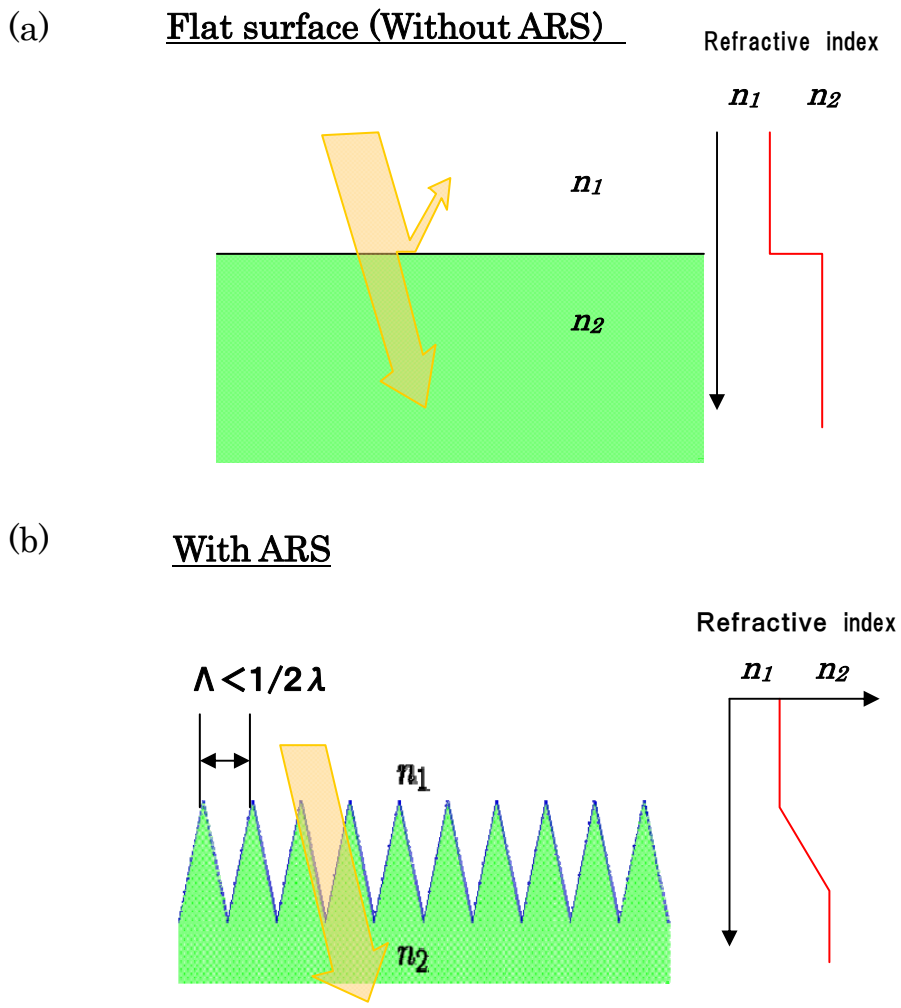

Fig. 3. 1 Schematic diagram of interface of (b) ARS in comparison with (a) conventional flat interface.

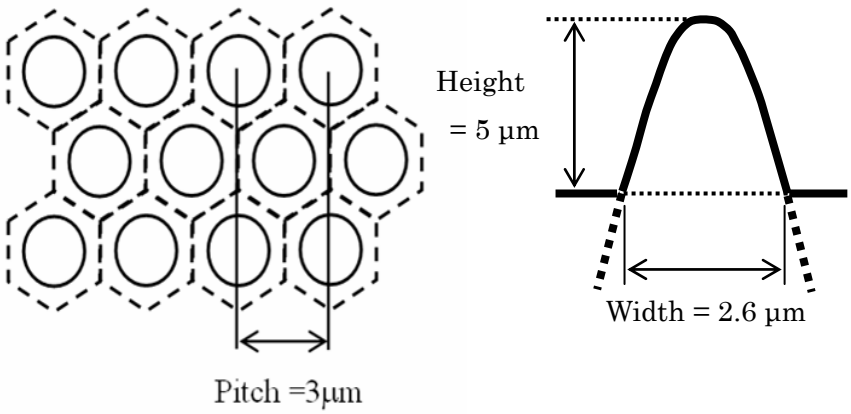

Fig. 3.2 Simulation models of ARS for infrared rays.

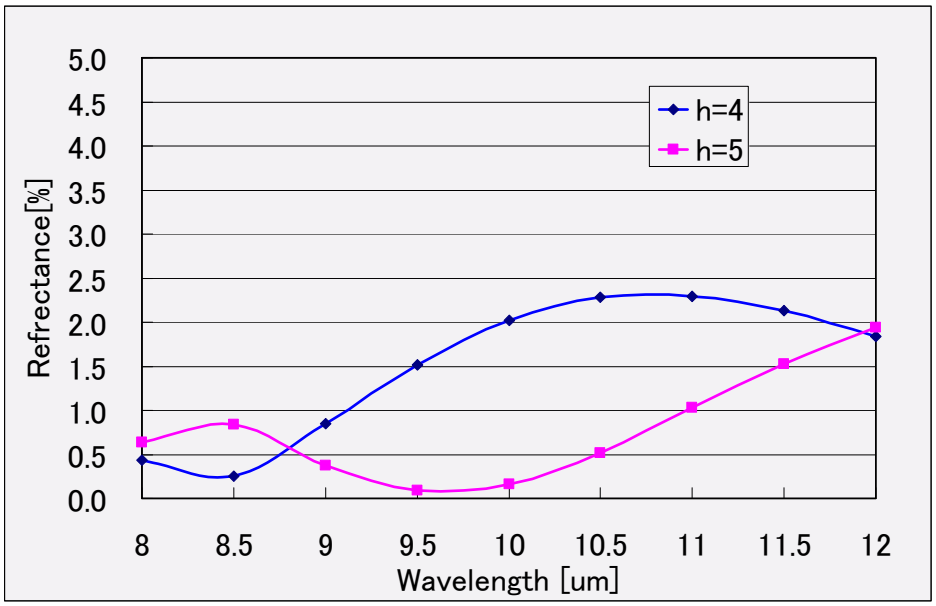

Fig. 3.3 Calculated reflectance of Si ARS vs. height.

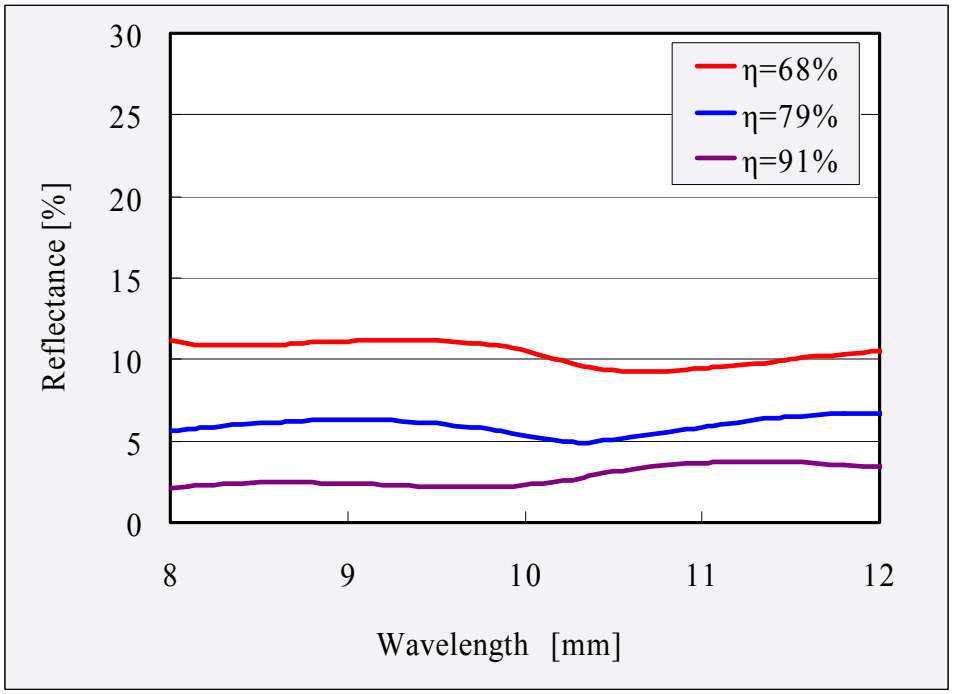

Fig. 3.4 Calculated reflectance of Si ARS vs. aperture ratio.

3.3 Fabrication of Si Infrared Anti-Reflection Structure

3.3.1 Fabrication by Line Scan Laser Irradiation Method

Processing of ARS and its results are discussed in some detail. First, concave structures aligned in hexagonal closest packing were fabricated for processing of silicon ARS by each individual point by point using line scan method of femtosecond laser pulse. The process condition is as follows. The magnification of the objective lens used was 20 and the NA was 0.4. The pulse repetition rate of the laser was 50 kHz, the pulse width was 133 fs, and the laser powers were set to 10 mW, 15 mW and 20 mW, respectively. Scanning speed was 150 mm/s in the processing.

The results obtained are described in Fig. 3.5. Sophisticated hexagonal closest-packed structure cannot be obtained because of low resolution of the stepping motor for line scan method. Concave structures irradiated by weak beam are smaller than expected, and a lot of bare substrate areas still remain. However concave areas increase with the laser power. Small concave structures are formed around margins of concave structures. It is confirmed (by Raman spectroscopy) that the areas are amorphous silicon melted because of high laser power.

(a) [10 mW]

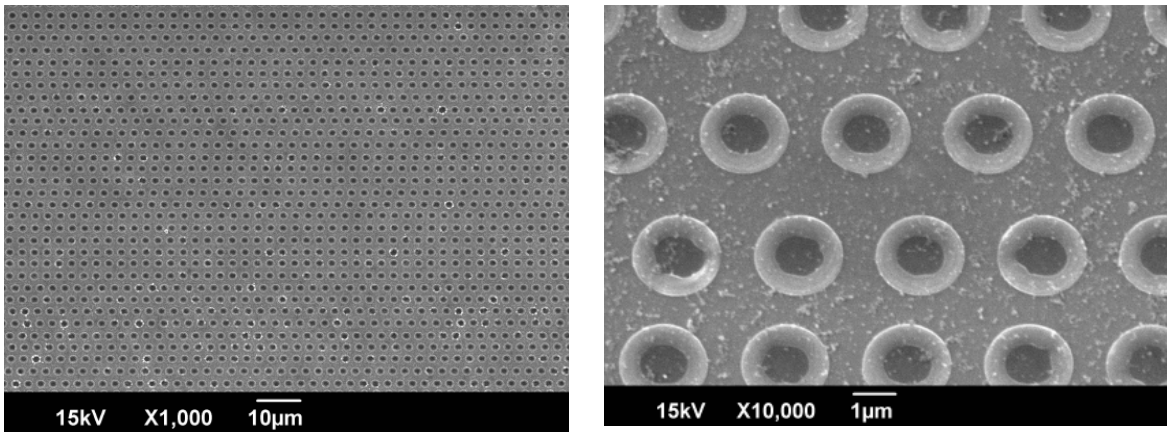

(b) [15 mW]

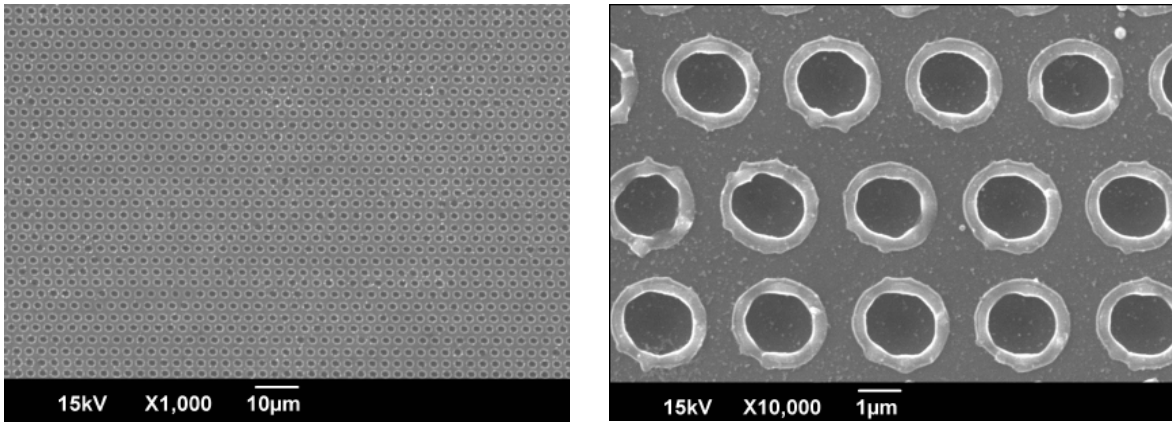

(c) [20 mW]

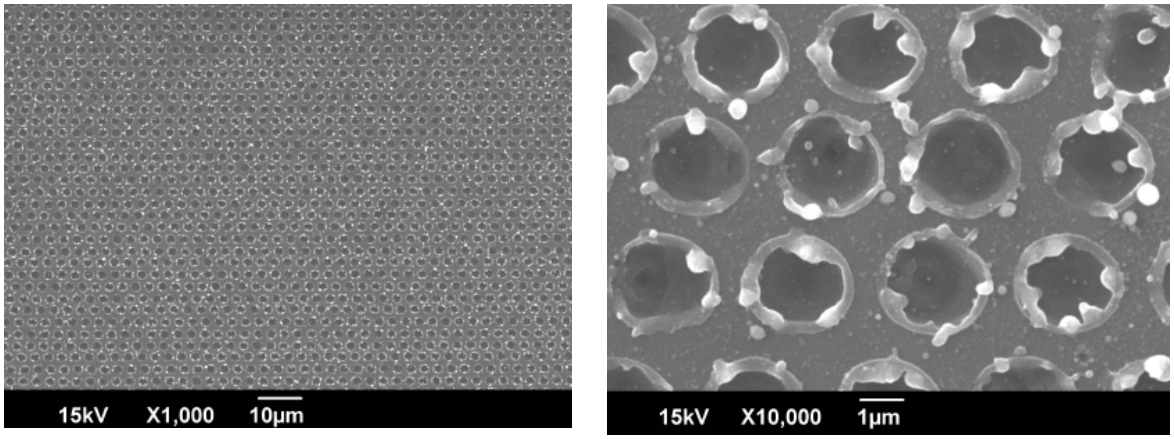

Fig. 3.5 SEM images of fabricated ARS by using femtosecond laser in line scan mode with the irradiated power of (a) 10 mW (b) 15 mW and (c) 20 mW, respectively.

3.3.2 Fabrication by Parallel Irradiation of Femtosecond Laser

The next trial fabrication was carried out using the femtosecond laser in the 3 dimensional parallel patterning mode. The parallel patterning system used is illustrated in Fig. 3.6 [8-10]. The hologram of desired pattern is generated on liquid crystal on silicon (LCOS), and the desired pattern is fabricated by irradiating femtosecond laser light through the LCOS.

The actual ARS is an array of the hexagonal closest packed structures each sized at 3 μm × 2.6 μm as shown in Fig. 3.2. When using the parallel mode, in order to eliminate disturbances by heat or interference, the 7 × 12 pattern of concave structures with the period of 6 μm × 5.2 μm shown in Fig. 3.7 are fabricated in parallel at first, then the substrate is shifted 3 μm in X direction and 2.6 μm in Y direction and complete the final structures as shown in Fig. 3.2. Figure 3.8 shows the hologram used to fabricate ARS of the desired period. The conditions for the parallel process using a femtosecond laser are listed below. The patallel irradiation process condition is described as follows. The magnification of the objective lens was × 20 (NA = 0.4). Pulse repetition rate was 1 kHz, and pulse width was 120 femtoseconds, and laser power was 210 mW (ND: 10 %). Simultaneous irradiation points were at 84 in one shot.

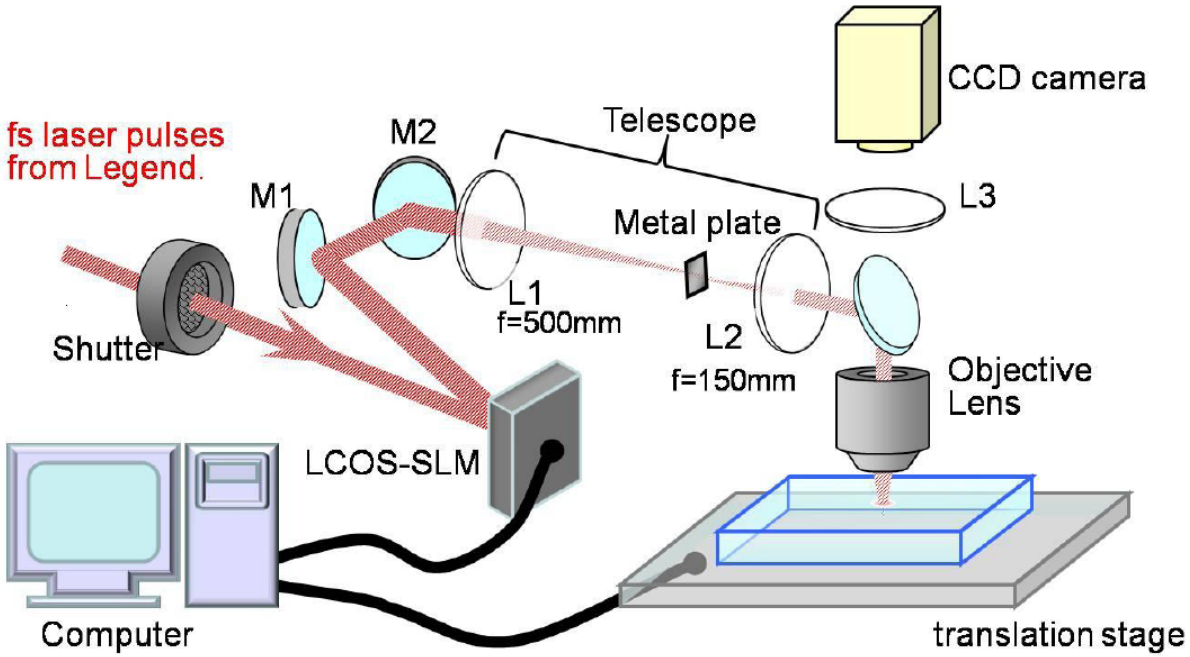

Fig. 3.6 Optical Configuration of parallel drawing fabrication system with femtosecond laser and LCOS-SLM.

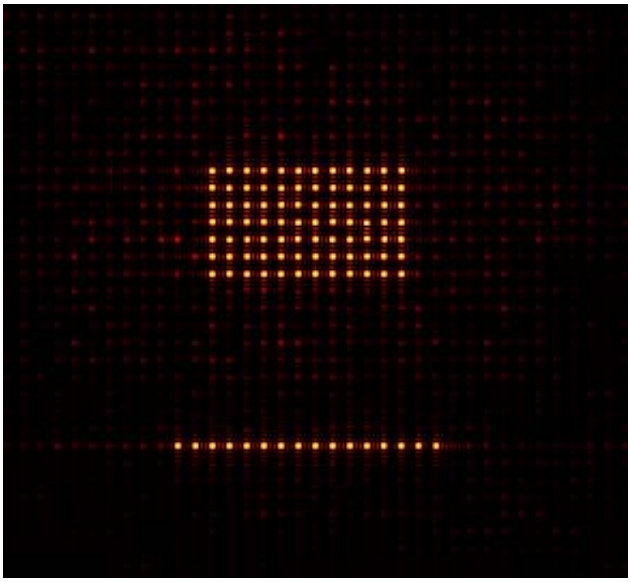

Fig. 3.7 Simulated typical light-intensity distribution used for parallel irradiation of 7 × 12 spots.

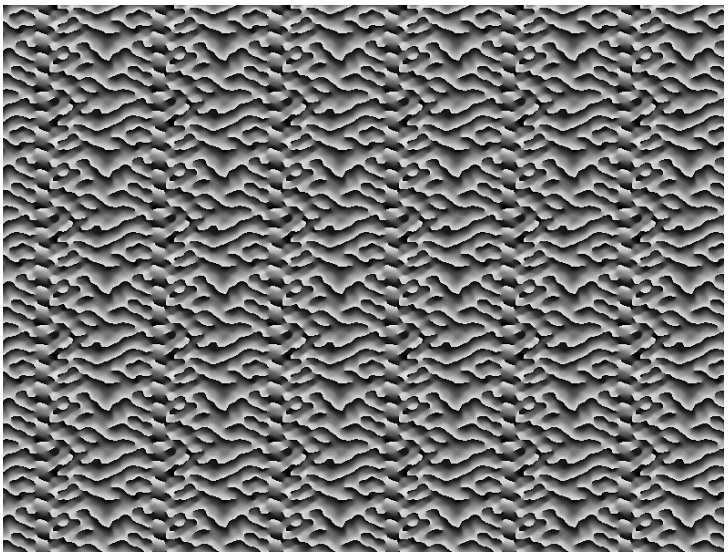

Fig. 3.8 Computer generated hologram for parallel irradiation.

3.4 Evaluation of Anti-Reflection Structure for Infrared Ray

Figure 3.9 shows the SEM image of ARS made by parallel irradiation of femtosecond laser on a Si (100) substrate. Compared to the structures made by linear scanning as described in 3.3.1, the overall surface looks rather rough. In order to locate its cause, the crystal changes at the irradiated spot by the femtosecond laser were examined by evaluating the Raman shift around the spot.

Figure 3.10 shows the Raman shift image on the Si (100) substrate surface and the area irradiated by the femtosecond laser. It is known that irradiating the surface of a Si substrate by a femtosecond laser turns Si into amorphous state. Fitting data shows the expanded hem of Raman shift at the irradiated area by the femtosecond laser, telling the growth of amorphous region. Figure 3.11 shows the Raman shifts mapped at 520 cm^{-1} near the peak of single crystal Si and 480 cm^{-1} where the peak of amorphous Si appears. It is observed clearly that not only the concave area fabricated by a femtosecond laser, but all the area irradiated by the laser are turned into amorphous state. The fact that besides the concave structures, other areas are also turned into amorphous phase shows that the irradiation by the femtosecond laser is not confined to the concave structured area. The reasons are estimated as follows. The beam spacing of the femtosecond laser is only 6 μm making it vulnerable to interference. And simultaneous irradiation of 7 × 12 points with 6 μm pitch heats up the substrate causing thermal interference.

(a)

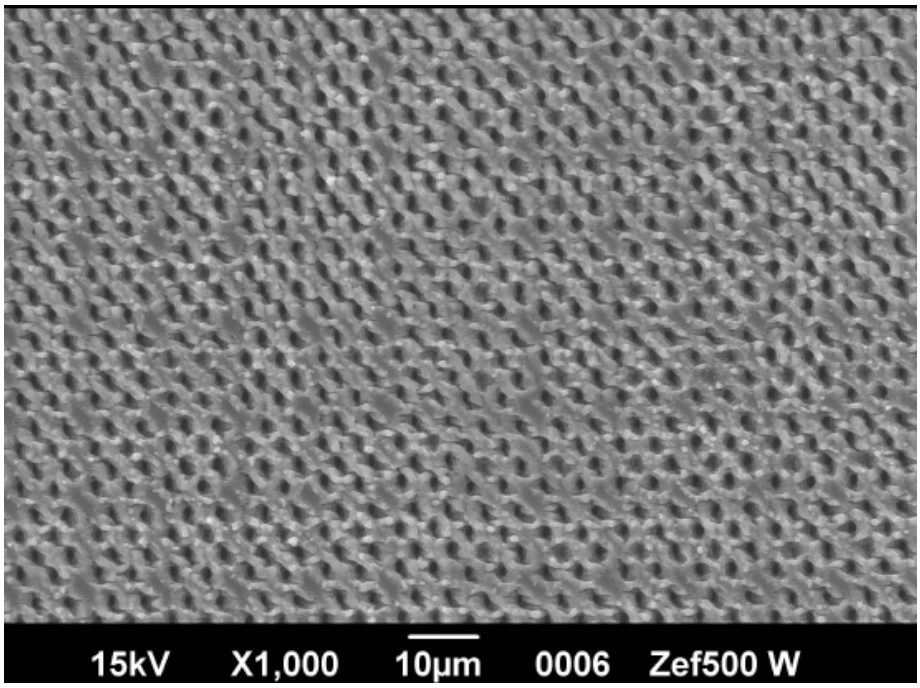

(b)

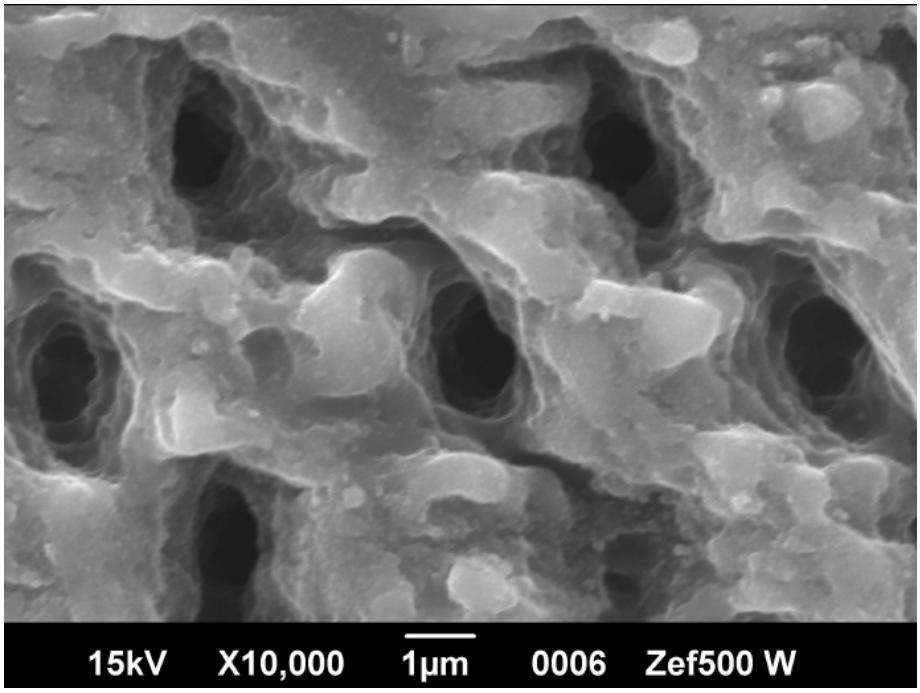

Fig. 3.9 SEM images of fabricated ARS by using parallel irradiation of femtosecond laser (a) × 1000 and (b) × 10000.

(a)

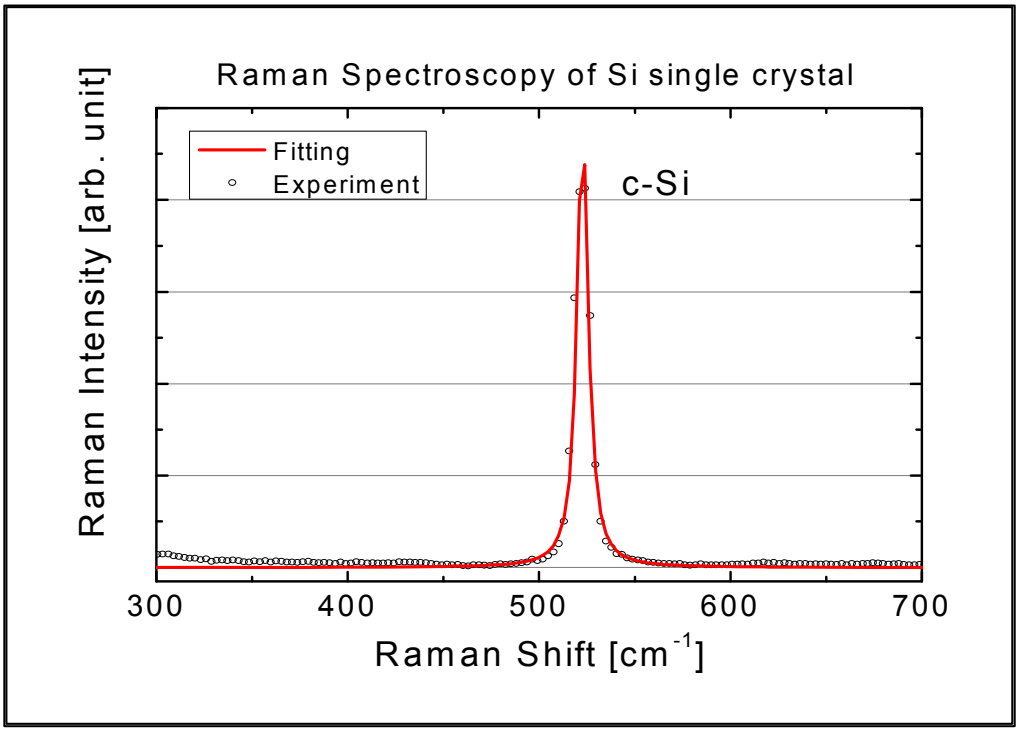

(b)

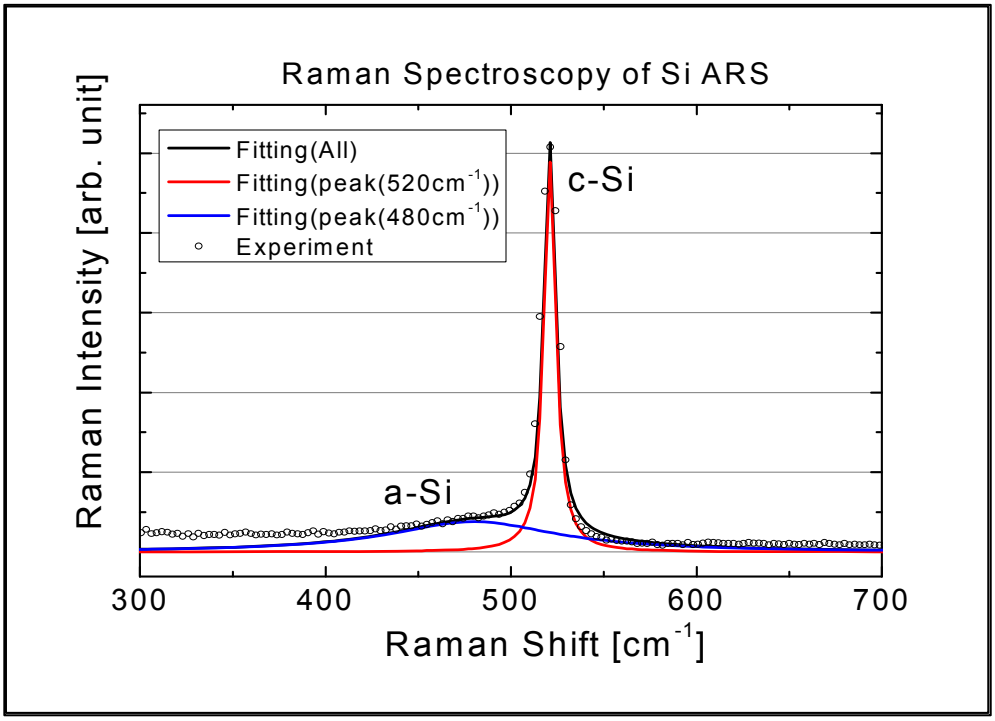

Fig. 3.10 Raman spectroscopy of (a) Silicon single crystal substrate and (b) ARS fabricated by femtosecond laser.

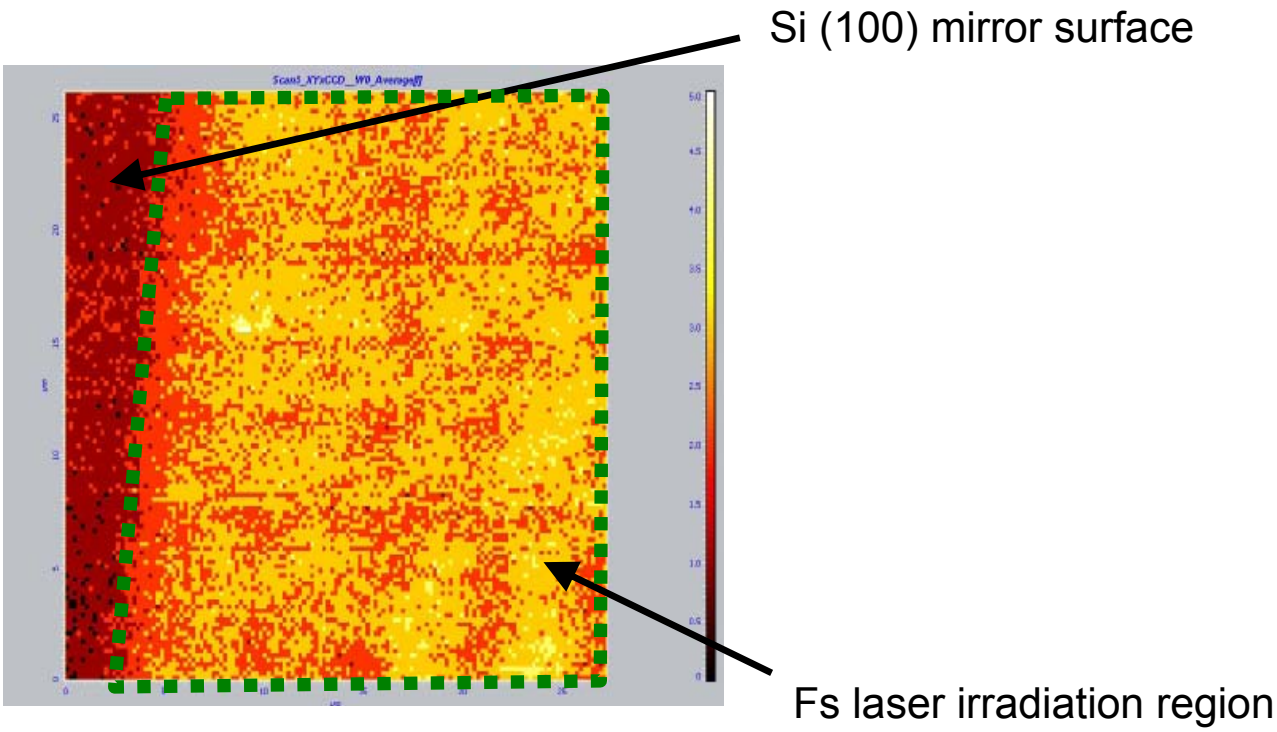

Fig. 3.11 Raman imaging of irradiated and non- irradiated areas.

The transmittance and reflectance of the ARS structure fabricated as above were then evaluated. Microscopic FTIR was used for evaluation. The measured wavelength and area were 6-14 μm and approx. 0.5 mm × 0.5 mm respectively. The fabricated sample size was larger than 2 mm × 2 mm, big enough compared to the measured area.

Figure 3.12 shows the measured transmittance of ARS made by line scanning. Although clear microstructures were fabricated, the transmittance was not much different from Si substrate. Only a small increase of transmittance from Si substrate was observed, and the causes are estimated to be the insufficient shapes and dimensions of the holes.

The next Fig. 3.13 shows the result obtained by parallel irradiation of femtosecond laser. For shorter wavelength than 10 μm, the transmittance of ARS was poorer than Si substrate, and for longer wavelength opposite result was observed.

Thus, ARS is found effective for the wavelength above 10 μm. In order to identify the reason why the transmittance was poor for shorter wavelength, measurements were made with microscopic FTIR in its reflection mode. Figure 3.14 shows the obtained result. The reflection ratio around 10 μm was about 10 % which tells the effect of ARS as positive. Considering the result of transmittance, or from the sum of transmitted and reflected lights, increased loss is estimated for shorter wavelength.

It is inferred that the parallel irradiation of femtosecond laser has damaged the substrate surface outside of the desired concave spots, and scattered the light. The fact that the ARS hence made shows clear effect for longer wavelength, additional decrease of reflection can be expected by next candidate's techniques. One is fabrication of the microstructure with less pitch, the other is obtaining smooth ARS surface by low damaging chemical and/or dry etching [11-12] after femtosecond laser irradiation for approaching ideal concave smooth surface.

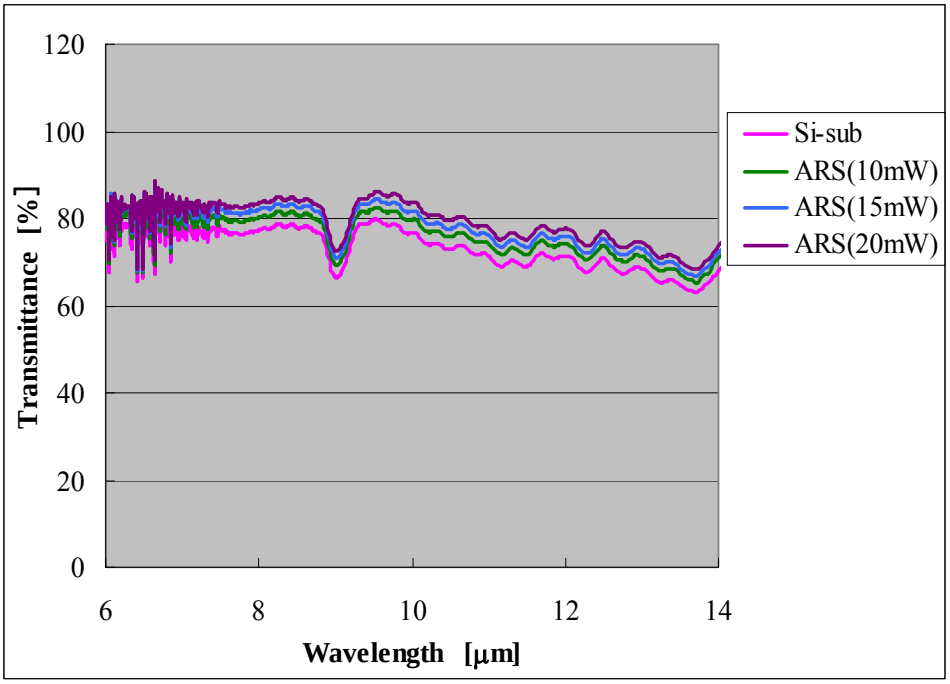

Fig. 3.12 FTIR transmittance spectrum of Si ARS fabricated by line scan femtosecond laser irradiation.

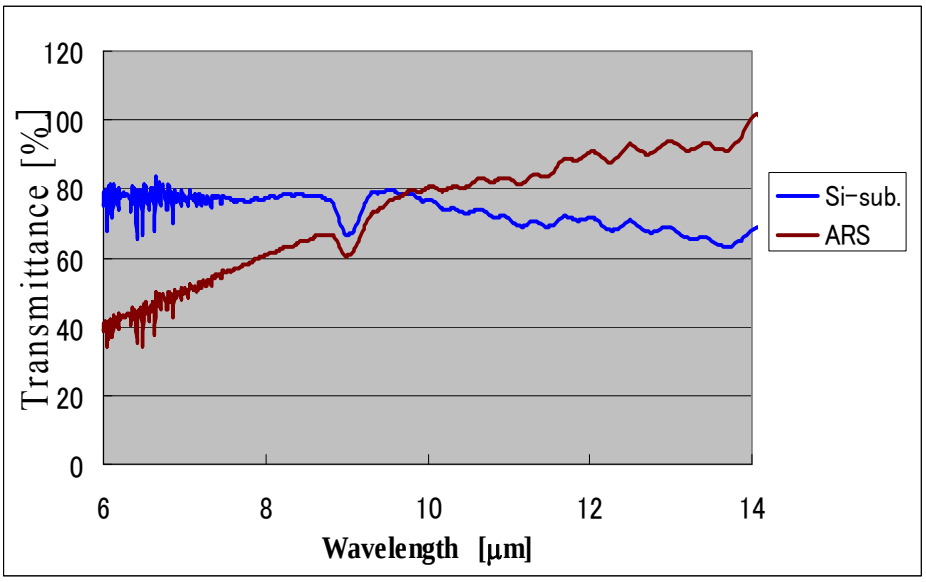

Fig. 3.13 FTIR transmittance spectrum of Si ARS fabricated by femtosecond laser parallel irradiation.

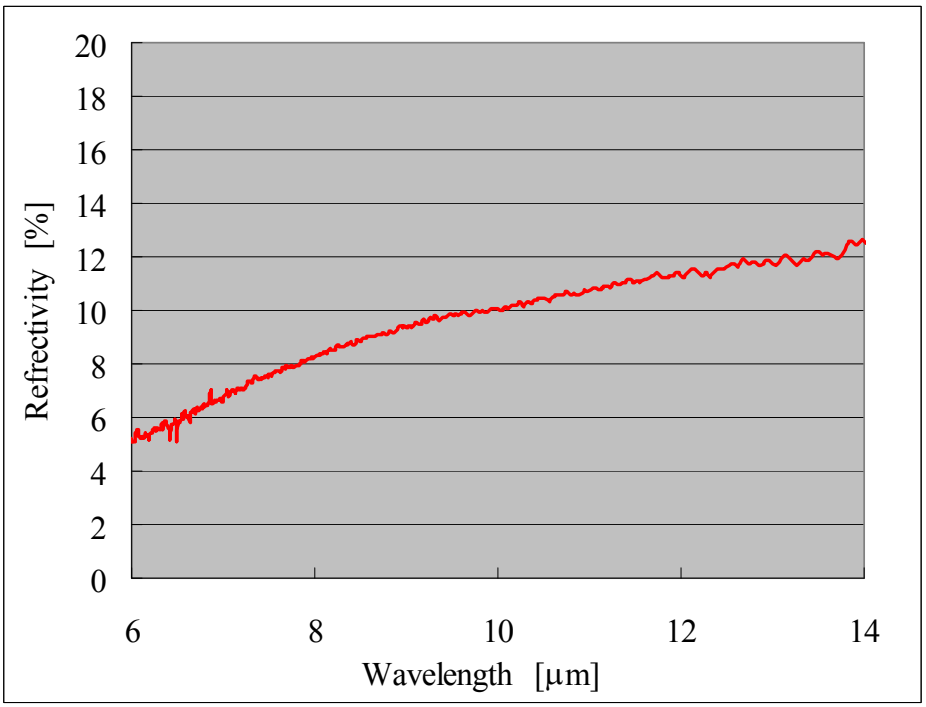

Fig. 3.14 FTIR reflectivity spectrum of Si ARS fabricated by parallel irradiation of femtosecond laser.

3.5 Conclusion

In order to improve sensitivity and S/N ratio of infrared sensors for the wavelength of around 10 μm, fabrication method of ARF was studied using a femtosecond laser.

With the line scanning method, which irradiates laser one by one to every spot, the substrate area remained wider compared to the concave spots and little significant effect to suppress reflection was obtained.

In case of the parallel irradiation method of femtosecond laser, on the other hand, the microstructures were fabricated all over the area, and good ARS were realized for the wavelength of 10 μm or above. Further trial to decrease light scattering, as listed below, are needed to achieve ARS effective for wider wavelength range. (1) With the optimized parallel irradiation conditions for femtosecond laser, the disturbance of surface structure incurred by parallel irradiation is presumably caused by interference and heating. The 6 μm period was used in this paper, whereas less disturbance was expected by using wider pitch such as 9 μm or 12 μm. This time the pitch was selected to meet the designed shape, in reality though the transmittance become lower at shorter wavelength. Another effort therefore could be using smaller period to improve transmittance for shorter wavelength. (2) Meanwhile with the optimum parallel irradiation conditions of femtosecond laser, line scanning could fabricate smaller concave structure than intended, resulting in less effective ARS. Improving ARS can be expected by fabricating bigger concave structure and employing smaller period.

References

[1] C.G.Bernhard, Endeavour **26**, 79 (1967).

[2] Y.Kanamori, K.Hane, H.Sai and H.Yugami, App. Phys. Lett. **78**, 142 (2001).

[3] R.Fujioka, O.Nishizaki, Y.Ito and Y.Okuno, Proceedings of NNT'07 **52** (2007).

[4] K.Sanari, T.inobe, Y.Takagi, Y.Yamamoto, and Y.Ito, Proceedings of IDW2009, FMC8-2, 2009.

[5] M.E.Motamedi, W.H.Southwell and W.J.Gunning, Appl. Opt. **31**, 371 (1992).

[6] P.Lalane and G.Michael Morris, Nanotechnology **8**, 53 (1997).

[7] Y.Kanamori. M.Sasak and K.Hane, Opt. Lett. **24** 1422 (1999).

[8] Y.Kuroiwa, N.Takeshima, Y.Narita, S.Tanaka and K.Hirao, Opt. Express **12**, 1908 (2004).

[9] Y.Hayasaki, T.SugimotoA.Takita and N.Nishida, Appl. Phys. Lett. **87**, 031101 (2005).

[10] M. Sakakura, T.Sawano, Y.Shimotsuma, K.Miura and K.Hirao, Jpn. J. Appl. Phys. **48**, 126507 (2009).

[11] S.Samukawa, K.Sakamoto and K.Ichiki, Jpn. J. Appl. Phys. **40** 779 (2001)

[12] S.Samkawa, K.Sakamoto and K.Ichiki, Jpn. J. Appl. Phys. **40**.997 (2001)

Summary

In the present study, great efforts were poured in order to improve the optical sensing characteristics, e.g. high sensitivity, low power consumption, low signal-noise ratio, long detection range, and long operating lifetime. By using atomic level layer control to grow and fabricate nano-structure in nanosized accuracy, a number of unique high efficiency optical sensing devices were created.

In Chapter 1, the author investigated improvement of light emitting device characteristics based on III-V compound semiconductors. AlGaAs/GaAs short period superlattices have been applied to various part of AlGaAs quantum well laser diode. By using short period superlattice around buffer layer and active layer, significant improvements of the laser characteristics including high efficiency, low threshold current, and high light output power with high temperature stability were confirmed.

On the other hand, redeeming the demerit of laser diode such as eye safety, life time and so on, a new pin-point LED was proposed and successfully put into commercial production.

Further investigated is the usage of the other crystal axis instead of (100). It was confirmed that (111) oriented substrate has new possibility to improve the light output characteristics. It was also confirmed that the Migration Enhanced Epitaxy method must be the most suitable technique to grow AlGaAs on (111)B oriented substrate.

In Chapter 2, the growth mechanism of ZnO nanostructure was investigated. The well aligned ZnO nanodot arrays have been formed along the step edges of R-plane sapphire extending more than several ten micrometers. This implies that sapphire can be a good template for manufacturing the semiconductor nanostructures on it, and as the result II-IV semiconductor nanostructures can be manipulated on an insulator even at near atmospheric pressure by a conventional MOCVD.

A bridge firmly connecting two electrodes was successfully fabricated and the growth of ZnO formed between the electrodes was directly conducted on the electrodes in the aqueous solution. The value of electric resistance of the structure was several mega-ohms in a room, while when it is irradiated by the UV light of 390 nm wavelength with applied voltage of 5 V, high photoconductivity with more than 20 μA was confirmed. The response characteristics for other external stimuli have also been confirmed.

Moreover, the author proposed a simple but convenient method to fabricate ZnO selectively and artificially between two micron-gap electrodes using the electrolytic deposition in aqueous solution of $Zn(NO_3)_2$ or $Zn(CH_3COO)_2$. The electrodes used for electrolytic deposition can be rapidly diverted to the contact electrodes for a sensing device. The device shows the capability to detect 500 ppm H_2 gas without external heating.

In Chapter 1 and Chapter 2, the author investigated high efficiency and high sensitivity optical devices by using bottom up nanotechnology. In Chapter 3, at the focal point of decreasing reflection at Si-air interfaces, the moth–eye structure fabricated by femtosecond laser for infrared optical sensing was reported. Drawing a comparison between parallel drawing method and line scan mode, the advantages of parallel drawing method were confirmed as follows; (1) Anti-reflection characteristics were superior to line scan mode in these examinations. (2) High throughput of fabricating anti-reflection structure was confirmed. In this case, parallel drawing method is about 100 times higher than line scan mode. It should be quite important for practical use.

List of Publications

Chapter 1

H.Imamoto, F.Sato, K.Imanaka and M.Shimura
"GaAs double quantum well laser diode with short period $(AlGaAs)_m(GaAs)_n$ superlattice barriers"
Applied Physics Letters **54**, 1388 (1989).

H.Imamoto, F.Sato, K.Imanaka and M.Shimura
"Migration-enhanced epitaxy on a (111)B oriented GaAs substrate"
Applied Physics Letters **55**, 115 (1989).

K.Imanaka, F.Sato, H.Imamoto and M.Shimura
"High-efficiency AlGaAs/GaAs single quantum well semiconductor laser with strained superlattice buffer layer"
IEEE Photonics Technology Letters **1**, 8 (1989).

H.Imamoto, F.Sato, K.Imanaka and M.Shimura
"Visible multi-quantum-well laser diode composed of $(AlGaAs)_m(GaAs)_n$ short period superlattice"
Electronics Letters **25**, 121 (1989).

F.Sato, H.Imamoto, M.Asai, K.Imanaka and M.Shimura
"Low thermal expansion polyimide buried ridge waveguide AlGaAs/GaAs single-quantum-well laser diode"
Journal of Applied Physics **63**, 964 (1988).

H.Imamoto, F.Sato, K.Imanaka and M.Shimura
"AlGaAs/GaAs superlattice multi-quantum-well laser diode"
Superlattice and Microstructure **5**, 167 (1989).

K.Imanaka, H.Imamoto, F.Sato, M.Asai and M.Shimura
"Inner-stripe AlGaAs/GaAs laser diode by single-step molecular beam epitaxy"
Electronics Letters **23**, 209 (1987).

H.Imamoto, F.Sato, K.Imanaka and M.Shimura
"Low temperature growth of AlGaAs/GaAs single quantum well laser diode by migration enhanced epitaxy"
Proceedings of the first international conference on electronic materials **1**,125 (1988).

H.Imamoto, F.Sato, K.Imanaka and M.Shimura
"Migration enhanced epitaxy of GaAs on exactly (111) oriented Si substrate"
Extended Abstracts of 32nd Electronic Materials Conference (EMC1990) 79 (1990).

T.Takagi, **H.Imamoto**, F.Sato, K.Imanaka and M.Shimura
"High-power broad mesa structure AlGaAs/GaAs single-quantum-well edge emitting LED"
IEEE Photonics Technology Letters **1**, 14 (1989).

M.Asai, F.Sato, **H.Imamoto**, K.Imanaka and M.Shimura
"Low-temperature (350°C) growth of AlGaAs/GaAs laser diode by migration enhanced epitaxy"
Journal of Applied Physics **64**, 432 (1988).

F.Sato, **H.Imamoto**, K.Imanaka, and M.Shimura
"Low thermal expansion polyimide buried ridge-waveguide AlGaAs laser diode"
Proceeding of SPIE Advanced Processing of semiconductor Devices II, **945**, 18 (1988).

F.Sato, **H.Imamoto**, M.Asai, K.Imanaka and M.Shimura
"High-quality AlGaAs/GaAs quantum well with a short period (InGaAs)(GaAs) strained superlattice buffer layer"
Journal of Crystal Growth **95**, 206 (1989).

H.Imamoto, F.Sato and M.Shimura
"GaAs Migration Enhanced Epitaxy and Device Applications"
Technical Report of IEICE **ED89-103,** 33 (1989).

H.Imamoto, M.Yanagase and M.Takaoka
”Reliability Estimation of AlGaInP-based Pin-point LED ”,
Technical Report of IEICE **R96-21**,11 (1996).

T.Nakagawa, **H.Imamoto**, N.J.Kawai, T.Kojima and K.Ohta
”Observation of resonant tunneling via first excited level in double barrier diodes”
Electronics Letters **22**, 406(1986).

T.Nakagawa, **H.Imamoto**, T.Kojima and K.Ohta
”Observation of resonant tunneling in AlGaAs/GaAs triple barrier diodes” ,
Applied Physics Letters **49**, 73 (1986).

T.Nakagawa, **H.Imamoto**, T.Sakamoto, T.Kojima, K.Ohta and N.J.Kawai
”Observation of negative differential resistance in CHIRP super-lattice”
Electronics Letters **21**, 882 (1985).

K.Imanaka, F.Sato, **H.Imamoto** and M.Shimura
”High efficiency AlGaAs/GaAs single- quantum-well laser with a short period (InGaAs)(GaAs) strained superlattice buffer layer”,
Conference Digests of 11th IEEE international semiconductor laser conference, 129 (1988).

T.Takagi, **H.Imamoto**, F.Sato, K.Imanaka and M.Shimura,
“Broad Area Phase-Locked Superlattice Barrier Quantum Well Laser Diode”,
IEEE, Photonics Technology Letters **1**, 4 (1989)

Chapter 2

K.Kametani, H.Dumot, **H.Imamoto** and S.Fujita
”Direct Growth of ZnO Whiskers bridging between Micron-gap Electrodes in Aqueous Solution”
Journal of the Society of Materials Science **563,** 278 (2007).

R. Hattori, **H.Imamoto**, K.Kametani and S. Fujita
”Growth in Aqueous Solution and Characterization of ZnO Whiskers Bridging Between Micron-gap Electrodes”
Proceedings of Material Research Society (MRS) Meeting **L08-30**, 1035 (2007).

K.Kametani, **H.Imamoto** and S.Fujita
”Formation of ZnO nano-dot arrays along the step edges on R-face sapphire by metal-organic chemical vapor deposition”
Physica E: Low-dimensional Systems and Nanostructures **32**, 33 (2006).

K. Kametani, **H.Imamoto** and S. Fujita
"Zinc oxide nanostructures grown by metal-organic chemical vapor deposition on various planes of sapphire"
Proceeding of 12th international conference on Modulated Semiconductor Structures **237** (2005).

Chapter 3

H.Imamoto, M.oba, Y.Ito, M.Kumatoriya, M.Sakakura, Y.Shimotsuma, K.Miura and K.Hirao
"Fabrication and Characterization of Silicon Anti-Reflection Structures by femtosecond Laser for Infrared Rays"
Proceedings of the 2010 international Symposium on Organic and Inorganic Materials and Related Nanotechnologies, 216 (2010).

H.Imamoto, S.Kanehira, Xi.Wang, K.Kametani, M.Sakakura, Y.Shimotsuma, K.Miura and K.Hirao
"Fablication and Characterization of Silicon Anti-Reflection Structures for Infrared Rays using a Femto-second Laser"
Optics Letters (in press)

S.Ueki, Y.Nishimori, H.Imamoto, T.Kubota, M.Sugiyama, S.Samukawa and G.Hashiguchi
'The analysis of a comb-drive actuator with the consideration of depletion layer'
IEEJ Transactions and Micromachines, 130-E Number 8, 388(2010).

S.Ueki, Y.Nishimori, H.Imamoto, T.Kubota, M.Sugiyama, H.Kawakatsu, S.Samukawa and G.Hashiguchi
"Method to evaluate the influence of etching damage on micro-cantilever surface on its mechanical properties"
Japanese Journal of Applied Physics 50, 026503 (2011)

S.Ueki, Y.Nishimori, H.Imamoto, T.Kubota, M.Sugiyama, S.Samukawa and G.Hashiguchi
'The analysis of a comb-drive actuator with the consideration of depletion layer'
Proceedings of 26th Sensor Symposium on Sensors, Micromachines and Applied Systems 127 (2009).

Acknowledgements

First of all, the author would like to express deep appreciation to Professor Kazuyuki Hirao, Department of Material Chemistry, Graduate School of Engineering in Kyoto University, for his insightful guidance and supervision throughout this study.

The author is especially grateful to Professor Kiyotaka Miura for his technical and general advice. And the author also thanks Professor Katsuhisa Tanaka for his instructive suggestions.

The author would also like to express deep appreciation to Prof. Shizuo Fujita for his valuable suggestions and helpful discussions about crystal growth of compound semiconductor and the characteristics of the devices.

Grateful acknowledgements are made to Associate Professor Yasuhiro Shimotsuma and Dr. Masaaki Sakakura for their helpful discussion and kind help in the usage of femtosecond laser.

Special thanks to Dr. Keisuke Kametani for his valuable discussions and his kind encouragement.

The author would like to extend thanks to Dr. Koichi Imanaka, Managing Officer and Senior General Manager of Research & Development HQ, OMRON Corporation and Dr. Masatoshi Oba, General Manager of the Core Technology Center, Research & Development HQ, OMRON Corporation for providing the opportunity to carry out this study and continuing encouragement.

Part of this study was subsidiaries as “Kyoto Nanotechnology Cluster” and “Kyoto Environmental Nanotechnology Cluster” by Knowledge Cluster Initiative of the MEXT. The author would like to express deep thanks to those concerned in this organization.

Finally, the author would like to express his appreciation to his wife, Ikuko Imamoto, for hearty encouragement.